FLUORESCENCE AND PHOTOBLEACHING IN PHOTODYNAMIC THERAPY

PHOTODYNAMIC THERAPY DOSIMETRY THROUGH MEASUREMENT OF FLUORESCENCE DECREASE DUE TO PHOTOBLEACHING

By

ROBERT PAUL HAWKES, B.Sc.

A Thesis
Submitted to the School of Graduate Studies
in Partial Fulfilment of the Requirements
for the Degree
Master of Science

McMaster University

MASTER OF SCIENCE (1997) McMaster University
(Medical Physics)

TITLE: Photodynamic Therapy Dosimetry Through Measurement
of Fluorescence Decrease due to Photobleaching

AUTHOR: Robert Paul Hawkes, B.Sc. (McMaster University)

SUPERVISOR: Dr. T. J. Farrell

NUMBER OF PAGES: xvi, 124

ABSTRACT

The phenomenon of photobleaching of a photosensitizer during photodynamic therapy (PDT) is well known. For second generation photosensitizers it may be possible to exploit this effect to enhance the volume of damaged tissue and improve the efficacy of PDT. In addition, as a consequence of photobleaching, the fluorescence emitted by the photosensitizer will decrease during PDT. Mathematical models were developed which describe fluorescence emission, photobleaching and tissue necrosis resulting from the irradiation of tissue containing photosensitizer using an appropriate light source. Diffusion theory was used to model bleaching in a semi-infinite medium caused by broad-beam irradiation, and both pencil and broad-beam fluorescence excitation of the photosensitizer. In addition, models were developed for an isotropic point source imbedded in an infinite medium. Based on the relationship between the decreasing fluorescence signal and the increasing volume of tissue damage, these models allow the extent of necrosis achieved during treatment to be monitored. By analysing spatially resolved fluorescence measurements predictions about necrosis depth that are insensitive to treatment parameters such as photosensitizer concentration, tissue optical properties and bleach rate are possible.

Tissue simulating optical phantoms that allow for relatively simple and accurate alteration to optical properties were developed. Photosensitizers which still undergo fluorescence and photobleaching in the solid medium were also added. Using these phantoms, treatment was simulated and spatially resolved fluorescence was measured as a function of time for a wide range of initial treatment parameters. Photobleaching of the photosensitizers was observed to occur through a decrease in fluorescence emission. Also, spatially resolved measurements provided information about the average photosensitizer depth, which was seen to increase with time, with little knowledge of initial treatment parameters. These experimental results were then compared with predictions from the mathematical theory, illustrating the validity of the models. The value and feasibility of this technique for photodynamic therapy dosimetry are discussed, along with planned improvements.

ACKNOWLEDGEMENTS

I wish to convey my appreciation to Dr. Tom Farrell for his patience and guidance throughout the course of this thesis. The insights he provided were invaluable, and his calm, light-hearted approach helped me through the difficult times.

I would also like to express my gratitude to Dr. Mike Patterson for his additional direction and conceptual development, without which none of this would have been possible.

I also wish to thank Dr. Robert Weersink, Jody Bruulsema and Dr. Joe Hayward for their help and advice with the experimental aspects of the research.

Thanks also goes to John Blenkey and Alan Hazelhurst for their prompt, high quality work in the machine shop.

Special thanks are given to Kevin Diamond for his thought provoking discussions and always dependable curve-fitting routines.

Finally, I would like to thank Rob Hunter for always being available to take well-deserved coffee breaks, and my parents for their continuing support.

TABLE OF CONTENTS

TABLE OF CONTENTS (continued)

TABLE OF CONTENTS (continued)

LIST OF FIGURES

LIST OF FIGURES (continued)

LIST OF FIGURES (continued)

LIST OF FIGURES (continued)

LIST OF FIGURES (continued)

LIST OF FIGURES (continued)

LIST OF FIGURES (continued)

LIST OF TABLES

1 INTRODUCTION

1.1 Origins of Photodynamic Therapy

Although photodynamic therapy has only recently gained significant attention, awareness of this photochemical phenomenon has existed since the turn of the century. Raab first discovered the photosensitizing effect in 1900 when he established that paramecia exposed to acridine dye and sunlight were killed while those subjected to either dye or sunlight independently survived (Pass 1993). In 1903, this phenomenon was first used to treat skin cancer when oncologists combined the drug eosin with light (McCaughan 1992). It was not until 1904 that Tappeiner coined the phrase "photodynamic" to differentiate between the reaction Raab had discovered, which specifically requires oxygen, and similar photochemical or photosensitizing reactions which do not require oxygen, such as the treatment of psoriasis using ultraviolet light and psoralens (McCaughan 1992). Porphyrin-based photosensitizing drugs were first introduced by Hausman in 1911 (Pass 1993) and although other types of photochemicals have been developed (e.g. phthalocyanines, chlorins), these remain as the most widely used. In the 1940s it was shown by Figge *et al* (1948) that hematoporphyrin, when injected into the bloodstream, would be selectively retained by malignant tissues over normal healthy tissues. Not only did Figge realize the therapeutic implications of this photosensitizer localization, he also felt tumour detection could be possible based on the knowledge that excited porphyrins would produce detectable fluorescent light (Figge *et al*

1948). These revelations led to the work of Lipson in the 1960s who attempted the first human treatment by injecting synthesized hematoporphyrin derivative (HpD) and irradiating the tumour with light resulting in the predicted cytotoxic effect (Lipson *et al* 1966). Also, by endoscopically detecting fluorescence emitted by excited HpD, Lipson located tumours in which drug had localized (Lipson *et al* 1966 and Gregorie *et al* 1968). It was not until the 1970s when Dougherty, considered the father of modern PDT, began his studies that moderate success was achieved treating animal and human malignancies (Dougherty *et al* 1978 and Dougherty 1987). It is his pioneering work that has led to both the high level of interest in photodynamic therapy (PDT) as a cancer treatment modality, as well as the discovery of current limitations.

Recently, a great deal of research has been undertaken to find photosensitizers that have a greater tumour to healthy tissue uptake ratio, are excited by light of longer, more penetrating wavelengths, have a higher yield of cytotoxic species and cause less skin photosensitivity. Techniques for predicting photodynamic damage are sub-optimal leading to many ineffective treatments. This stems mainly from the fact that straightforward dosimetric indicators do not exist and models of the process are very complicated. Also, the reaction processes and mechanisms of damage are poorly understood. Current research is also aimed at improving light delivery techniques with the use of lasers and fibre optics. Despite these limitations, PDT was approved for clinical use in Canada in 1993 and received FDA approval in the United States in 1995. Presently, a wide range of malignancies are treated including bladder, endobronchial, esophageal and skin cancers (McCaughan 1992).

1.2 Overview of the Photodynamic Therapy Mechanisms

The goal of any cancer therapy technique is to completely destroy the tumour while doing as little damage as possible to nearby healthy tissue. Traditionally, malignant tumours have been treated with radiation or chemical therapy, often in conjunction with surgery. Radiation therapy generally involves the directing of high energy gamma rays or electrons at the tumour such that the majority of energy deposition is within the cancerous cells. Unfortunately, for any sub-cutaneous cancer the radiation travels through healthy tissue both before and after it reaches the tumour inflicting significant damage.

With chemotherapy, anti-cancer drugs administered into the bloodstream have a greater toxic effect on cancerous cell populations than on normal cells. Most selectivity is based on differences between kinetics of normal and neoplastic cells. The fact that tumour cells are actively dividing and growing makes it possible to target them during a specific phase of the cell cycle. Other cancer drugs kill cells by taking advantage of unique biochemical differences. In all cases, normal healthy tissues are also affected by the anti-cancer agents, resulting in damage throughout the body. This is responsible for the many side effects associated with chemotherapy treatment.

Photodynamic therapy minimizes damage to healthy tissue through a unique inherent dual selectivity. When a photosensitizing drug is administered, most normal healthy cells retain very little of the drug whereas tumour cells preferentially retain the photosensitizer molecules. The reasons for this have not yet been established but it is postulated that the lack of lymphatics in tumours prevents them from removing aggregated drug (McCaughan 1992). At some time following administration, the majority of photosensitizer will have cleared the healthy tissues leaving an advantageous tumour to healthy tissue ratio, providing the first mechanism of tumour selectivity. Typically, a tumour-to-tissue ratio between two to one and five to one is achieved (Pass 1993).

Whereas chemotherapy drugs produce unregulated toxic effects, a photosensitizer requires the absorption of light of a particular wavelength to initiate the tissue damaging reactions. Since there is a lower concentration of drug in healthy tissue than in the tumour, there is a much lower yield of cytotoxic products in the healthy tissue. This provides a second opportunity for selectivity, since the light can be directed at the tumour, much like radiation therapy, sparing healthy tissue that is not in the path of the excitation light. The threshold hypothesis (Potter 1986 and Moan 1986) has been postulated which states that a minimum amount of toxic species must be produced in a small volume of tissue in order for necrosis to occur. Based on the dual selectivity, it should be possible to spare most of the normal tissue by keeping it below the threshold, while destroying the tumour which should exceed the threshold. This effect is obviously enhanced if the tumour to healthy tissue uptake ratio is increased, and is also aided by the process of photobleaching which will be discussed.

1.3 Molecular Basis for PDT

When light excites a photosensitizer in the electron singlet ground state, several reactions can take place resulting in toxic photoproducts (free radicals for type I photosensitizers, singlet oxygen for type II), emission of fluorescent light, or degradation of the photosensitizer itself, referred to as photobleaching.

If the additional energy of the excited atom causes a reversal in the spin of an electron, the photosensitizer is said to be in the excited triplet state. With type II photosensitizers such as Photofrin II, excess energy from this excited state can then be transferred to a ground state triplet oxygen molecule resulting in singlet oxygen. It is this excited singlet oxygen that is thought to do the majority of biological damage in PDT through oxidative cell plasma membrane injury (Thorpe *et al* 1995).

Alternatively, the excited singlet photosensitizer molecule can emit a photon to return to the ground state. These fluorescence photons are at wavelengths characteristic of the excitation wavelength and electronic transition.

Originally, it was thought that the chemical integrity of photosensitizers was unaffected by irradiation, always returning to the ground state for indefinite activation. Recently, however, the phenomenon of photobleaching became apparent (Mang *et al* 1987 and Moan 1986). Photochemical reactions can alter the photosensitizer molecule so that it no longer absorbs light at the excitation wavelength (Patterson and Wilson 1994). Also, the toxic species produced can attack the photosensitizer molecules, decreasing the quantity of active drug.

1.4 Consequences of Photobleaching

Light incident perpendicular to the surface of a homogenous medium will be attenuated approximately exponentially with respect to depth. As a result, the fluence rate closest to the surface will be greatest, as will the absorption by the photosensitizer and subsequent photobleaching rate. As the drug near the surface bleaches, fewer photons are absorbed, allowing for deeper penetration into the medium. In other words, there is less "self-shielding" by the photosensitizer. Not only does this allow for increased treatment depth, it also has important implications in PDT dosimetry. Potter (1986) and Moan (1986) first recognized that if necrosis in PDT is a threshold process, meaning cell death occurs only if the amount of toxic species produced surpasses a minimum value, then photobleaching will prevent local necrosis in tissues where the initial concentration of photosensitizer is below a certain minimum. The continuous photodegredation will exhaust the supply of drug before enough toxic product can be created to exceed the threshold. Thus, the differential retention of photosensitizers by normal and malignant tissues can be further exploited to prevent undesired damage. This has led to decreased drug doses in an attempt to prevent skin photosensitivity (Boyle and Potter 1987).

Also important to PDT dosimetry is the decrease in emitted fluorescence as the photosensitizer photobleaches. The amount of fluorescence emitted and the instantaneous yield of toxic products are both proportional to the quantity of photosensitizer present in the tissue. Correlations have been made between the photobleaching rate observed by decreasing fluorescence and decreasing concentration of photosensitizer found by chemical analysis of biopsied tissue (Potter 1986). Thus, if this decreasing fluorescence signal is measured during clinical PDT treatments (Mang *et al*

1987 and Potter 1986), it should be possible to make predictions about the modified drug distribution within the tumour and the resulting necrosis.

1.5 Current Dosimetry Techniques and Inherent Difficulties

Photodynamic therapy dosimetry is based on three interdependent primary treatment variables: photosensitizer concentration, light fluence and oxygen concentration. The photosensitizer absorption alters the light distribution, while light causes photobleaching of the photosensitizer. Both the photosensitizer and light together react to deplete tissue oxygenation leading to a decrease in toxic species production.

Currently, when PDT is performed in a clinical setting, protocols consider the light and photosensitizer to be independent variables, and administered drug and light doses are based mainly on clinical experience. At the same time, oxygen and many additional secondary factors such as the variation of optical absorption and scattering coefficients between different tissues and patients (Wilson *et al* in press), differences in drug uptake by tumours, and the incident fluence rate are generally not considered. Given the growing evidence that these factors are essential to dose calculations (Wilson *et al* in press), current dosimetric techniques require improvement in order to provide more accurate information during treatment.

Usually, the approach has been to make measurements of all relevant factors including light fluence rate, photosensitizer concentration and tissue optical properties in order to predict photodynamic effect. This has been called "explicit" dosimetry. Few assumptions need be to made, aside from those concerning reaction mechanisms, however it is difficult to obtain a complete data set considering the equipment required and invasive nature of some measurements thereby limiting this approach. It also does not allow for monitoring during the treatment.

Recently, it has been postulated that a single dose metric, the fluorescence decrease due to photobleaching, is indicative of the photodynamic dose, and incorporates all variables and their interdependencies (Wilson *et al* in press). If this assumption holds, measurements of fluorescence would be sufficient to predict the delivered dose using this "implicit" approach.

The theory presented will attempt to discern mathematical relationships between the escaping fluorescence and extent of necrosis while minimizing the need to accurately determine initial treatment variables, such as tissue optical properties, photosensitizer concentration and bleach rate. This will allow for accurate, non-invasive monitoring of photodynamic dose during treatment, thus improving the overall efficacy of this cancer therapy.

2 THEORY

Diffusion theory accurately predicts the propagation of light through a medium in which scatter dominates absorption, as is the case for most tissues at PDT wavelengths (Svaasand and Gomer 1989). Tissue optics are described by the tissue absorption coefficient, μ_a, and the transport scatter coefficient, $\mu_s^{'} = (1-g)\mu_s$. This corresponds to isotropic scattering based on the similarity principle for scattering with anisotropy parameter g, which is the mean cosine of the scattering angle, and the scatter coefficient μ_s. When a photosensitizer is added the absorption coefficient becomes the sum of the endogenous tissue absorption coefficient μ_{a_o} and the photosensitizer absorption coefficient $\mu_{a(drug)}$. Knowing these optical properties, the fluence rate distribution $\Phi(\vec{r})$ can be found by solving the steady state diffusion equation

$$D\nabla^2\Phi(\vec{r}) - \mu_a\Phi(\vec{r}) = -S(\vec{r}) \tag{1}$$

where $S(\vec{r})$ is the source term, and D is the diffusion constant

$$D = [3(\mu_a + \mu_s^{'})]^{-1}. \tag{2}$$

Complicating the fluence rate distribution is the spatial variation in drug absorption coefficient resulting from photobleaching of the photosensitizer as treatment progresses. In order to solve this problem, a diffusion equation with a spatially dependant absorption coefficient is employed, and numerical methods are used to calculate the resulting fluence rate distribution and subsequent fluorescence emission. A pencil beam of fluorescence excitation light is also considered and detection of spatially resolved fluorescence is used to predict PDT progress. Finally, the diffusion equation in spherical co-ordinates is solved numerically to calculate the excitation fluence and resulting fluorescence distributions for an isotropic source in an infinite medium.

2.1 Bleaching of Photosensitizer -- Semi-infinite Medium, Broad-beam Irradiation

By using an "infinite" collimated source on a semi-infinite medium, the problem can be simplified to one dimension. The fluence rate and drug distributions are functions only of depth, z, giving

$$D(z)\frac{\partial^2}{\partial z^2}\Phi(z) - \mu_a(z)\Phi(z) = -S(z) \tag{3}$$

as the 1-D diffusion equation. After incident photons enter the medium, scattering events give rise to a distribution of diffuse, isotropic point sources according to

$$S(z) = S_o \mu_s' e^{-\int_0^z \mu_t(w)dw} \tag{4}$$

where S_o is the primary photon fluence rate at the surface and primary photons incident on the surface are exponentially attenuated according to the depth dependent total transport coefficient $(\mu_t(z) = \mu_a(z) + \mu_s^{'})$. Reorganization of equation 3 gives

$$\frac{\partial^2}{\partial z^2}\Phi(z) - \mu_{eff}^2(z)\Phi(z) = -3S_o\mu_s^{'}\mu_t(z)e^{-\int_0^z \mu_t(w)dw} \tag{5}$$

where $\mu_{eff}(z) = \sqrt{3\mu_a(z)\mu_t(z)}$ is the effective attenuation coefficient. An approximate general solution to this differential equation can be found using the WKB Method (Mathews and Walker 1970) which is valid if $\mu_{eff}(z)$ is slowly varying with respect to penetration depth

$$\Phi(z) \approx \frac{1}{\sqrt{\mu_{eff}(z)}}\left[ae^{+\int_0^z \mu_{eff}(w)dw} + be^{-\int_0^z \mu_{eff}(w)dw}\right]. \tag{6}$$

The boundary condition $\Phi(\infty) = 0$ requires that $a = 0$. By adding the diffuse scatter source term, the particular solution is obtained

$$\Phi(z) \approx \frac{b}{\sqrt{\mu_{eff}(z)}}e^{-\int_0^z \mu_{eff}(w)dw} + C(z)e^{-\int_0^z \mu_t(w)dw}. \tag{7}$$

The constant, b, can be found by considering the boundary conditions of the semi-infinite medium. For a non-scattering medium adjacent to the tissue having a matched refractive index, photons leaving the tissue will not return. This can be described by the partial current boundary condition (Keijzer *et al* 1988)

$$\Phi(0) - 2D(z)\frac{\partial}{\partial z}\Phi(z)|_{z=0} = 0. \tag{8}$$

Generally, the refractive indices are mismatched, resulting in internal reflection at the boundary. This may be accounted for by adding a parameter A to make the boundary condition

$$\Phi(0) - 2AD(z)\frac{\partial}{\partial z}\Phi(z)|_{z=0} = 0. \tag{9}$$

This parameter may be determined using an approach developed by Groenhuis *et al* (1983) in which

$$A = \frac{1 + r_d}{1 - r_d} \tag{10}$$

where the ratio of the refractive indices (n_{rel}) is used to determine r_d, the internal diffuse reflectance

$$r_d = -1.440 n_{rel}^{-2} + 0.710 n_{rel}^{-1} + 0.668 + 0.0636 n_{rel}. \tag{11}$$

Substituting this into equation 7, the coefficient of the general solution term is found as

$$b = \left(\frac{-3\mu_t \mu_{eff}^{\frac{3}{2}}}{3\mu_t \mu_{eff} + 2A\mu_{eff}^2 + A\frac{\partial}{\partial z}\mu_{eff}} \right) \left(\left(1 + \frac{2}{3}A\right) C(z)|_{z=0} - \frac{2A}{3\mu_t}\frac{\partial}{\partial z} C(z)|_{z=0} \right) \qquad (12)$$

where μ_t and μ_{eff} are evaluated at $z=0$.

Finally, a solution for $C(z)$ must be found. By explicitly solving the diffusion equation, the following second order differential equation is obtained

$$\frac{\partial^2}{\partial z^2}C(z) - 2\mu_t(z)\frac{\partial}{\partial z}C(z) + \left\{[\mu_t(z)]^2 - [\mu_{eff}(z)]^2 - \frac{\partial}{\partial z}\mu_t(z)\right\}C(z) + 3\mu_s'\mu_t(z) = 0. \qquad (13)$$

No analytic solution exists for this equation, and numerical methods must be used to determine $C(z)$.

As $z \rightarrow \infty$ there is no light penetration and thus no bleaching occurs. The photosensitizer absorption coefficient remains at its initial value and $\mu_t(z)$, $\mu_{eff}(z)$ and $C(z)$ are also unaltered. The derivatives of $C(z)$ and $\mu_t(z)$ with respect to z are zero, and equation 13 can be solved analytically as

$$C(z)_{z\rightarrow\infty} = -\frac{3\mu_s'\mu_{to}}{(\mu_{to})^2 - (\mu_{effo})^2} \qquad (14)$$

where μ_{to} and μ_{effo} are the initial attenuation coefficients. Using this result, an initial point z_i is chosen deep in the medium and fourth order Runge-Kutta (Gerald and Wheatley 1970) and Adams-Moulton (Gerald and Wheatley 1970) methods may be used to solve the differential equation numerically for all $z<z_i$. The addition of the primary photons to equation 7 gives the total fluence rate

$$\Phi(z) = S_o\left(\frac{b}{\sqrt{\mu_{eff}(z)}}e^{-\int_0^z \mu_{eff}(w)dw} + C(z)e^{-\int_0^z \mu_t(w)dw} + e^{-\int_0^z \mu_t(w)dw}\right). \tag{15}$$

This is the photon fluence which will photobleach the photosensitizer, resulting in a lower absorption coefficient.

Assuming first order kinetics, photobleaching of the drug is a time-dependent process according to

$$\mu_{a(drug)}(z,t) = \mu_{a(drug)}(z,0)e^{-\int_0^t \Phi(z,t')Bdt'} \tag{16}$$

where B is the experimentally determined bleach rate of the photosensitizer, Φ is the fluence rate, and t is the irradiation period. Before irradiation, the photosensitizer is assumed to be homogeneously distributed throughout the medium allowing for a fairly simple calculation of the initial fluence rate. The decrease in drug absorption coefficient can be calculated for a given bleach rate and time interval, giving rise to an altered fluence rate distribution. This process is repeated iteratively to calculate the spatially dependent drug distribution and fluence rate as the PDT irradiation progresses.

This algorithm was implemented as a computer program using Fortran. Stepsizes were optimized to give accurate results without requiring lengthy run times, or extremely large arrays. A stepsize of 0.01 millimetres was sufficiently small and the time increments began at 0.05 seconds and were gradually increased to 10 seconds since the photobleaching effects are much slower as time progresses. A maximum depth of 30 millimetres was set which was beyond the range of any significant photobleaching.

The resulting relationship between fluence rate and depth for a typical simulation is illustrated in figure 2.1.1a, where the depth is plotted in penetration depths ($\delta = \frac{1}{\mu_{eff}}$). The standard initial conditions were: $\mu_{a(drug)} = 0.01$ mm^{-1}, $\mu_{a_o} = 0.01$ mm^{-1}, $\mu_s' = 1.00$ mm^{-1} and bleach rate = 0.05 cm^2/J. The progression of treatment with time is represented by the unitless quantity Ψ, equal to the incident fluence of photobleaching light multiplied by the bleach rate of the photosensitizer, defined as the "scaled photobleaching fluence." As treatment progresses, the photosensitizer bleaches (figure 2.1.1b) allowing photons to penetrate deeper into the medium. After a short period, the fluence rate at the surface has reached a maximum corresponding to the local absence of photosensitizer. As the process continues, the local fluence rate increases towards its maximum value, indicated by the dotted line, resulting when the local photosensitizer has been completely bleached away. Similar results were obtained by Patterson and Wilson (1994) using another approach.

By examining the decreasing photosensitizer absorption coefficient, the amount of toxic product created, and hence the depth of necrosis, can be calculated based on the quantity of drug that has been bleached. For example, the dashed line in figure 2.1.1b corresponds to an arbitrary necrosis threshold. Once the photosensitizer absorption coefficient drops below this value, enough toxic species have been produced to cause local tumour death. As a result, necrosis depth will increase with scaled bleaching fluence, as shown in figure 2.1.2. Initially, before enough photons have interacted with the tissue, none of the tumour is killed, however after a short period there is rapid necrosis over the first few millimetres due to the high fluence rate near the surface.

Another consequence of the threshold hypothesis is that the total yield of toxic photoproducts is limited to a value proportional to the initial photosensitizer concentration. If the initial drug concentration yields a total photoproduct concentration less than the threshold for tissue damage, then the treatment will be ineffective. Since photosensitive drugs target tumour cells, there should be a greater concentration present in the cancerous tissue than in the surrounding healthy tissue. Given the very short distance that singlet oxygen molecules diffuse before reacting, if this advantageous therapeutic ratio could be exploited it should be possible to destroy the tumour without extensive damage to healthy tissue (Patterson and Wilson 1994).

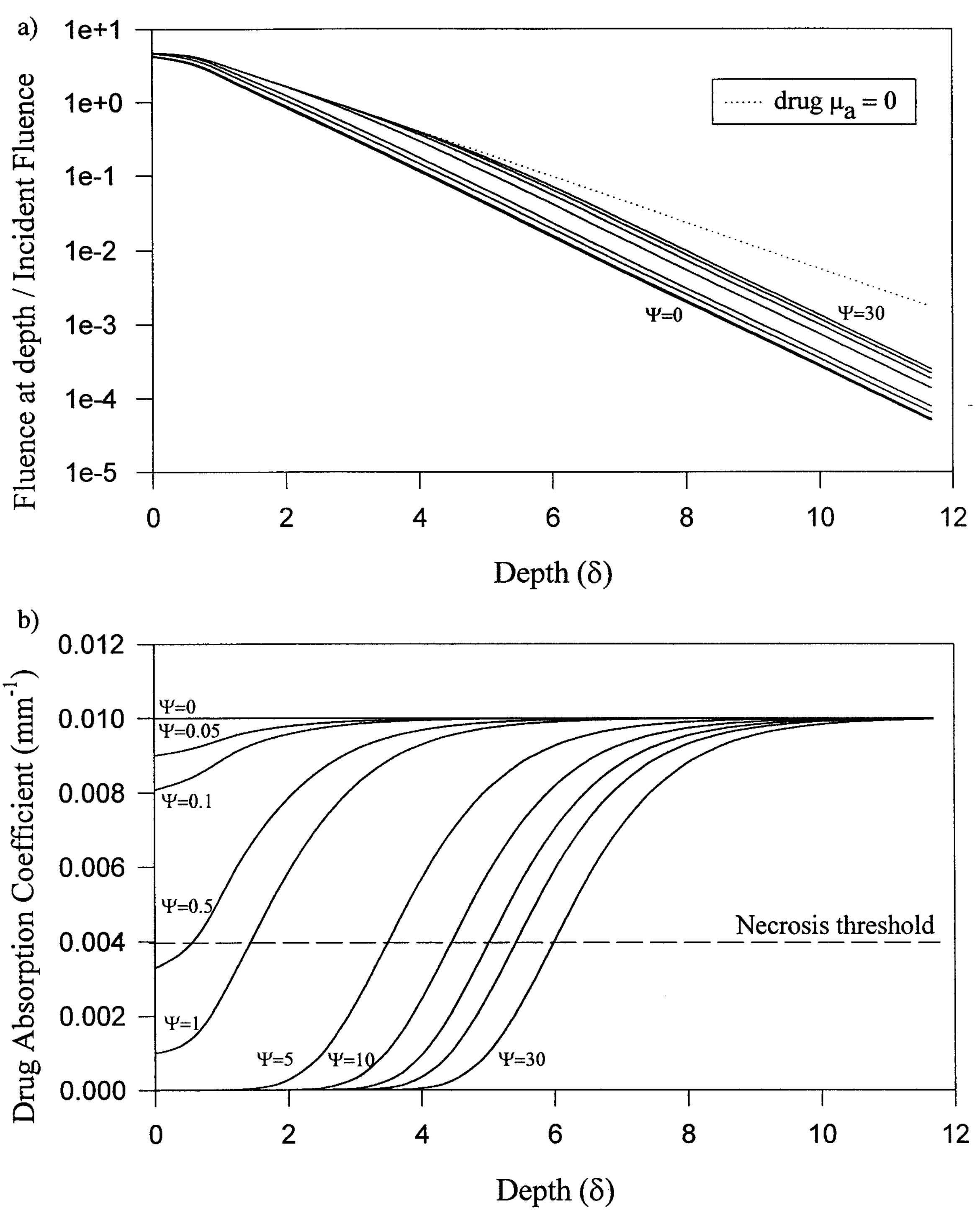

Figure 2.1.1 **a)** Fluence rate as a function of depth as treatment progresses for standard initial conditions. The photosensitizer distribution is initially uniform ($\mu_{a(drug)} = 0.01\ \mathrm{mm}^{-1}$) at $\Psi=0$.

b) Drug absorption coefficient versus depth for the same initial conditions. Necrosis occurs when drug μ_a falls below the indicated threshold.

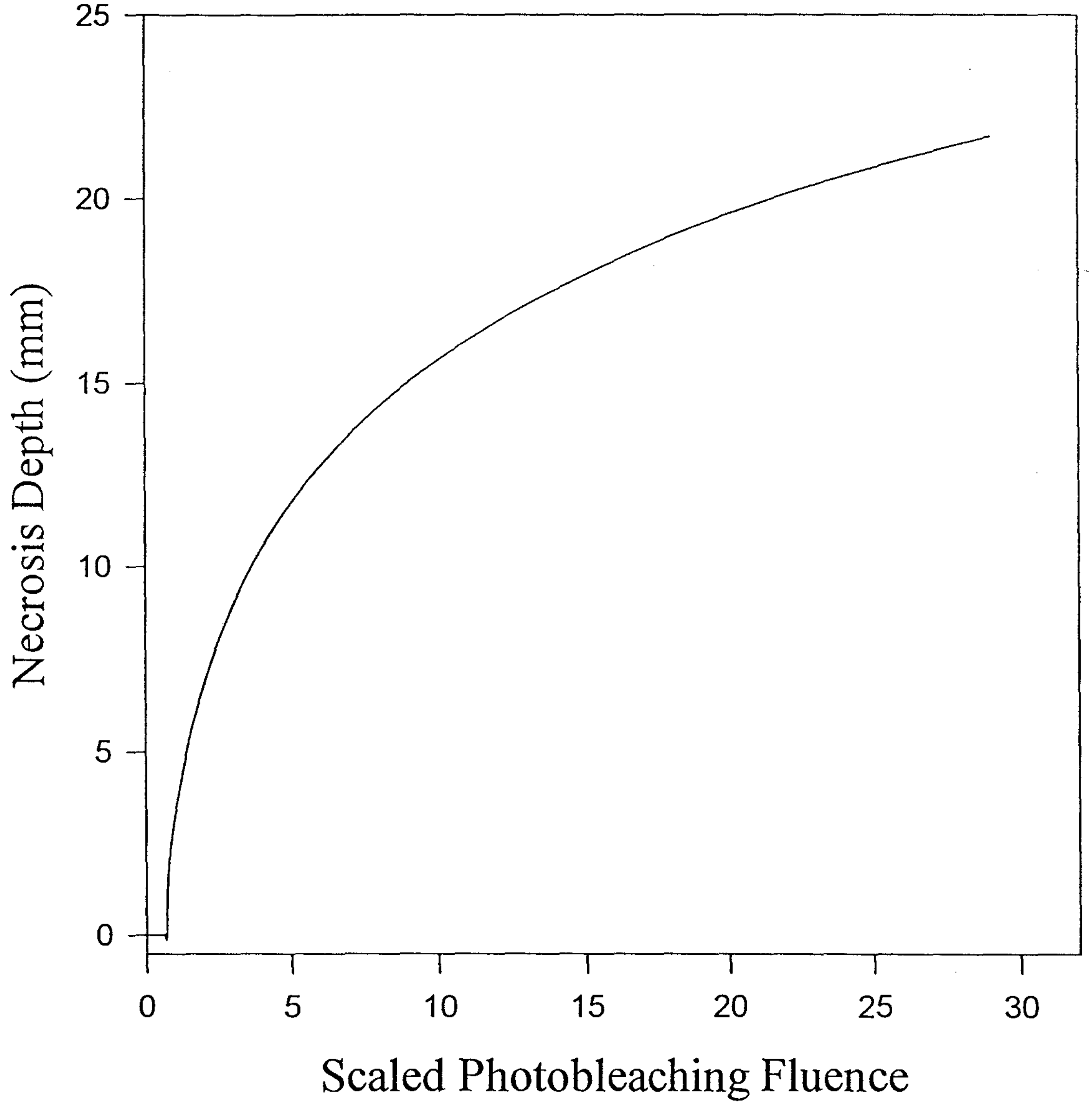

Figure 2.1.2 Increase in necrosis depth as treatment progresses using standard initial conditions. For necrosis to occur, the photosensitizer absorption coefficient must decrease by 0.006 mm^{-1}.

2.2 Fluorescence Escape -- Semi-infinite Medium, Broad-beam Excitation

Knowing the excitation light fluence rate from an infinite source and the drug distribution, the local fluorescence emission rate is calculated as the product of the local fluence rate, the drug absorption coefficient and the quantum yield for fluorescence, γ

$$f(z) = \Phi(z)\mu_{a(drug)}(z)\gamma. \tag{17}$$

To determine the fraction that escapes to the surface, the following approach is used. Consider a uniform layer of fluorescence at depth z_o to be a collection of identical isotropic point sources. Although the drug concentration is spatially dependent, the tissue optical properties are homogeneous at the fluorescence emission wavelength because the assumption is made that the photosensitizer does not absorb at this wavelength. The boundary condition at $z=0$ can be satisfied by introducing a layer of negative "image sources" which force the fluorescence to zero at an extrapolated boundary found at position $z_b = 2AD$ (Farrell *et al* 1992), where A is related to the internal diffuse reflectance (equation 10). If the point sources are considered individually, the Green's function will give an expression for the fluorescence fluence rate at any point (ρ,z) in a semi-infinite medium by summing the solutions for the point source at $(0,z_0)$ and its corresponding image source (figure 2.2.1)

$$f(\rho, z; 0, z_o) = \frac{1}{4\pi D}\left(\frac{e^{-\mu_{eff} r_1}}{r_1} - \frac{e^{-\mu_{eff} r_2}}{r_2}\right) \tag{18}$$

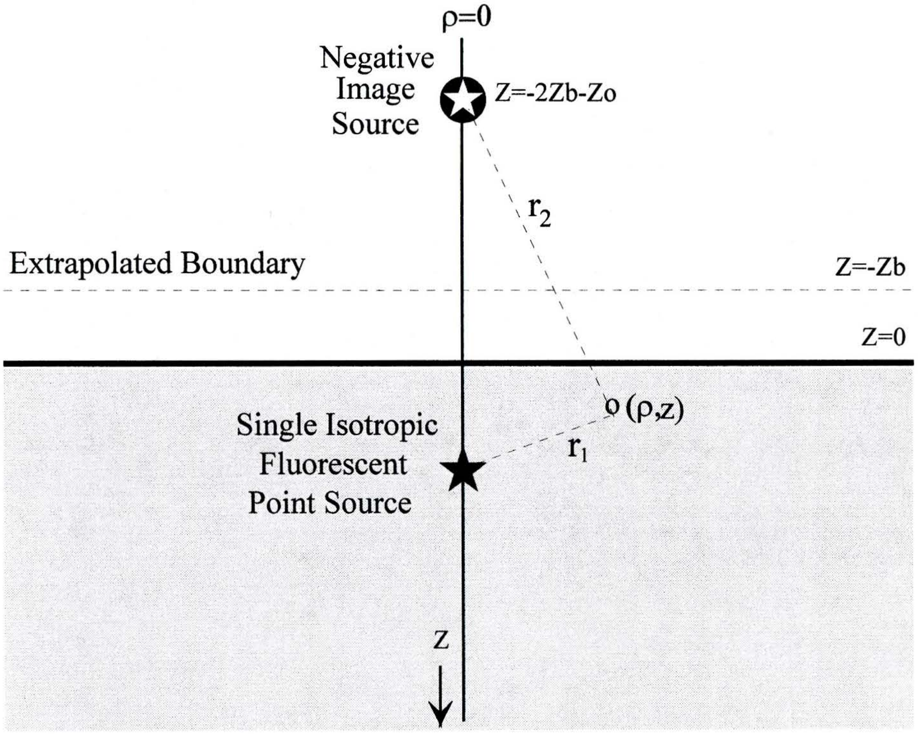

Figure 2.2.1 A single isotropic point source in a semi-infinite medium and its corresponding image source equidistant from the extrapolated boundary. Summation of the fluence rates from the two sources will give the fluorescence at any point (ρ, z).

where

$$r_1 = \sqrt{(z-z_o)^2+\rho^2}\,, \text{ and } r_2 = \sqrt{(z+z_o+2z_b)^2+\rho^2}\,. \tag{19}$$

For fluorescence, the quantity of interest is the photon current, F, leaving the medium at $z=0$, given by the gradient of the fluence rate (Farrell *et al* 1992)

$$F(\rho,0;0,z_o) = -D\nabla f(\rho,z;0,z_o)|_{z=0}\,. \tag{20}$$

Combining equations 18 and 20 gives

$$F(\rho,0;0,z_o) = \frac{1}{4\pi}\left[z_o\left(\mu_{eff}+\frac{1}{r_1}\right)\frac{e^{-\mu_{eff}r_1}}{r_1^2} + (z_o+2z_b)(\mu_{eff}+\frac{1}{r_2})\frac{e^{-\mu_{eff}r_2}}{r_2^2}\right]. \tag{21}$$

Now, the total fluorescence reaching any point at the surface from all sources at depth z_o is the adjoint problem to the total fluorescence reaching the surface from a single fluorescence point source at the same depth, given by

$$\begin{aligned} F(0;z_o) &= \int_0^\infty F(\rho,0;0,z_o)2\pi\rho d\rho \\ &= \tfrac{1}{2}\left(e^{-\mu_{eff}z_o} + e^{-\mu_{eff}(z_o+2z_b)}\right). \end{aligned} \tag{22}$$

Knowing $z_b = 2AD = \frac{2A}{3\mu_t}$, this simplifies to

$$F(0;z_o) = \tfrac{1}{2}e^{-\mu_{eff}z_o}\left(1+e^{\frac{-4A\mu_{eff}}{3\mu_t}}\right) \tag{23}$$

which describes the fluorescence escape at any point on the boundary $z=0$ from a layer of fluorescence at $z=z_o$.

The total fluorescence reaching the surface from all depths is the integral of the product of the depth dependent fluorescence source strength (equation 17) and the escape probability (equation 23)

$$F(0) = \gamma \int_0^\infty F(0; z_0)\Phi(z_o)\mu_{a(drug)}(z_o)dz_o \tag{24}$$

which must be solved numerically.

Anywhere on the surface of the semi-infinite medium the fluorescence signal will decrease according to the curve depicted in figure 2.2.2a which is not a simple exponential as would be expected if tissue optics had no effect. The necrosis depth calculations performed by the bleaching algorithm (figure 2.1.2) can be compared with the fluorescence emission, depicted in figure 2.2.2b (direction of time is from right to left). At early times, the fluorescence signal decreases before surface toxicity has exceeded the threshold for necrosis, resulting in a flat line. Then, once the toxicity threshold has been exceeded near the surface, the depth of necrosis increases in proportion to a logarithmic decrease in the observed fluorescence signal. This simple relationship may allow prediction of necrosis depth from observation of the fluorescence signal during treatment.

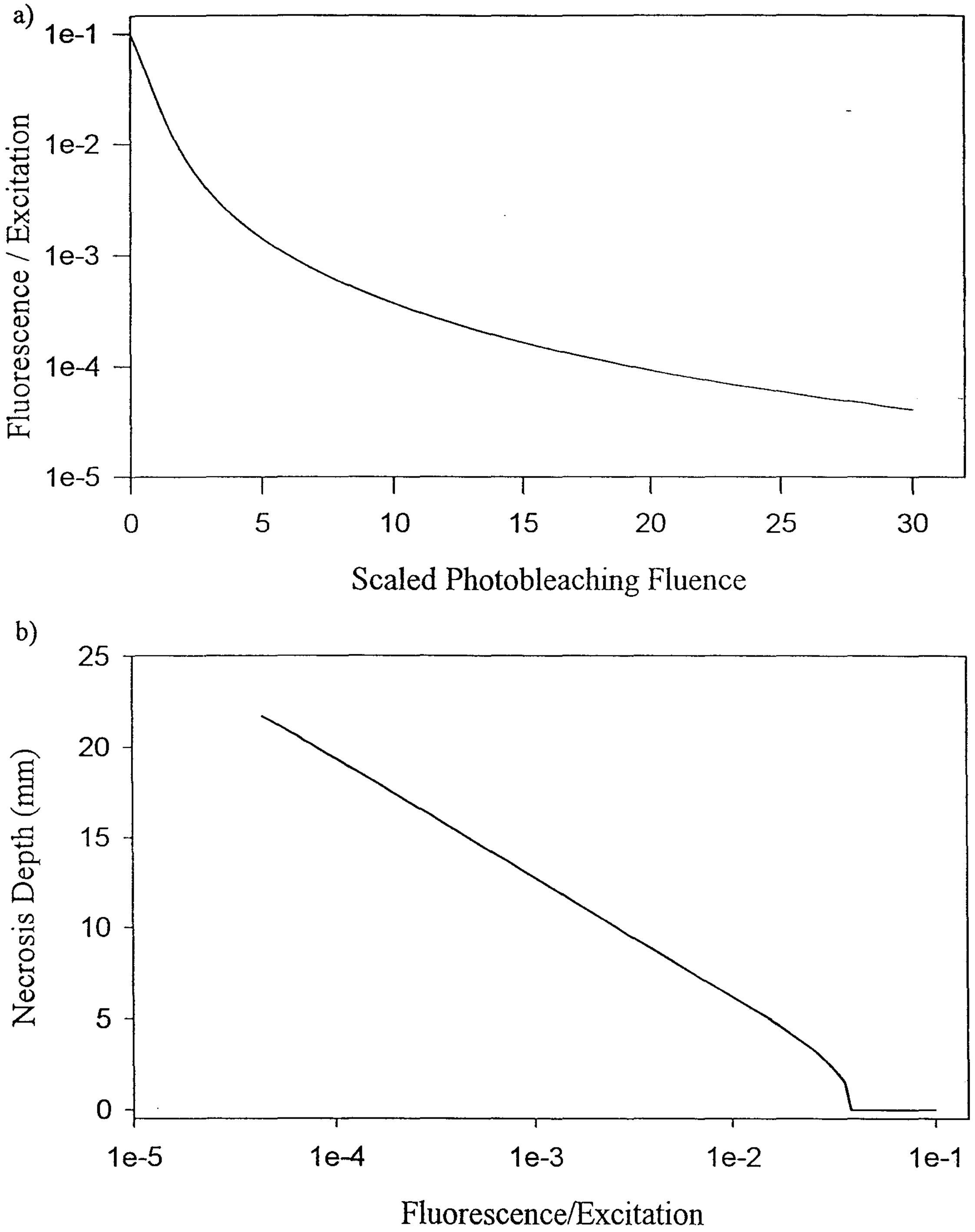

Figure 2.2.2 **a)** 690 nm fluorescence at the surface for irradiation with a broad-beam 630 nm light source. Standard initial treatment conditions were used.
b) Decrease in fluorescence signal as depth of necrosis increases (direction of time proceeds from right to left).

2.3 Fluorescence Escape -- Semi-infinite Medium, Pencil Beam Excitation

In contrast with the broad-beam source, a pencil beam of excitation light will give rise to an excitation fluence rate distribution that has radial variation. Integration of the product of the excitation fluence rate, local drug absorption coefficient and escape probability will provide a distribution of emitted fluorescence that varies with distance from the source. Spatially resolved fluorescence measurements might be able to provide more information than the single measurement obtained using an infinite source. A short fluorescence measurement could easily be made during treatment using an optical fibre based probe. Although an optical fibre source would not provide a well-collimated beam, this assumption is made to simplify the mathematics. The excitation light would be delivered through a central fibre, while fluorescence would be collected by several fibres at known radii.

2.3.1 Highly Scattering Medium

A pencil beam of excitation light perpendicular to the surface of a highly scattering ($\mu_s^{'} > \mu_a$) semi-infinite medium will give rise to a line of scattering events in the medium according to

$$S(\vec{r}) = S_o \mu_s^{'} e^{-(\mu_s^{'} + \mu_{ao})z} \delta(r) \tag{25}$$

which produces a complicated excitation fluence rate distribution. A simpler alternative is to assume all initial interactions take place at a single scattering site located at a depth of one mean free path ($z_o = \frac{1}{\mu_t^{'}}$) giving

$$S(z) = S_o \frac{\mu_s^{'}}{\mu_t^{'}} \delta(z - \frac{1}{\mu_t^{'}}) \delta(r). \tag{26}$$

If, for simplicity, we assume that $\mu_{a(drug)} \ll \mu_s^{'} + \mu_{a_o}$ at the excitation wavelength, neither the depth of this single scattering site nor the distribution of excitation light will be affected by the photosensitizer. Assuming an isotropic scatter source, the excitation fluence rate distribution at any point (ρ_s, z_s) from a source at $(0, z_o)$ can be described by Green's function, again making use of a negative image source to satisfy boundary conditions for a semi-infinite medium

$$\phi_{ex}(\rho_s, z_s; z_o) = S_o \frac{\mu_s^{'}}{\mu_t^{'}} \frac{1}{4\pi D_{ex}} \left(\frac{e^{-\mu_{effex} r_1}}{r_1} - \frac{e^{-\mu_{effex} r_2}}{r_2} \right) \tag{27}$$

where

$$r_1 = \sqrt{(z_s - z_o)^2 + \rho_s^2} \text{ and } r_2 = \sqrt{(z_o + 2z_{b+} z_s)^2 + \rho_s^2}. \tag{28}$$

Since the photosensitizer absorption is considered very low when compared with tissue absorption,

$$\mu_{eff_{ex}} = \sqrt{3(\mu_s^{'} + \mu_{a_o})\mu_{a_o}} \text{ and } D_{ex} = [3(\mu_s^{'} + \mu_{a_o})]^{-1}. \tag{29}$$

The resulting fluorescence source distribution is described by a three-dimensional distribution of isotropic point sources, symmetric about the incident excitation beam $(\rho = 0)$

$$f(\rho_s, z_s) = \phi_{ex}(\rho_s, z_s) \mu_{a(drug)_{ex}}(z_s) \gamma \tag{30}$$

denoting the quantum yield for fluorescence by γ. The subscript s indicates the fluorescent sources. Green's function is again appropriate for describing the fluorescent light fluence rate distribution at any point (ρ', z') from any source (ρ_s, z_s) as shown in figure 2.3.1 and described by

$$\phi_{fl}(\rho', z'; \rho_s, z_s) = f(\rho_s, z_s)\frac{1}{4\pi D_{fl}}\left(\frac{e^{-\mu_{eff_{fl}} r'_1}}{r'_1} - \frac{e^{-\mu_{eff_{fl}} r_2'}}{r'_2}\right) \tag{31}$$

where

$$r'_1 = \sqrt{(z' - z_s)^2 + (\rho' - \rho_s)^2} \text{ and } r'_2 = \sqrt{(z' + z_s + 2z_b)^2 + (\rho' - \rho_s)^2}\,. \tag{32}$$

At the fluorescence wavelength there is very little re-absorption by the photosensitizer and as a result photobleaching has minimal effects on light propagation. Thus, $\mu_{eff_{fl}}$ and D_{fl} are considered constant with respect to depth.

The magnitude of the radial distance can be re-expressed to allow for integration with respect to angle

$$|\rho' - \rho_s| = \sqrt{\rho_s^2 + \rho'^2 - 2\rho_s\rho' \cos\theta} \quad ; 0 \le \theta \le 2\pi. \tag{33}$$

Only the fluorescence at the surface (*z'=0*) is of interest, giving

$$r'_1 = \sqrt{{z_s}^2 + \rho_s^2 + \rho'^2 - 2\rho_s\rho' \cos\theta} \text{ and } r'_2 = \sqrt{(z_s + 2z_b)^2 + \rho_s^2 + \rho'^2 - 2\rho_s\rho' \cos\theta}\,. \tag{34}$$

Integrating equation 31 over all dimensions will give the total fluorescence fluence rate at any point on the surface

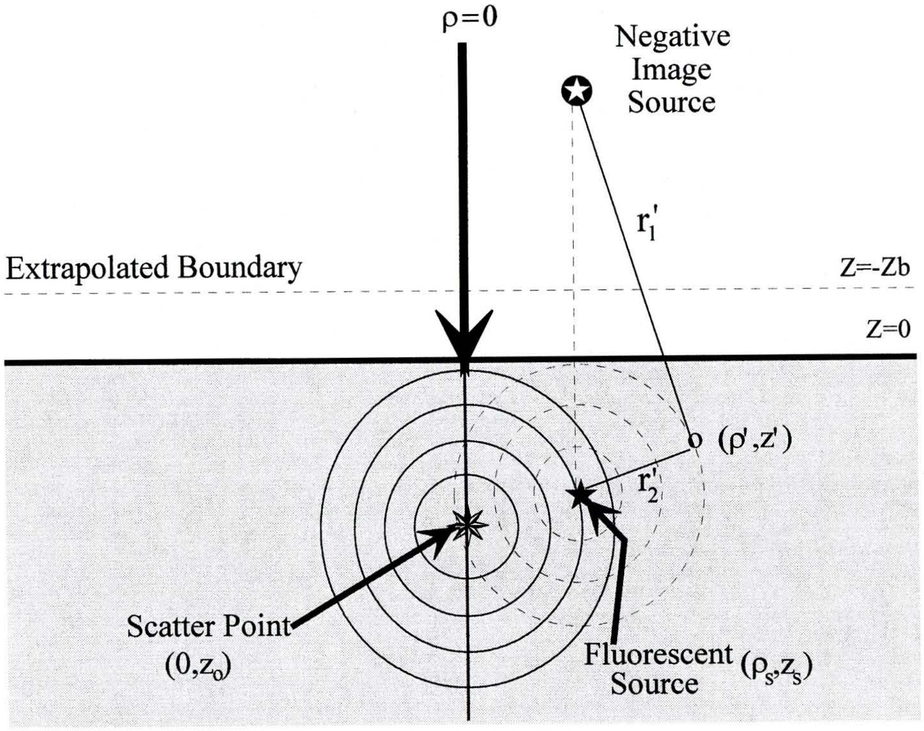

Figure 2.3.1 A pencil beam of excitation light incident on a highly scattering, semi-infinite medium. For a single scatter point, the excitation light distribution can be calculated, leading to a distribution of fluorescence sources. A negative image source satisfies boundary conditions and allows for the determination of fluorescence at any point (ρ', z').

$$\phi_{fl}(\rho',0) = \int_0^{\infty}\int_0^{\infty}\int_0^{2\pi} \phi_{fl}(\rho',0;\rho_s,z_s)d\theta\rho_s d\rho_s dz_s \tag{35}$$

$$= S_o\frac{\mu_s'}{\mu_t'}\frac{\Phi}{(4\pi)^2 D_{ex}D_{fl}}\int_0^{\infty}\int_0^{\infty}\int_0^{2\pi}\mu_{a(drug)_{ex}}(z_s)\left[\begin{array}{c}\frac{e^{-(\mu_{effex}r_1+\mu_{efffl}r_1')}}{r_1r_1'} - \frac{e^{-(\mu_{effex}r_2+\mu_{efffl}r_1')}}{r_2r_1'} \\ -\frac{e^{-(\mu_{effex}r_1+\mu_{efffl}r_2')}}{r_1r_2'} + \frac{e^{-(\mu_{effex}r_2+\mu_{efffl}r_2')}}{r_2r_2'}\end{array}\right]d\theta\rho_s d\rho_s dz_s$$

which cannot be solved analytically.

Figure 2.3.2a shows the decrease in fluorescence for several detection fibres at 0.33 mm increments from the source as treatment progresses. The simulation uses 630 nm light for fluorescence excitation and assumes tissue scattering and absorption properties are identical for excitation and escape photons and that fluorescence re-absorption does not occur. The standard initial conditions for a highly scattering medium at 630 nm were: $\mu_{a(drug)}$= 0.02 mm^{-1}, μ_{a_o}= 0.04 mm^{-1}, μ_s'= 1.50 mm^{-1} and bleach rate = 0.10 cm^2/J. A better visualization of the variation between fluorescence signals as the scaled photobleaching fluence increases is seen in figure 2.3.2b, where the fluorescence is normalized to the closest detector fibre. The effects are most prominent as the photosensitizer near the surface bleaches since the close fibres with the shortest paths from the source are highly influenced by drug concentration at shallow depths.

At each distance the fluorescence signal can be compared with the necrosis depth calculated during the broad-beam bleaching (figure 2.3.3). Not surprisingly, these are qualitatively similar to the relationship obtained in the one-dimensional model (figure2.2.3b) but now many sets of data exist. All of these curves provide the same

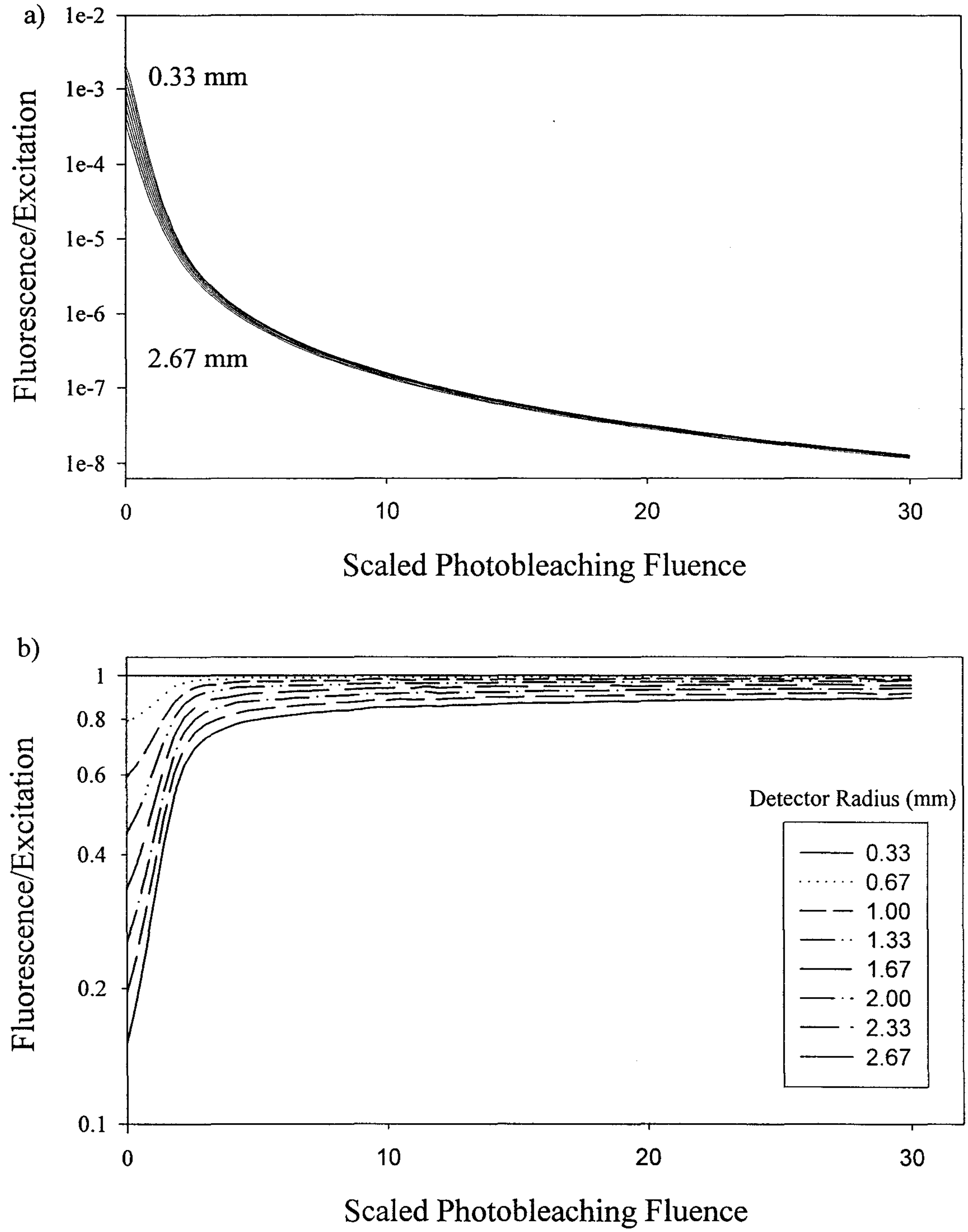

Figure 2.3.2 **a)** Fluorescence observed at eight radii (0.33 mm increments) from a pencil beam excitation source as scaled bleaching fluence increases. Standard conditions for a highly scattering medium were used.

b) Normalization to a single radius (0.33 mm) allows the variation between fibres to be seen more clearly.

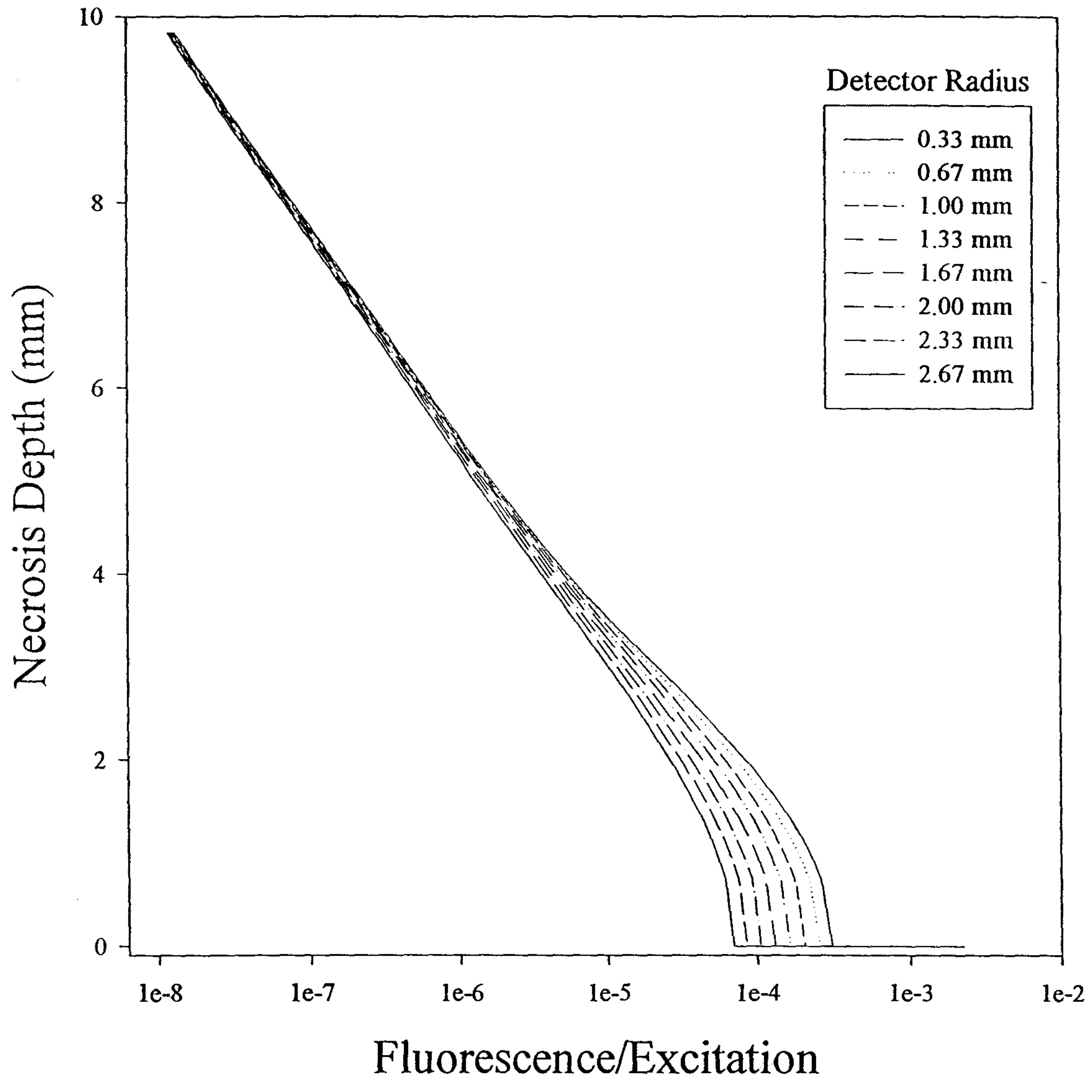

Figure 2.3.3 Comparison of necrosis depth versus fluorescence emission at eight detection radii (progresses from right to left) for broad-beam photobleaching and pencil beam excitation of a highly scattering medium at 630 nm.

information as that for the broad beam fluorescence, and taken individually, nothing has been gained by adding spatial information. However, if the variation in fluorescence *between* fibres is examined, it may be possible to ascertain information about the photosensitizer distribution.

2.3.2 Virtual Plane Depth

During treatment, spatially resolved fluorescence can be measured periodically. In this form, the data does not provide obvious dosimetric information and requires further analysis in order to allow for treatment monitoring. Although it may be possible, it would be extremely time consuming to calculate the three-dimensional distribution of photosensitizer responsible for the emitted fluorescence. Instead, the following approach is taken. It is assumed that all fluorescence originates from a very thin layer at depth z_o, (termed the "virtual plane") which would produce spatially resolved fluorescence at the surface equivalent to that emitted from the three-dimensional distribution. By matching the observed fluorescence as a function of radius at any point during treatment (figure 2.3.4a) with the escape probability as a function of radius from a single depth, seen in figure 2.3.4b, the virtual plane depth can be determined as a function of time (figure 2.3.5a). The depth of the virtual plane is dependent on the depth distribution of photosensitizer, and hence increases as photobleaching occurs. Necrosis depth is also highly dependent on the distribution of photosensitizer and when the two are plotted against one another (figure 2.3.5b), they track very closely once necrosis begins.

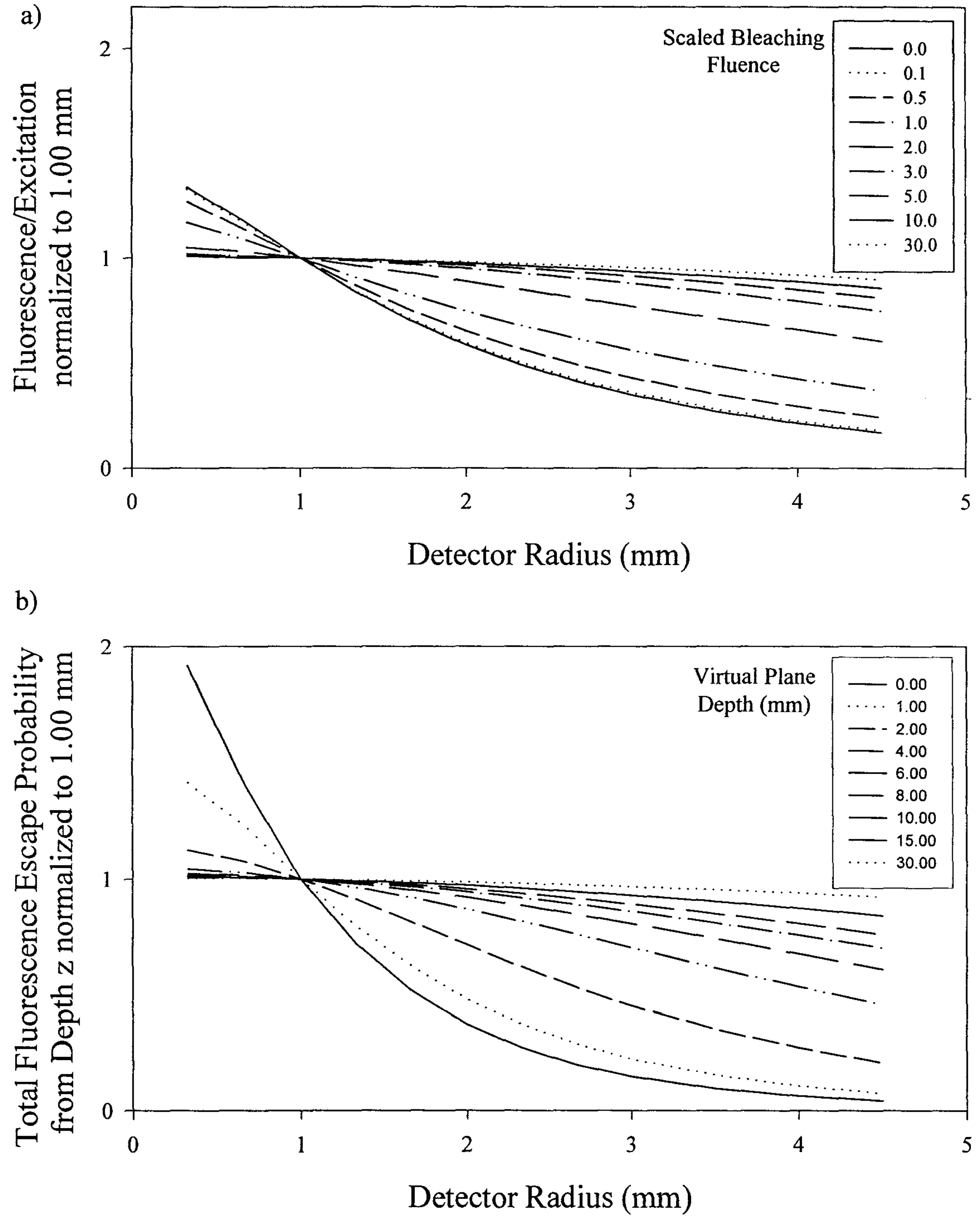

Figure 2.3.4 **a)** Normalized fluorescence as a function of detector radius as scaled photobleaching fluence increases using standard initial conditions.
b) Total probability of fluorescence escape for an single virtual plane versus detector radius for several depths, normalized to 1.0 mm.

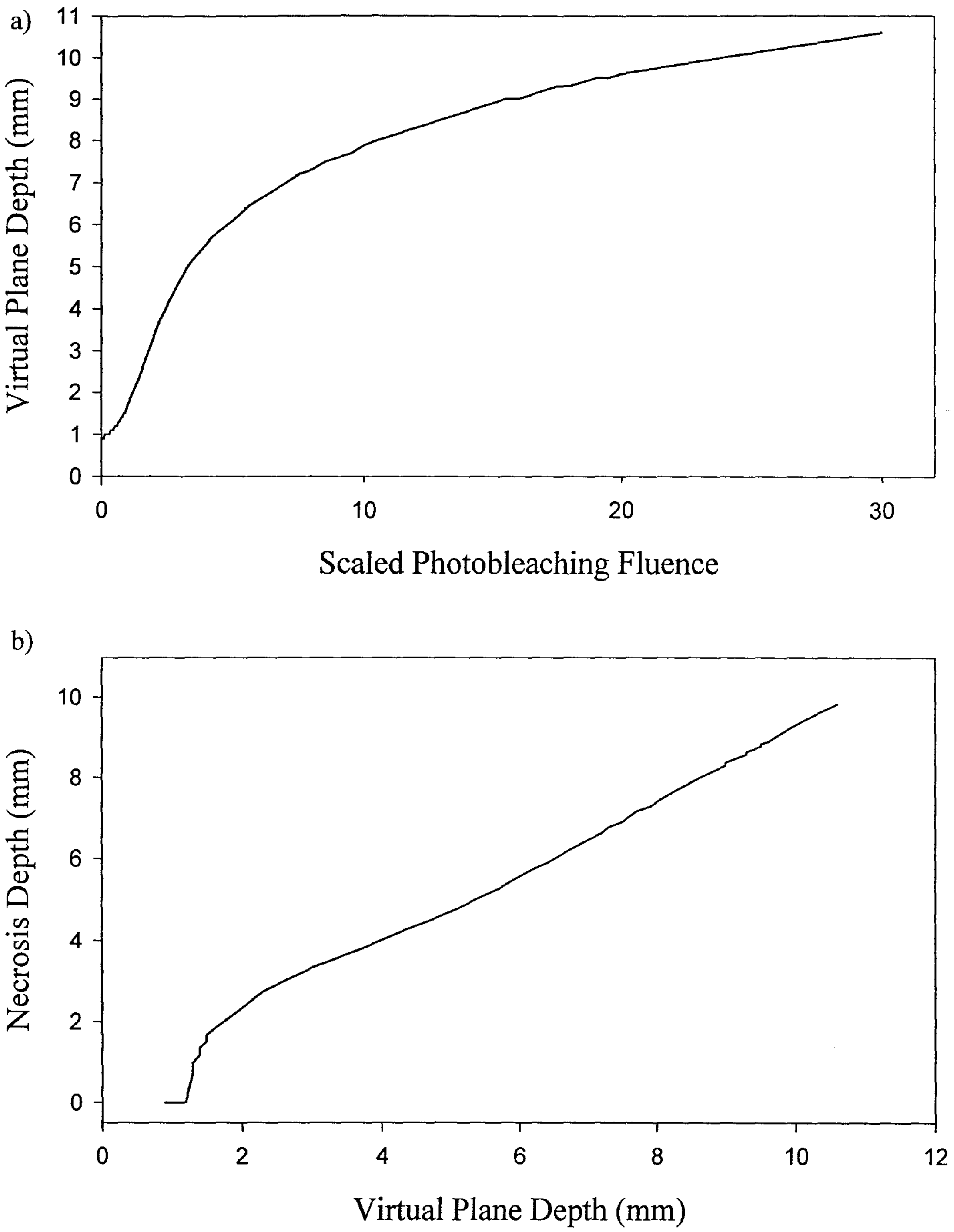

Figure 2.3.5 **a)** Progression of the virtual plane into the medium as scaled bleaching fluence increases. Standard scatter-dominated conditions were used.
b) Depth of necrosis as it relates to the effective depth of a single plane of fluorescence.

2.3.3 Highly Absorbing Medium

At the opposite extreme is a highly absorbing medium with low scattering ($\mu_a \gg \mu_s'$); an unlikely scenario when exciting fluorescence in human tissue with 630 nm light. The situation becomes much more plausible, however, if a shorter wavelength is used such that absorption by the photosensitizer and endogenous tissue chromophores is greatly increased. Given this assumption, a collimated incident light beam will give rise to a line of absorption events according to

$$\Phi(z) = \Phi_o e^{-\int_0^z \mu_a(w)dw} \tag{36}$$

where Φ_o is the source term proportional to the primary photon fluence rate at the surface. The line of absorption can also be considered a line of fluorescence sources (figure 2.3.6) with source strength

$$S_f(0,z) = \gamma\mu_{a(drug)}(z)e^{-\int_0^z \mu_a(w)dw} \tag{37}$$

again denoting the fluorescence quantum yield by γ Green's function can again be adopted (as in section 2.3.1) assuming diffusion theory holds at the longer fluorescence wavelengths. The photon current leaving the medium at $z=0$ from a point at depth z_o is given by equation 21 with

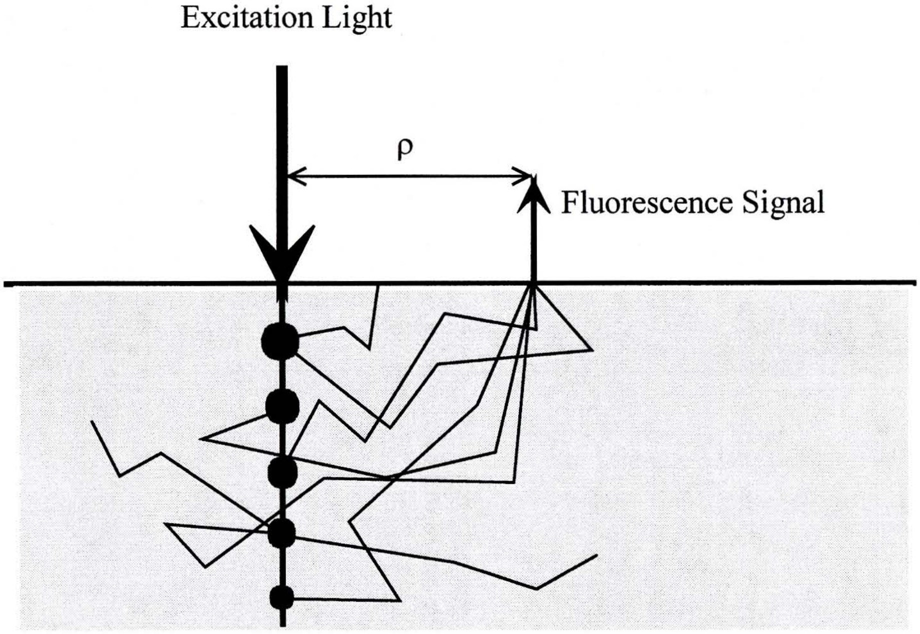

Figure 2.3.6 For pencil beam geometry, excitation light incident on the surface of a highly absorbing medium penetrates along the z-axis and is absorbed (no scattering). These absorption sites can be considered fluorescence point source emitting light which can be measured at the surface.

$$r_1 = \sqrt{z_o^2 + \rho^2}\,, r_2 = \sqrt{(z_o + 2z_b)^2 + \rho^2}\,. \tag{38}$$

The radially resolved fluorescence current reaching the surface is found by integrating the product of the source term and the fluorescence escape probability

$$F(\rho, 0; 0, z_o) = \tag{39}$$

$$\frac{\gamma}{4\pi}\int_0^{\infty}\left[\mu_{a(drug)}(z_o)e^{-\int_0^{z_o}\mu_a(z)dz}\left(z_o\left(\mu_{eff} + \frac{1}{r_1}\right)\frac{e^{-\mu_{eff}r_1}}{r_1^2} + (z_o + 2z_b)(\mu_{eff} + \frac{1}{r_2})\frac{e^{-\mu_{eff}r_2}}{r_2^2}\right)\right]dz_o$$

using numerical methods.

Whereas tissue scattering is assumed constant at all wavelengths, tissue and drug absorptions are higher at shorter wavelengths and as a result were set to be three times higher at the excitation wavelength than at the bleaching wavelength for the simulations. Consistent with the previous models, tissue optical properties are constant at the bleaching and fluorescence wavelengths, and the drug absorption is considered negligible for fluorescent light.

Although absorption by the photosensitizer is much greater and the fluence rate is much higher during measurements, photobleaching resulting from the fluorescence excitation light was considered negligible compared with that done by the broad-beam source since. This is justified by the fact that in an actual clinical situation the probe would be used only periodically to monitor the fluorescence decrease with short pencil beam excitations at random locations within the treatment area.

For excitation with a pencil beam source at 515 nm, figure 2.3.7a shows the fluorescence reaching the surface at eight detection radii. At this excitation wavelength, standard initial conditions were: $\mu_{a(drug)}$= 0.60 mm^{-1}, μ_{a_o}= 0.60 mm^{-1}, μ'_s=1.00 mm^{-1} and bleach rate = 0.10 cm^2/J, while both tissue and drug absorption are a factor of three lower at the bleaching wavelength. Variation between fibres is much more apparent in figure 2.3.7b where fluorescence is normalized to the closest fibre, showing results similar to those of the scatter dominated model. Once again, it is this difference between spatially resolved fluorescence measurements that can be exploited to obtain useful information.

2.3.4 Virtual Source Depth

Similar to the virtual plane idea, the absorption dominated situation makes use of a single "virtual source." Since the initial distribution of fluorescence sources is distributed along one dimension $(\rho = 0)$ simplification is easier than for the scatter dominated model, where the fluorescence sources occupy three dimensions. The assumption is made that all fluorescence originates from a single source located along $\rho = 0$ at a depth *d*, as shown in figure 2.3.8. It may described using a delta function

$$S(0, z) = \kappa\delta(z - d) \tag{40}$$

where κ is a constant multiplying the delta function. An expression for the virtual source depth can be found be examining the moments of *S(z)*. The zeroth moment is given by

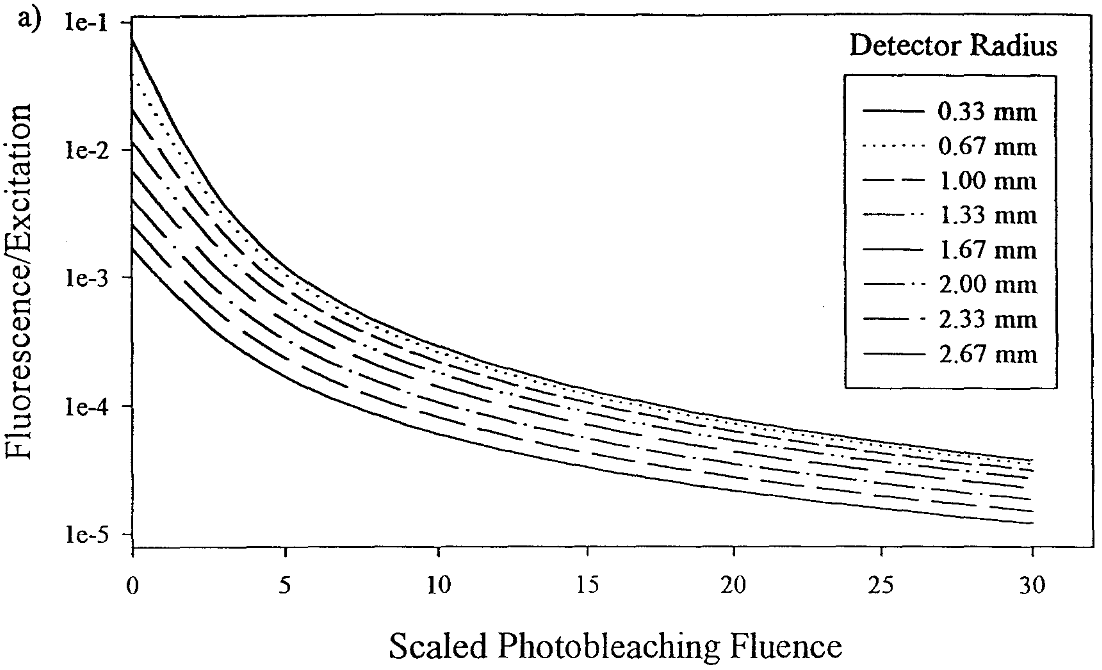

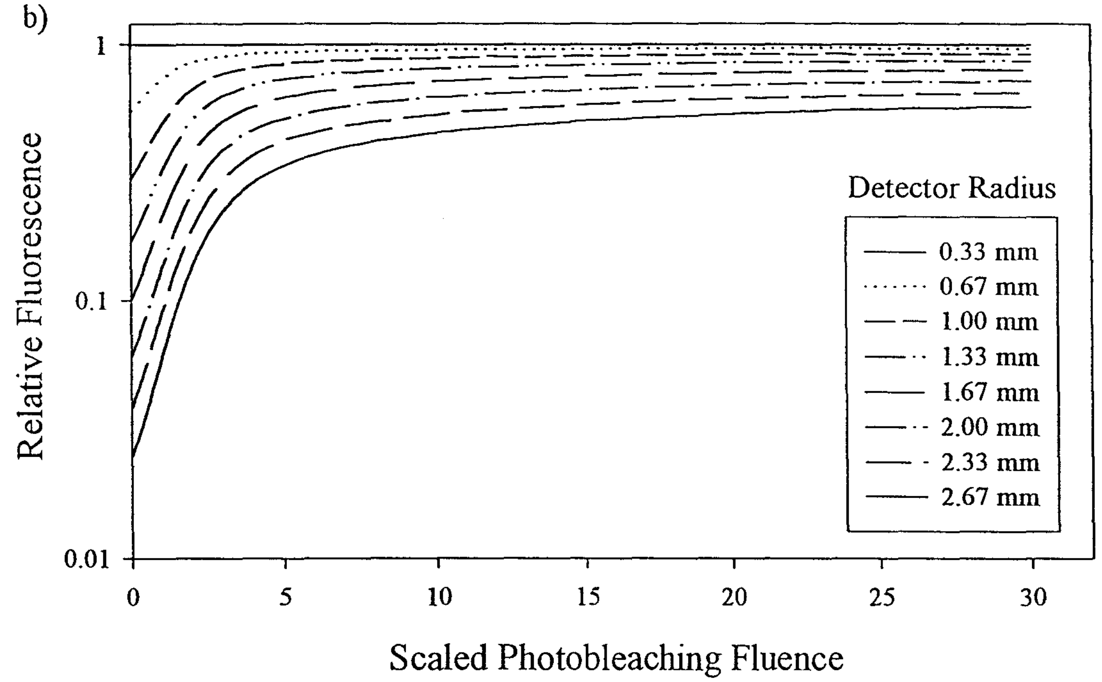

Figure 2.3.7 **a)** Radially resolved fluorescence as a function of scaled photobleaching fluence for a highly absorbing medium with standard initial conditions.
b) Normalization of the radially resolved fluorescence to 0.33 mm, exemplifying the variation between detection fibres.

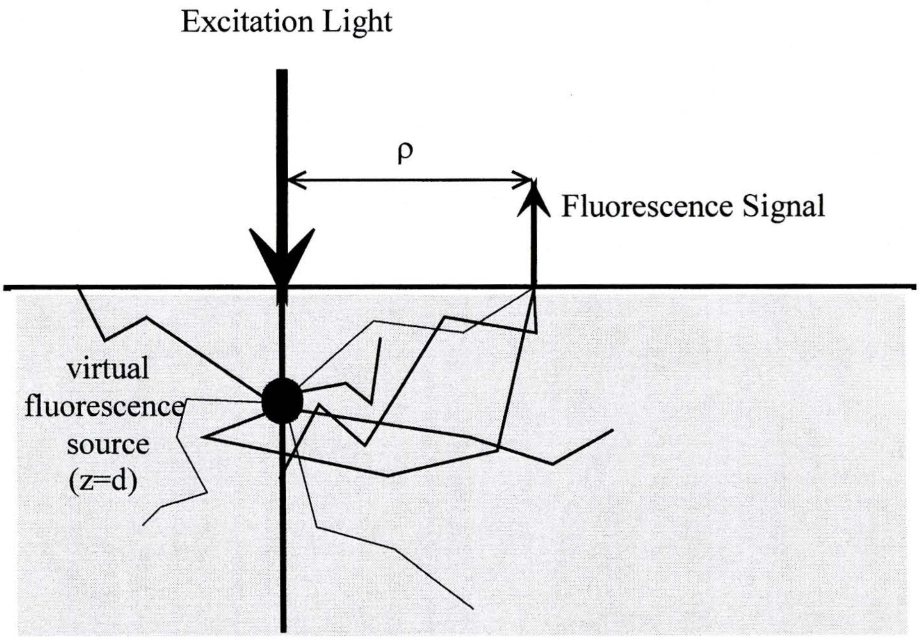

Figure 2.3.8 Illustration of the single virtual fluorescence source arising from a beam of excitation light on the surface of a highly absorbing, semi-infinite medium. The resulting radially resolved fluorescence at the surface is equivalent to that from a line of fluorescence sources along the z-axis.

$$\int_0^\infty S(0,z)dz = \int_0^\infty \kappa\delta(z-d)dz \;= \kappa \tag{41}$$

while the first moment is

$$\begin{aligned} \int_0^\infty zS(0,z)dz &= \int_0^\infty \kappa z\delta(z-d)dz \\ &= \kappa d. \end{aligned} \tag{42}$$

Dividing equation 42 by equation 41 gives the result

$$d = \frac{\int_0^\infty zS(0,z)dz}{\int_0^\infty S(0,z)dz}. \tag{43}$$

Reverting to equation 37 as the source term, the virtual source depth is easily calculated numerically. To find the radial fluorescence distribution that arises from this virtual source, the following relationship is developed

$$\begin{aligned} F(\rho,0) &= \int_0^\infty S(0,z)\, F(\rho,0;0,z)dz \\ &= \int_0^\infty \kappa\delta(z-d)\, F(\rho,0;0,z)dz \\ &= \kappa F(\rho,0;0,d). \end{aligned} \tag{44}$$

The constant κ is evaluated by substituting equation 37 into

$$\kappa = \int_0^\infty S(0,z)dz \tag{45}$$

which was previously evaluated when calculating *d*. Thus, the final result is an expression for the radially resolved fluorescence current at the surface which must be calculated using numerical techniques. It is important to note that the fluorescence distribution observed at the surface is virtually indistinguishable from that when a damped line of fluorescence sources is used.

The virtual source is observed to move deeper into the medium as the drug bleaches, as shown in figure 2.3.9a. Originally, the single source begins at a depth of one mean free path before any bleaching has occurred, and then penetrates deeper as upper layers become bleached. The relationship between calculated necrosis and virtual fluorsecence source depth depicted in figure 2.3.9b is similar to the virtual plane model. Since both values are related to the location of the bleached photosensitizer interface, some relationship is expected.

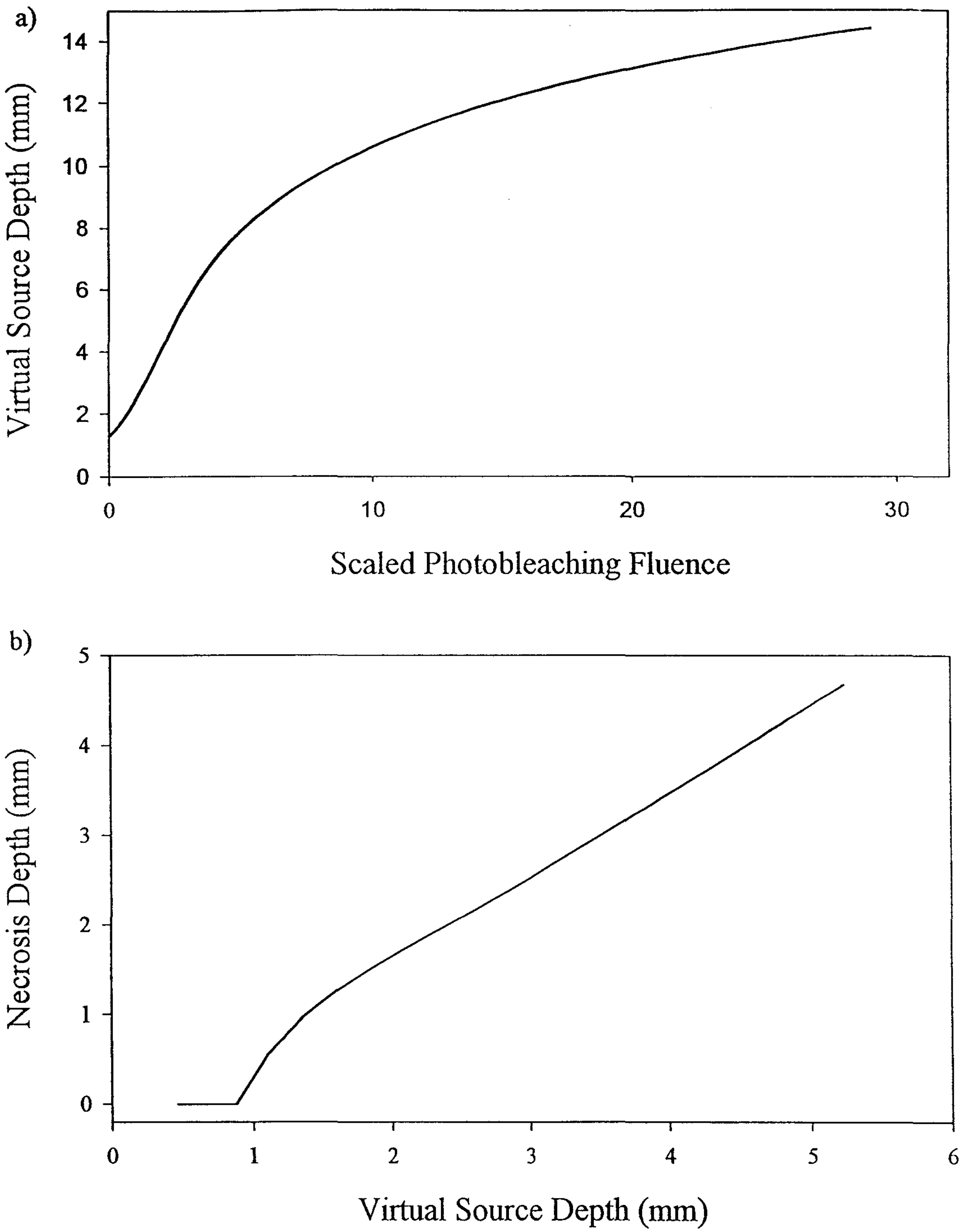

Figure 2.3.9 **a)** Virtual source depth penetration as treatment progresses for standard initial conditions.

b) Necrosis depth as a function of virtual source depth for an absorption dominated medium.

2.4 Bleaching of Photosensitizer -- Infinite Medium, Isotropic Point Source

Consider an isotropic photon source in an infinite medium. Due to spherical symmetry the diffusion equation in spherical co-ordinates will be a function only of radius

$$\left(\frac{\partial^2}{\partial r^2} + \frac{2}{r}\frac{\partial}{\partial r}\right)\Phi(r) - \mu_{eff}^2(r)\Phi(r) = \frac{P}{D(r)}\delta(0). \tag{46}$$

In this case, the source term is a delta function at $r=0$ with total power equal to P. Thus, at $r>0$

$$\frac{\partial^2}{\partial r^2}\Phi(r) + \frac{2}{r}\frac{\partial}{\partial r}\Phi(r) - \mu_{eff}^2(r)\Phi(r) = 0 \tag{47}$$

which can be solved by adopting the WKB Method (Mathews and Walker 1970), which yields the following result

$$\Phi(r) = \frac{ke^{-\int \mu_{eff}(r)dr}}{\sqrt{\mu_{eff}(r)}\, r}. \tag{48}$$

Since all photons must eventually be absorbed in an infinite medium, it is true that

$$\int_{volume} \Phi(r)\mu_a(r)dV = P. \tag{49}$$

Substituting in equation 48 and exploiting spherical symmetry,

$$P = k\int_0^\infty \frac{\mu_a(r)e^{-\int \mu_{eff}(r)dr}}{\sqrt{\mu_{eff}(r)}\,r}4\pi r^2 dr \tag{50}$$

which must be solved numerically. At any instant in time k is constant with respect to r, however k must be recalculated as the optical properties change due to photobleaching.

Bleaching of the drug as a function of time is calculated using the method described for the semi-infinite medium. Figure 2.4.1a shows the radial fluence distribution for several scaled bleaching fluences, beginning at one millimetre. Diffusion theory in spherical co-ordinates breaks down at very small radii leading to inaccurate results near the source where the fluence rate is high and bleaching occurs rapidly. However, the region of interest as far as photodynamic effect is concerned is several millimetres away, where diffusion theory is considered accurate. The fluence increases as treatment progresses due to a decrease in self-shielding by the photosensitizer as it photobleaches, with the dashed line representing an absence of photosensitizer everywhere. Near the source, the fluence reaches a maximum after complete photodegredation of the drug has occurred, as seen in figure 2.4.1b. Initially, the drug is uniformly distributed, followed by rapid bleaching close to the source where fluence rates are highest.

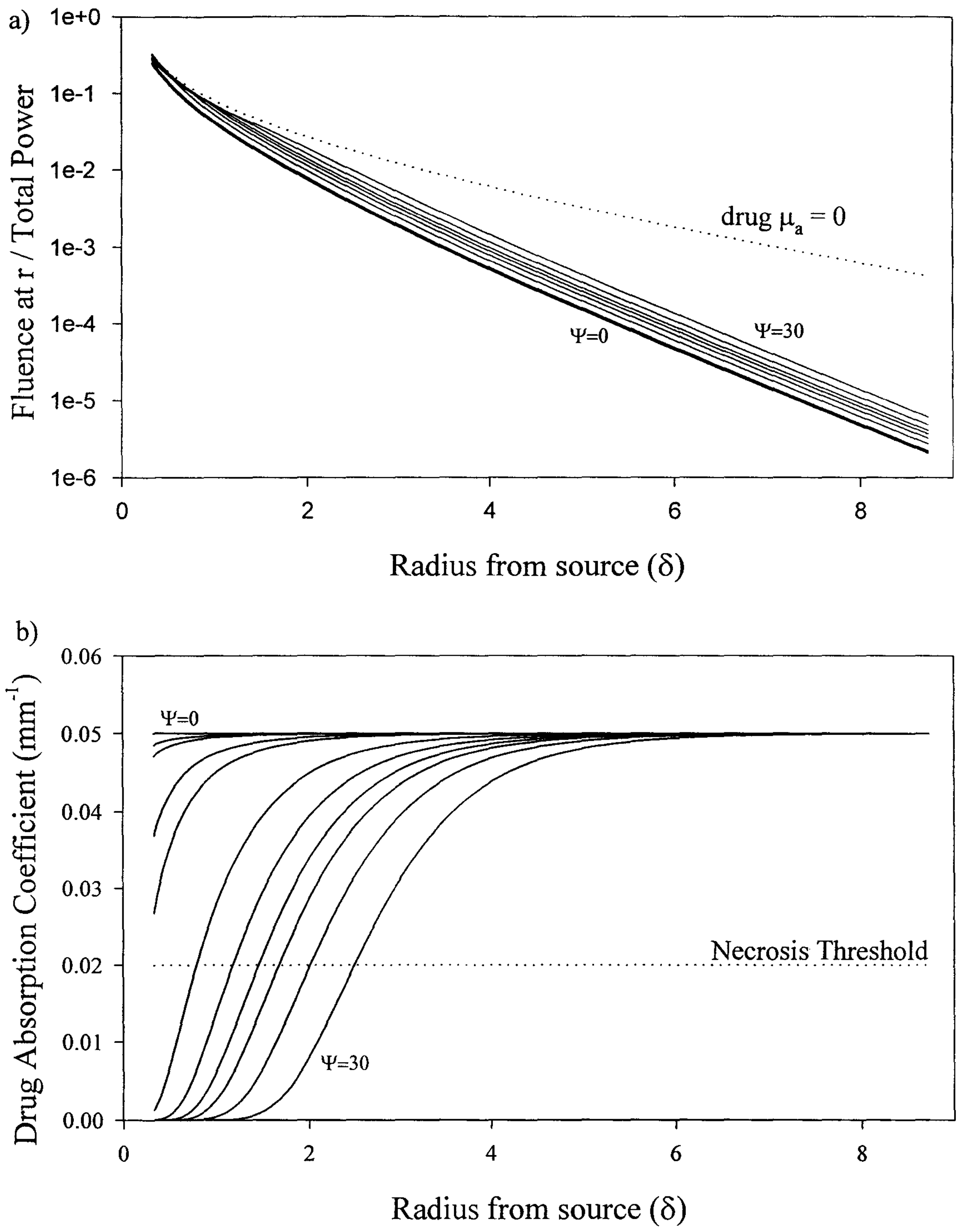

Figure 2.4.1 **a)** Excitation fluence versus radius (in penetration depths) originating from a spherical source in an infinite medium, using standard initial conditions. The dotted line indicates complete drug degradation.
b) Radial drug distribution for several scaled bleaching fluences. Necrosis occurs when $\mu_{a(drug)}$ falls below the indicated threshold.

2.5 Fluorescence -- Infinite Medium, Isotropic Excitation Source

The bleaching fluence is also responsible for exciting fluorescence. At any position, the rate of fluorescence production will be the local rate of excitation light absorbed by the drug multiplied by the quantum yield for fluorescence, γ

$$f(r) = \Phi(r)\mu_{a(drug)}(r)\gamma. \tag{51}$$

Since the excitation fluence rate is spherically symmetric, the fluorescence source distribution can be described as a distribution of fluorescent shells which themselves can be considered to be collections of identical isotropic point sources (figure 2.5.1). Fluorescence measurements are made at known distances from the source fibre. If the assumption is made that tissue optical properties are essentially homogeneous at the fluorescence emission wavelength, Green's function can again be used to describe the migration of fluorescence photons from the individual point sources

$$F(\rho) = f(r)\frac{1}{4\pi D}\frac{e^{-\mu_{eff}d}}{d}. \tag{52}$$

The distance from the single fluorescence source to the detector can be expressed in relation to the source/detector distance ρ, the radius of the fluorescence point r, and the angle θ

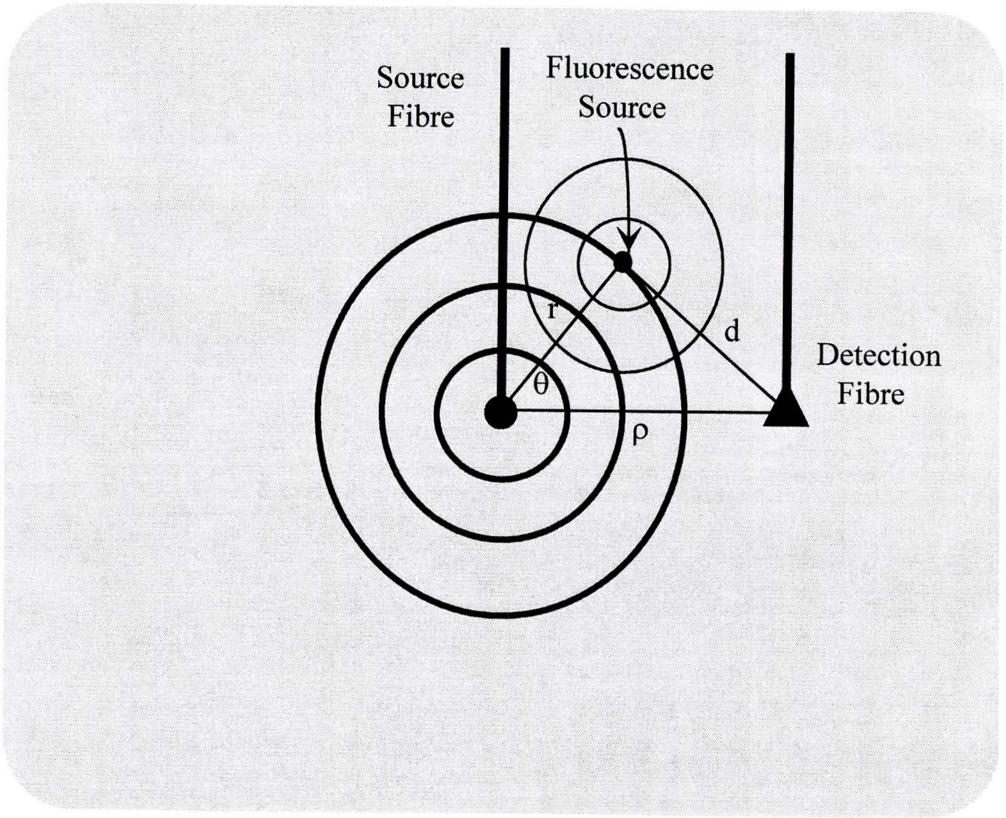

Figure 2.5.1 Representation of a isotropic point source imbedded in an infinite medium. The excitation fluence gives rise to a spherical distribution of fluorescence sources which can be detected by a fibre at a known radius, ρ.

$$d = \sqrt{\rho^2 + r^2 - 2r\rho\cos\theta}\,. \tag{53}$$

Thus, a single fluorescence point at radius r and angle θ from the source will contribute

$$F(\rho; r, \theta) = \frac{3\mu_t\gamma}{4\pi}\Phi(r)\mu_{a(drug)}(r)\frac{e^{-\mu_{eff}\sqrt{\rho^2+r^2-2r\rho\cos\theta}}}{\sqrt{\rho^2 + r^2 - 2r\rho\cos\theta}} \tag{54}$$

to the total fluorescence observed at radius ρ. The entire shell at radius r will contribute

$$F_{shell}(\rho; r) = \int_0^{2\pi}\int_0^{\pi} F(\rho; r, \theta)\sin\theta d\theta d\phi \tag{55}$$

$$= \frac{3\mu_t\gamma}{2\mu_{eff}\rho}\frac{\Phi(r)\mu_{a(drug)}(r)}{r}\left(e^{-\mu_{eff}\sqrt{\rho^2+r^2-2r\rho}} - e^{-\mu_{eff}\sqrt{\rho^2+r^2+2r\rho}}\right).$$

Finally, the fluorescence reaching the detector at radius ρ is the integral of all shells

$$F_{total}(\rho) = \int_0^{\infty} F_{shell}(\rho; r)r^2 dr \tag{56}$$

$$= \frac{3\mu_t\gamma}{2\mu_{eff}\rho}\int_0^{\infty} r^2\Phi(r)\mu_{a(drug)}(r)\left(e^{-\mu_{eff}\sqrt{\rho^2+r^2-2r\rho}} - e^{-\mu_{eff}\sqrt{\rho^2+r^2+2r\rho}}\right)dr.$$

A curve demonstrating predicted fluorescence measurements at a radius of 3.0 millimetres from the source is given in figure 2.5.2a. For the spherical model, standard initial conditions were: $\mu_{a(drug)}$= 0.02 mm^{-1}, μ_{a_o}= 0.02 mm^{-1}, μ_s'=1.00 mm^{-1} and bleach rate = 0.10 cm^2/J. Similar to the semi-infinite model, a simple exponential curve is not observed due to the photobleaching of photosensitizer giving rise to a spatially dependent drug absorption coefficient. The increase in necrosis radius with treatment is shown in figure 2.5.2b, and the corresponding necrosis radius versus observed fluorescence curve is presented in figure 2.5.2c, again with irradiation time moving from right to left.

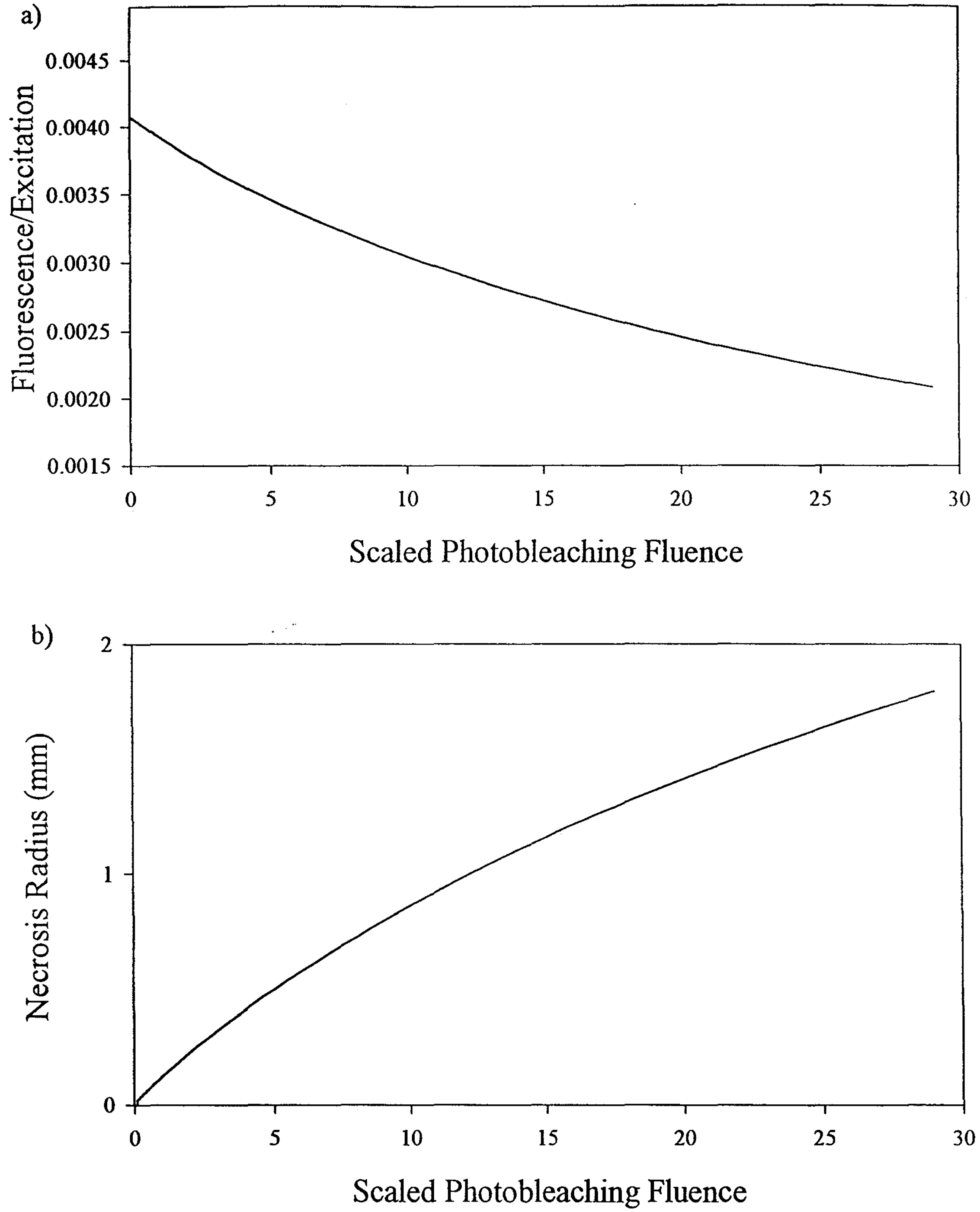

Figure 2.5.2 **a)** Fluorescence as a function of scaled photobleaching fluence for a single detection point at 3.0 mm from the source, using standard initial conditions.
b) Increase in necrosis depth as treatment progresses for a photosensitizer threshold of 0.03 mm^{-1}.

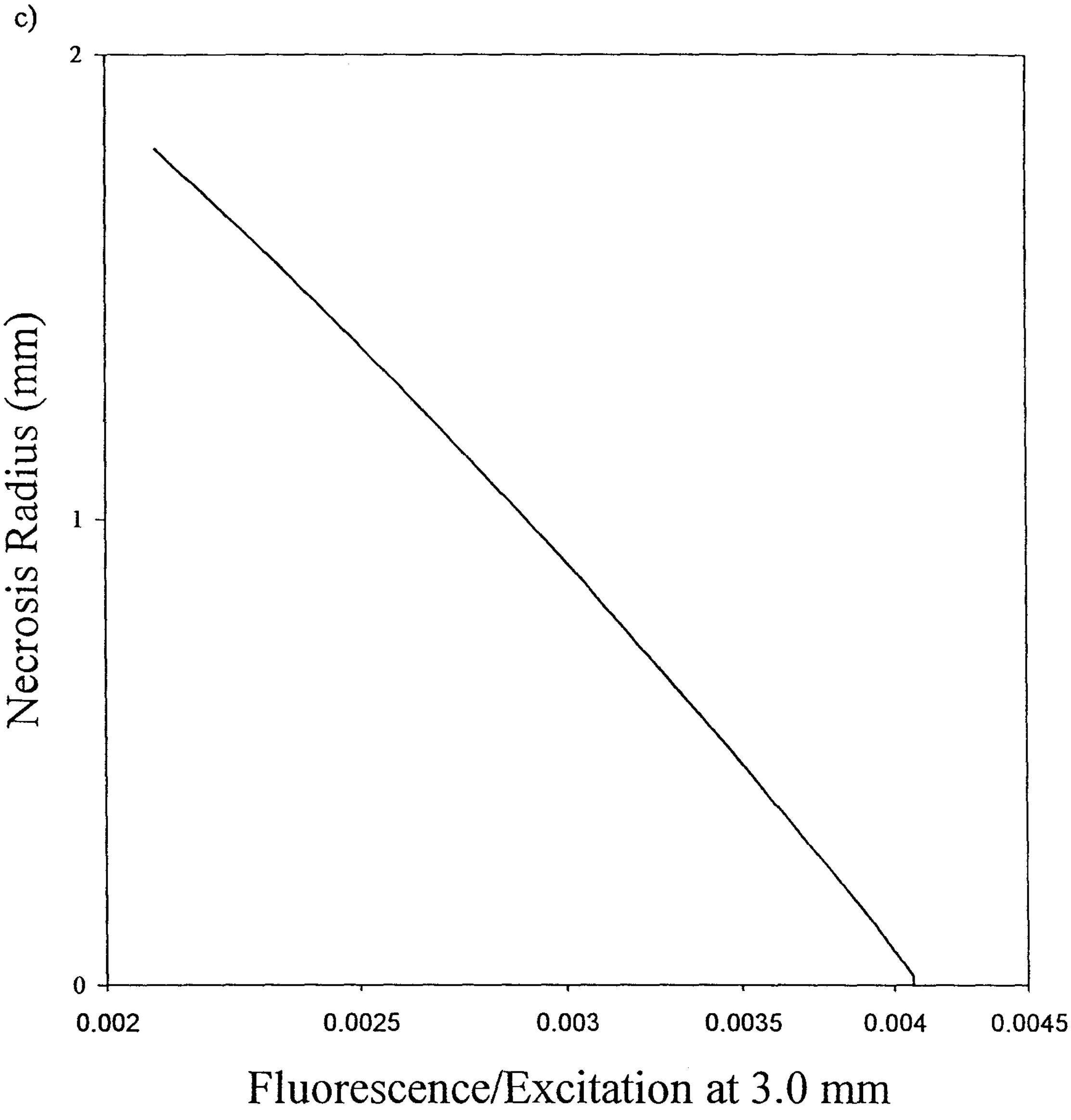

Figure 2.5.2 c) The relationship between predicted necrosis radius and fluorescence signal for a single detector located 3.0 mm from the excitation source (irradiation time moves from right to left). Standard initial condition apply.

3 MATHEMATICAL MODELLING RESULTS

In order to determine the accuracy with which predictions about necrosis depth can be made from measured fluorescence, it is necessary to investigate the sensitivity of the models to small alterations in initial treatment conditions. For each fluorescence excitation model the scattering and absorption of the tissue, the initial photosensitizer concentration and the percentage of drug that must be bleached in order for necrosis to occur are varied and the effects on the established relationships between measured parameters and necrosis depth are observed.

3.1 Broad-beam Fluorescence Excitation

First, consider changing the initial photosensitizer concentration while all other parameters are held fixed at $\mu_{a_o} = 0.01\ \mathrm{mm}^{-1}$, $\mu_s' = 1.00\ \mathrm{mm}^{-1}$ and bleach rate = 0.10 cm^2/J (figure 3.1). As expected, a higher photosensitizer concentration yields a stronger fluorescence signal (figure 3.1.1a). It is anticipated that when intrinsic absorption due to endogenous chromophores in the tissue is exceeded by absorption due to the photosensitizer, "self-shielding" by the drug will become significant (Patterson *et al* 1990 and Brown *et al* 1986). This effect is responsible for limiting the extent of tissue damage at higher drug concentration (figure 3.1.1b), as discussed by Wilson (1989). Figure 3.1.1c illustrates the relationship between necrosis depth and fluorescence emission and the

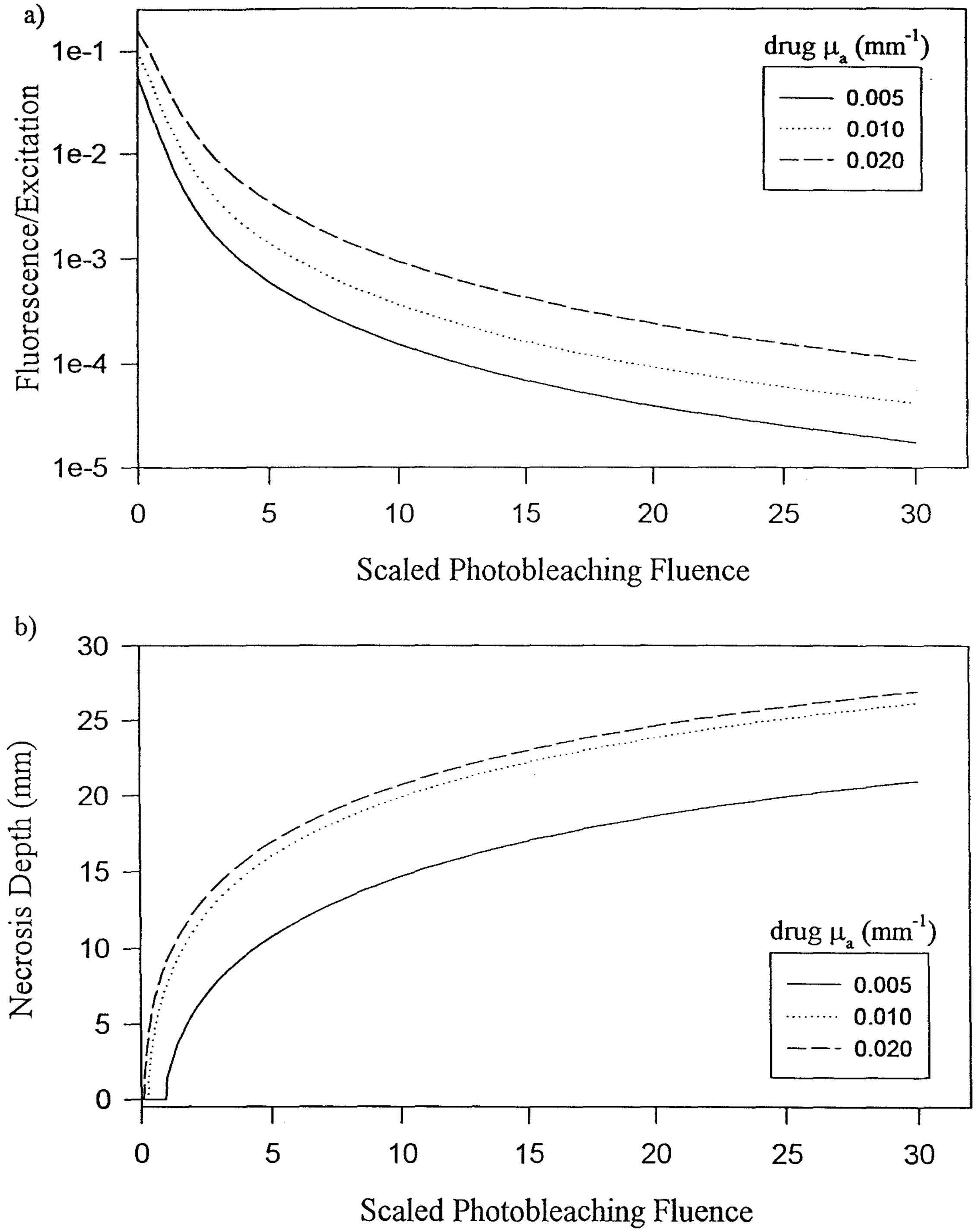

Figure 3.1.1 Other initial conditions used were standard.

- **a)** Observed fluorescence versus scaled photobleaching fluence for three initial drug absorption coefficients.
- **b)** Depth of necrosis as a function of scaled photobleaching fluence for varied initial drug absorption coefficient.

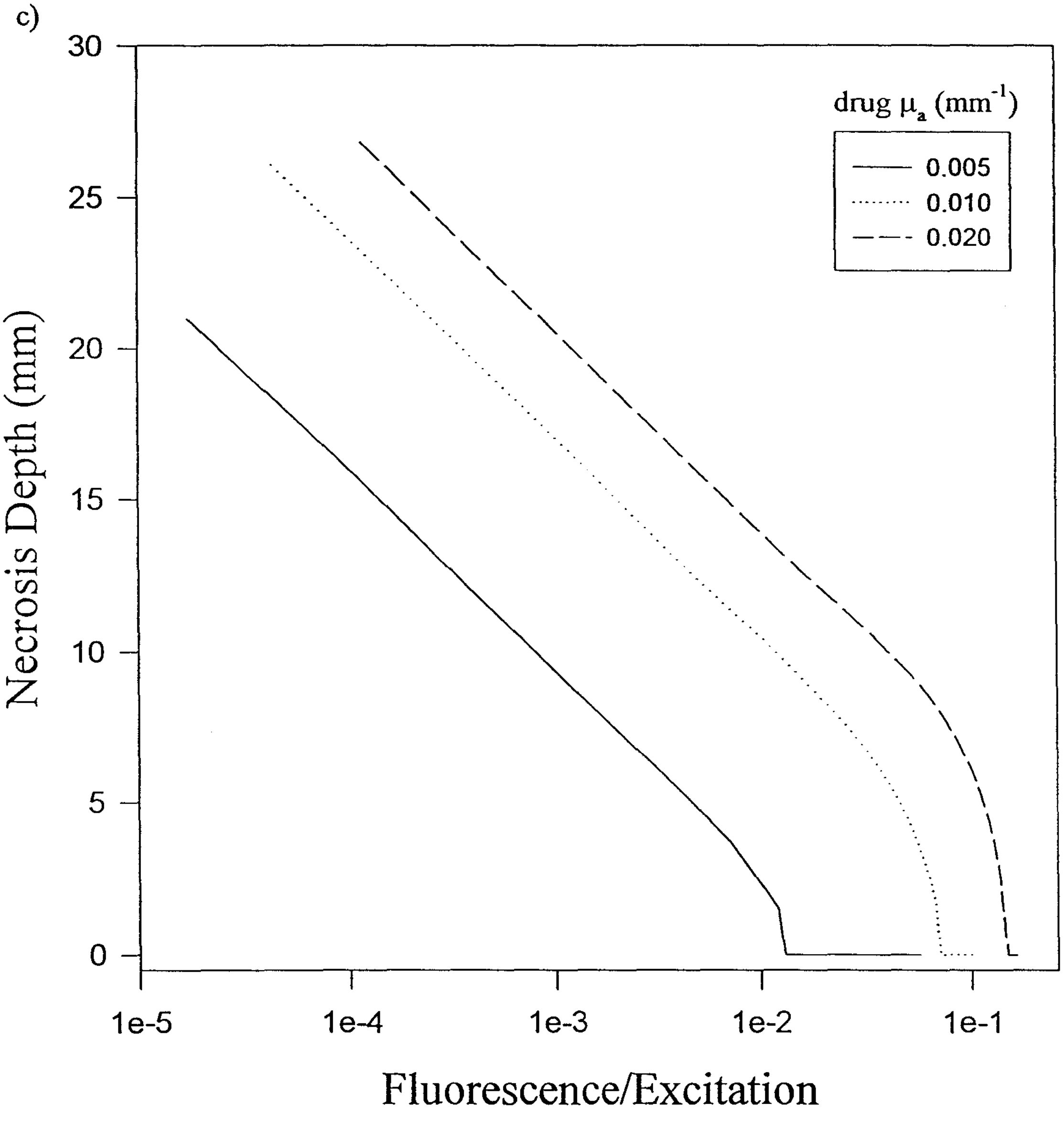

Figure 3.1.1 Other initial conditions used were standard.

c) Relationship between necrosis depth and fluorescence signal for varied initial photosensitizer absorption coefficient.

large differences resulting from small changes in initial photosensitizer concentration. Shortly after tumour necrosis commences, the necrosis depth proceeds linearly with respect to the logarithm of fluorescence, with all three curves having the same slope. The higher initial drug concentration yields a stronger fluorescence signal and causes deeper necrosis over the given time interval.

The second treatment parameter that was altered is the endogenous absorption of the tissue. Initially, before the photosensitizer near the surface has bleached away, observed fluorescence signals are higher for low μ_{a_o} due to enhanced light (both excitation and fluorescence) penetration (figure 3.1.2a). This has two effects: faster bleaching and a corresponding increase in the necrosis depth. As a result, the decrease in observed fluorescence and the increase in depth of necrosis do not progress as quickly as with low tissue absorption, illustrated by figures 3.1.2a and 3.1.2b. Even though the initial photosensitizer concentration was held fixed, the effects become more substantial later in the treatment as the divergent curves in figure 3.1.2c indicate.

Changes in the reduced scattering coefficient of the tissue produce similar changes in fluorescence emission (figure 3.1.3a) and necrosis depth (figure 3.1.3b) since higher scattering prevents deeper light penetration. Although the effect is subtle, the higher scattering induces necrosis at the surface earliest due to the higher bleaching fluence at shallow depths. The divergent relationship in figure 3.1.3c is similar to that observed for μ_{a_o} (figure 3.1.2c).

Finally, the effect of changing the bleach rate of the photosensitizer was investigated. Although a higher bleaching rate causes a much more rapid decline in fluorescence signal (figure 3.1.4a) and a corresponding increase in necrosis depth with

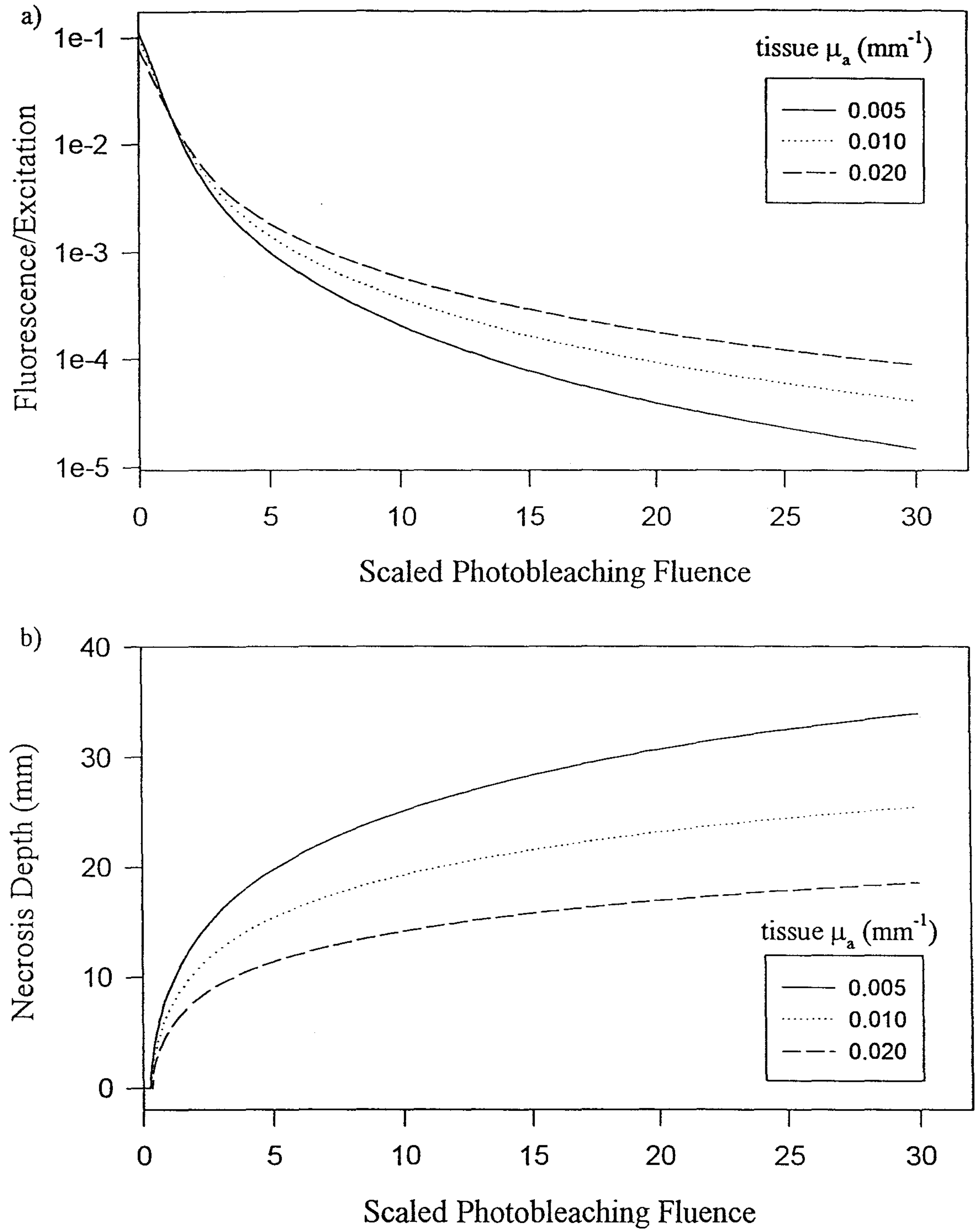

Figure 3.1.2 Other initial conditions used were standard.

- **a)** Observed fluorescence versus scaled photobleaching fluence for three endogenous tissue absorptions.
- **b)** Depth of necrosis as a function of scaled photobleaching fluence for varied endogenous tissue absorption.

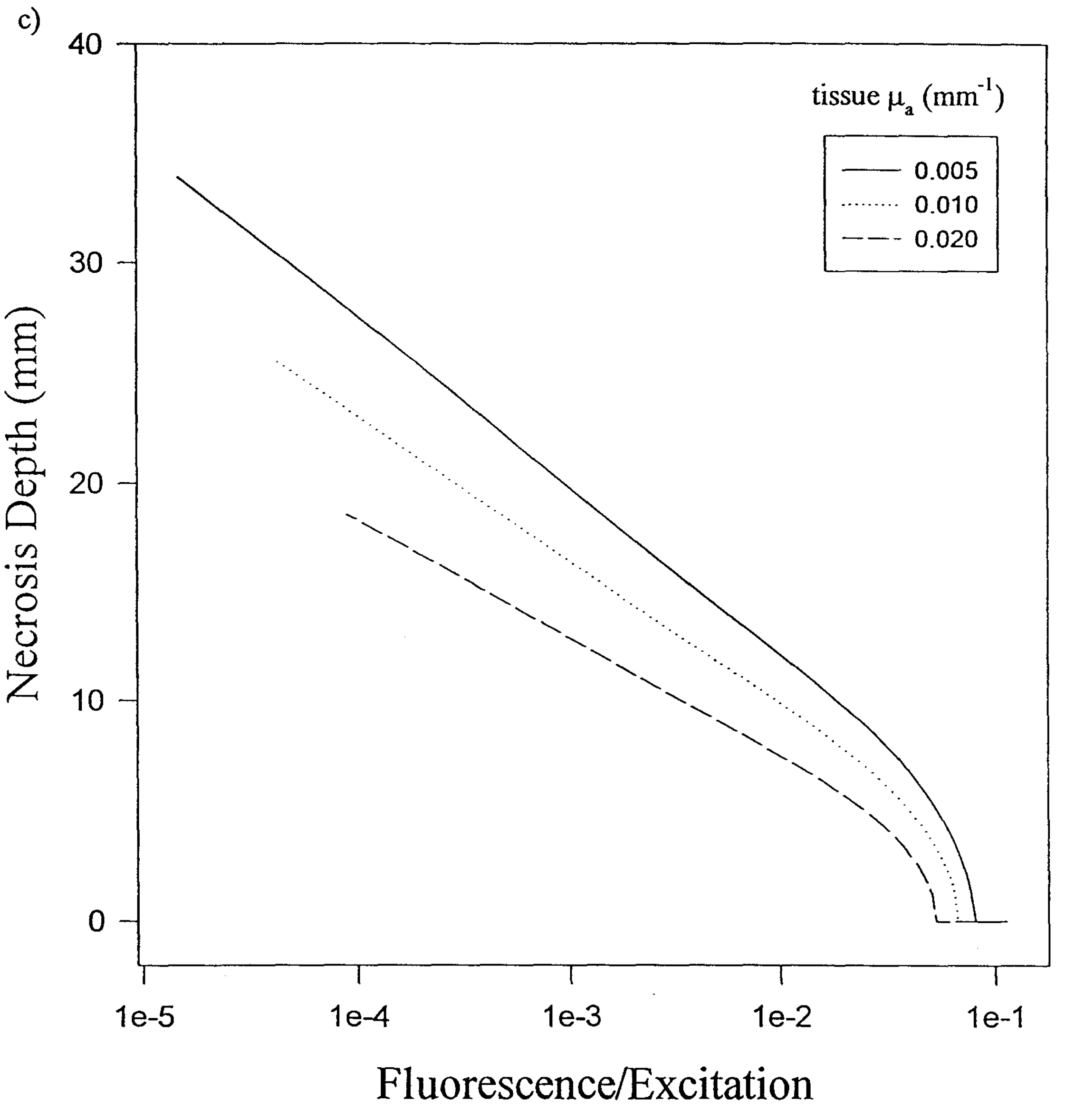

Figure 3.1.2 Other initial conditions used were standard.

c) Relationship between necrosis depth and fluorescence signal for varied endogenous tissue absorption.

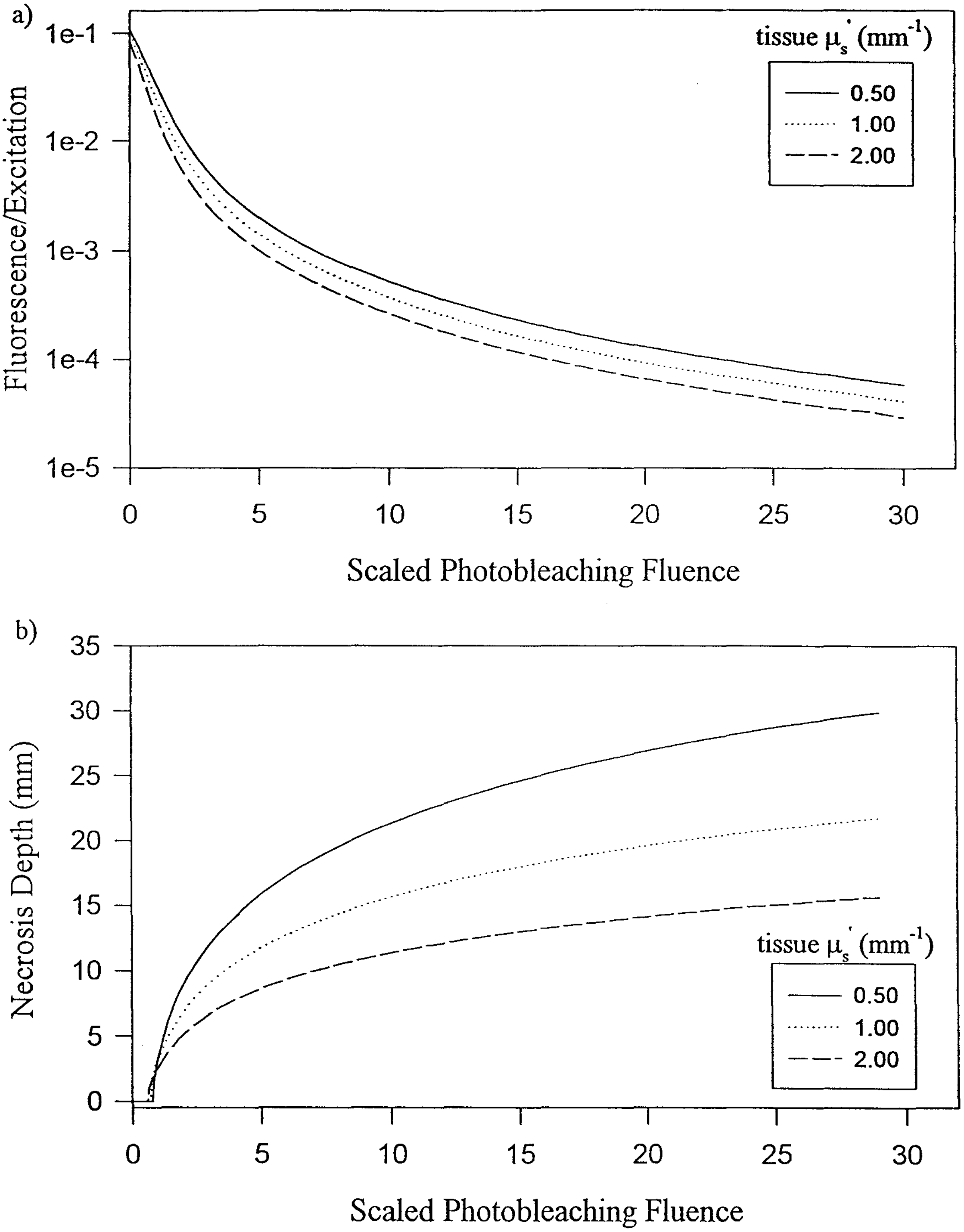

Figure 3.1.3 Other initial conditions used were standard.

a) Observed fluorescence versus scaled photobleaching fluence for three tissue scattering coefficients.

b) Depth of necrosis as a function of scaled photobleaching fluence for varied tissue scattering coefficient.

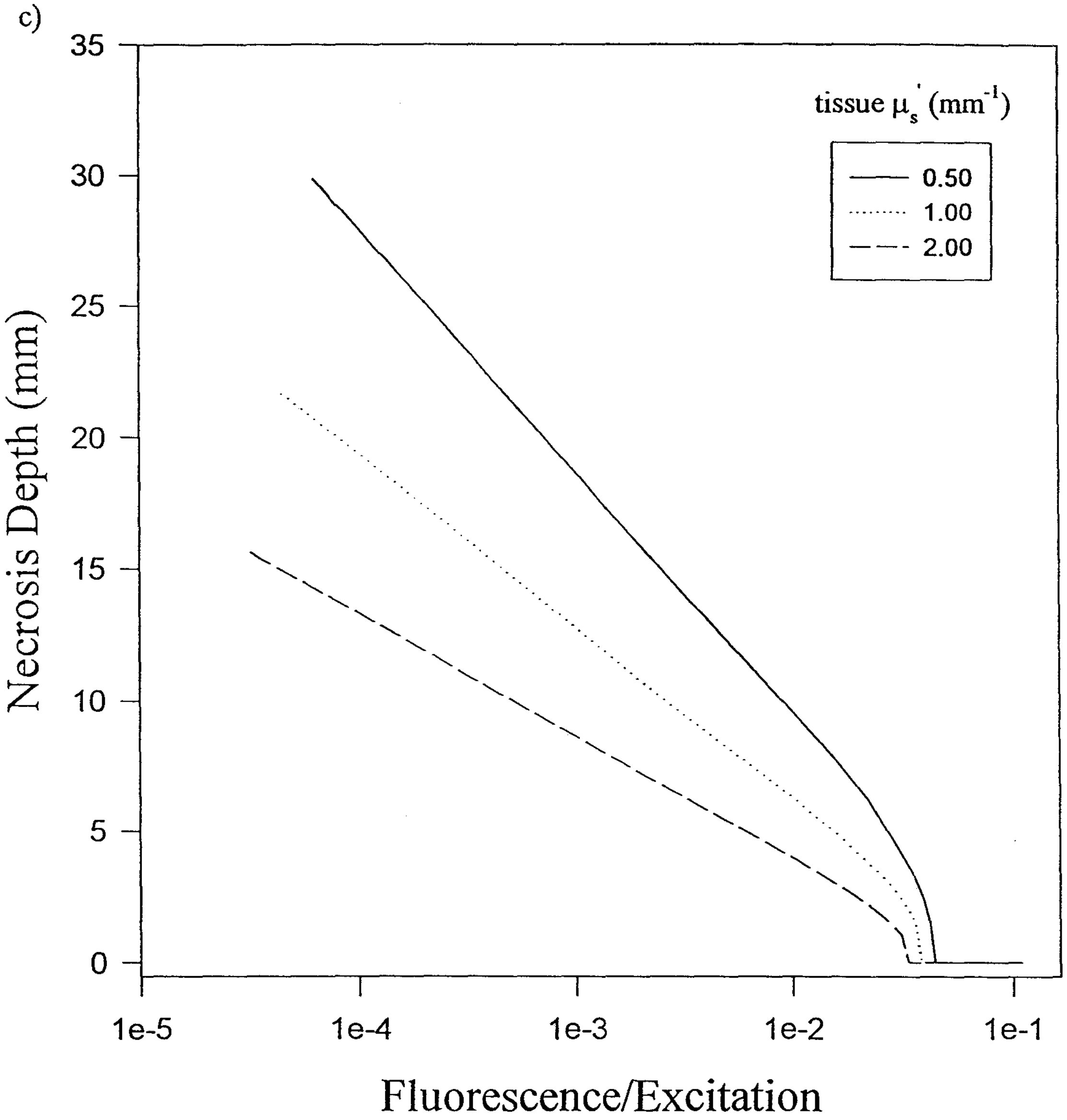

Figure 3.1.3 Other initial conditions used were standard.

c) Relationship between necrosis depth and fluorescence signal for varied tissue scattering coefficient.

respect to scaled bleaching fluence (figure 3.1.4b), the relationship between necrosis depth and fluorescence signal is independent of bleaching rate, as figure 3.1.4c reveals.

From these results it is apparent that small changes in the initial treatment parameters can cause large variation in the necrosis depth versus fluorescence relationship. Varying the drug concentration shifted the curve towards higher fluorescence and deeper necrosis, while altering the optical properties of the tissue caused the curves to diverge. In order to be useful in a clinical situation, the extent of tumour damage must be closely monitored during treatment. Unfortunately, it is difficult to accurately determine these parameters using current measurement techniques, thereby limiting the usefulness of this approach. On a positive note, fluence rate and bleaching kinetics (assuming first order) are not significant if fluorescence is used to predict the effect of treatment.

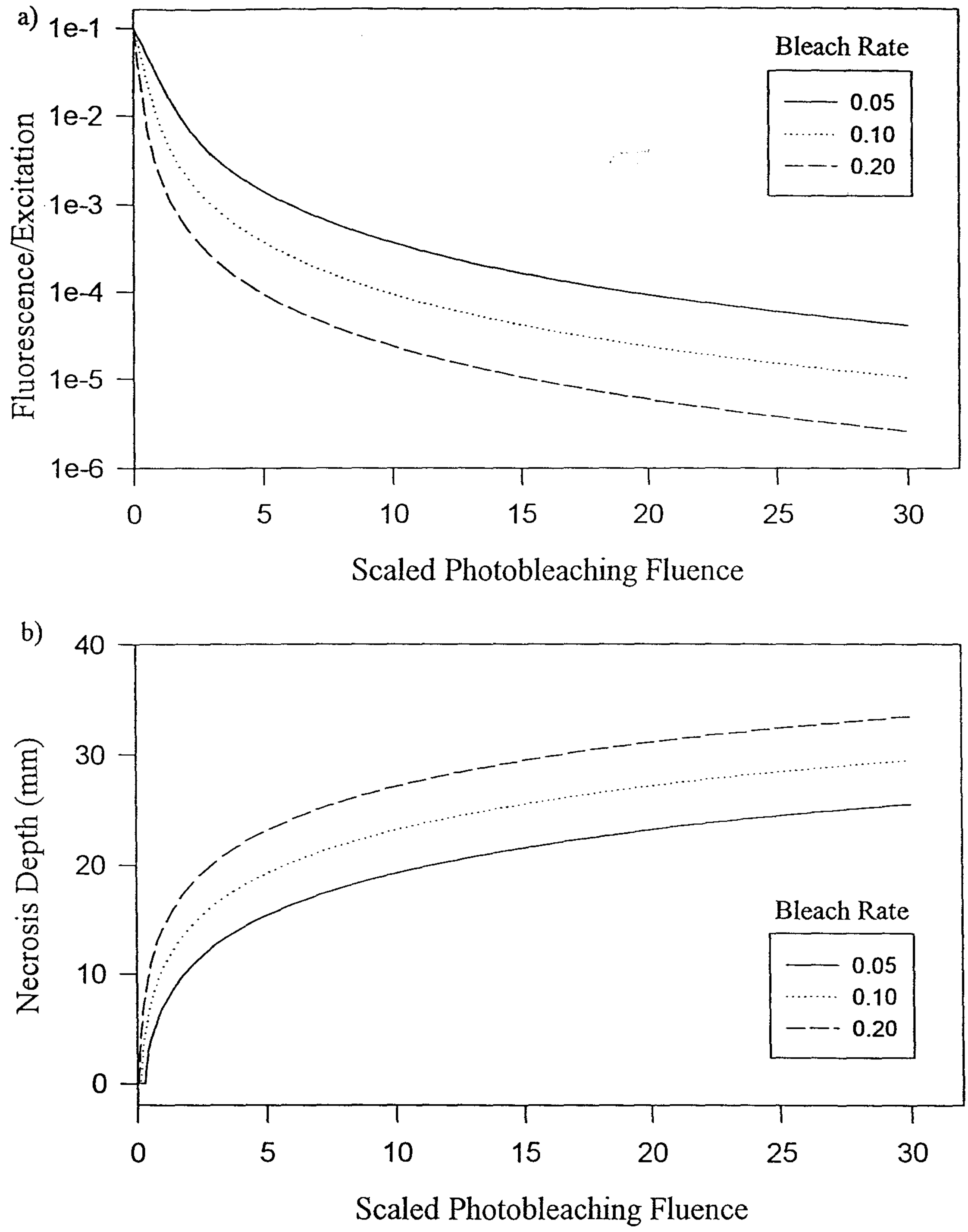

Figure 3.1.4 Other initial conditions used were standard.

a) Observed fluorescence versus scaled photobleaching fluence for three bleach rates.

b) Depth of necrosis as a function of scaled photobleaching fluence for varied bleach rate.

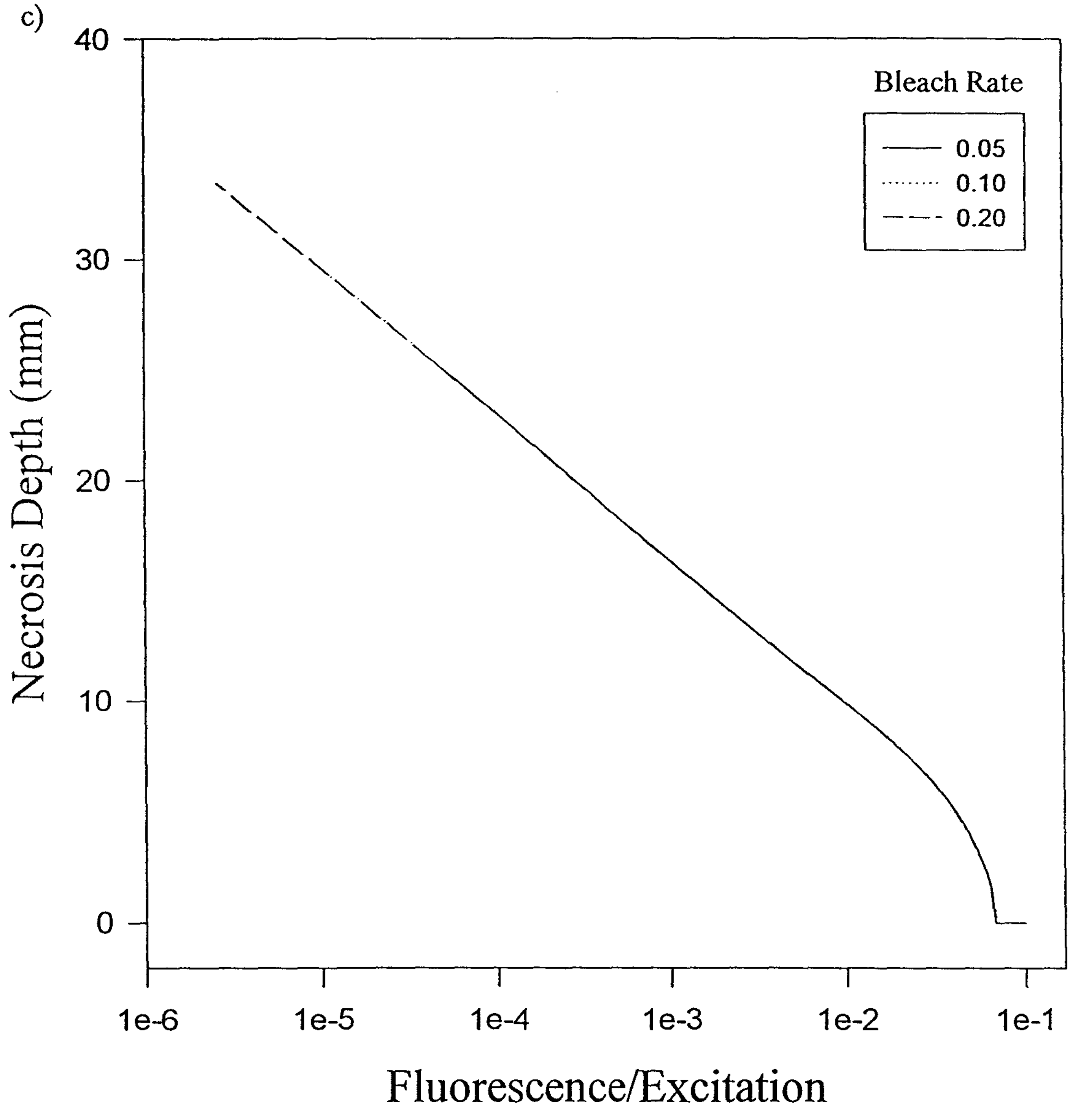

Figure 3.1.4 Other initial conditions used were standard.

c) Relationship between necrosis depth and fluorescence signal for varied bleach rate.

3.2 Pencil Beam Excitation, Highly Scattering Medium

For the scatter dominated model, the most important relationship is that between virtual plane depth and necrosis depth. By changing the percentage of photosensitizer that must be bleached in order for necrosis to occur, the shape of the curve can be greatly affected, as seen in figure 3.2.1a. For a threshold of 50 percent, very little information can be obtained from the initial part of the curve since the necrosis depth is changing very quickly for small changes in virtual plane depth. At the other extreme, a 99.5 percent threshold requires the virtual plane depth to penetrate much deeper before necrosis begins. The slow increase in necrosis depth makes it more feasible to track treatment progress based on measured changes in virtual plane depth. In all three cases, a useful relationship eventually results since increases in necrosis depth and virtual plane depth are proportional.

Next, variations in optical properties were made. As a standard, $\mu_s' = 1.50$ mm^{-1}, tissue $\mu_a = 0.04$ mm^{-1} and drug $\mu_a = 0.02$ mm^{-1} to ensure that the condition μ_s'+tissue $\mu_a \gg$drug μ_a is realistic. Figure 3.2.1b indicates that changing the photosensitizer concentration does not affect the relationship between necrosis depth and virtual plane depth if the necrosis threshold is held fixed. From figure 3.2.1a, it can be concluded that changing the photosensitizer absorption coefficient while keeping the absolute value of the necrosis threshold fixed would result in dissimilar curves. Similarly, figures 3.2.1c and 3.2.1d show very little difference when tissue optics are altered, especially as treatment progresses.

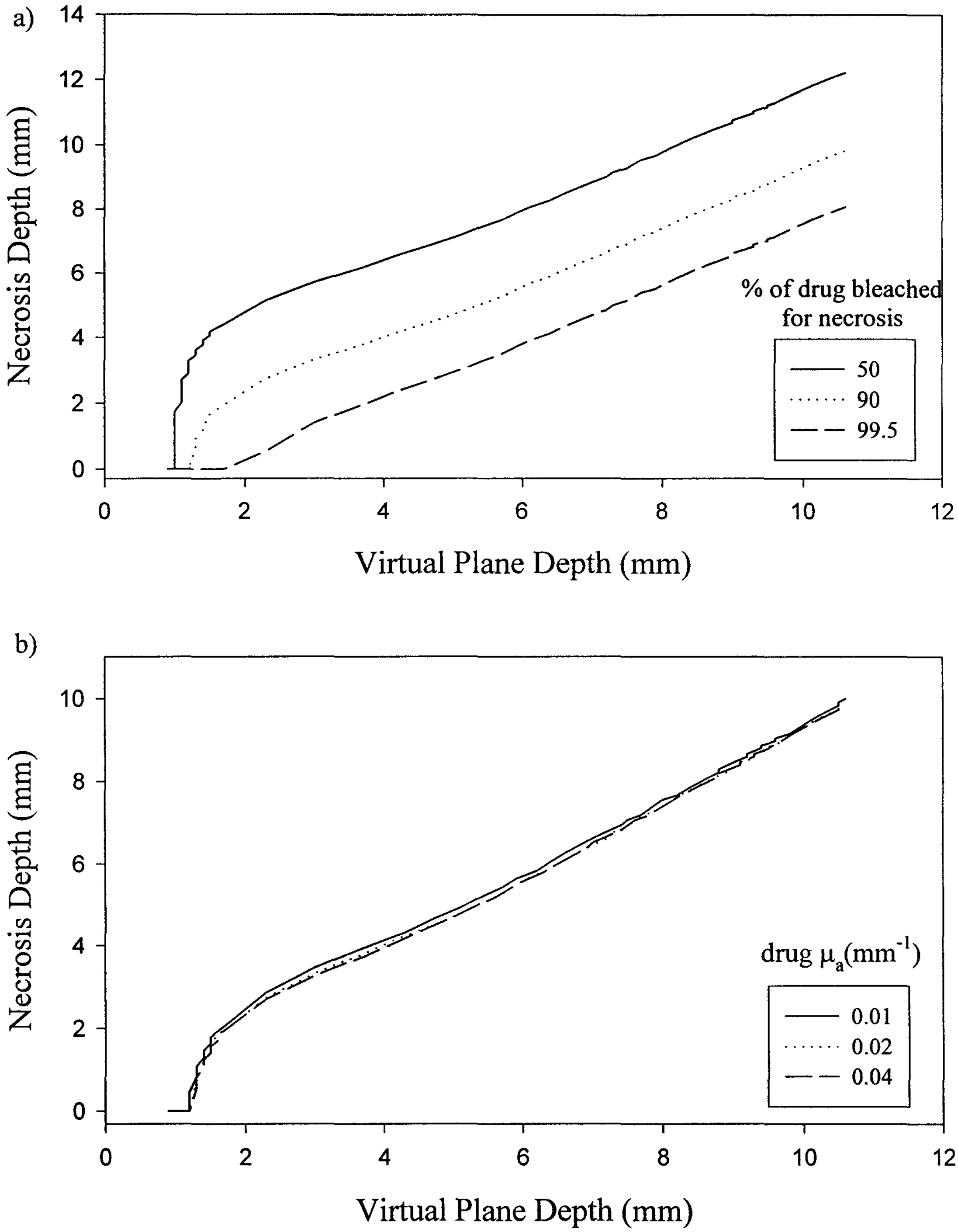

Figure 3.2.1 Other initial conditions used were standard.

a) Relationship between necrosis depth and virtual plane depth for varied necrosis threshold (percentage of initial photosensitizer).

b) Relationship between necrosis depth and virtual plane depth for varied initial $\mu_{a(drug)}$ (necrosis threshold held fixed at 90 percent).

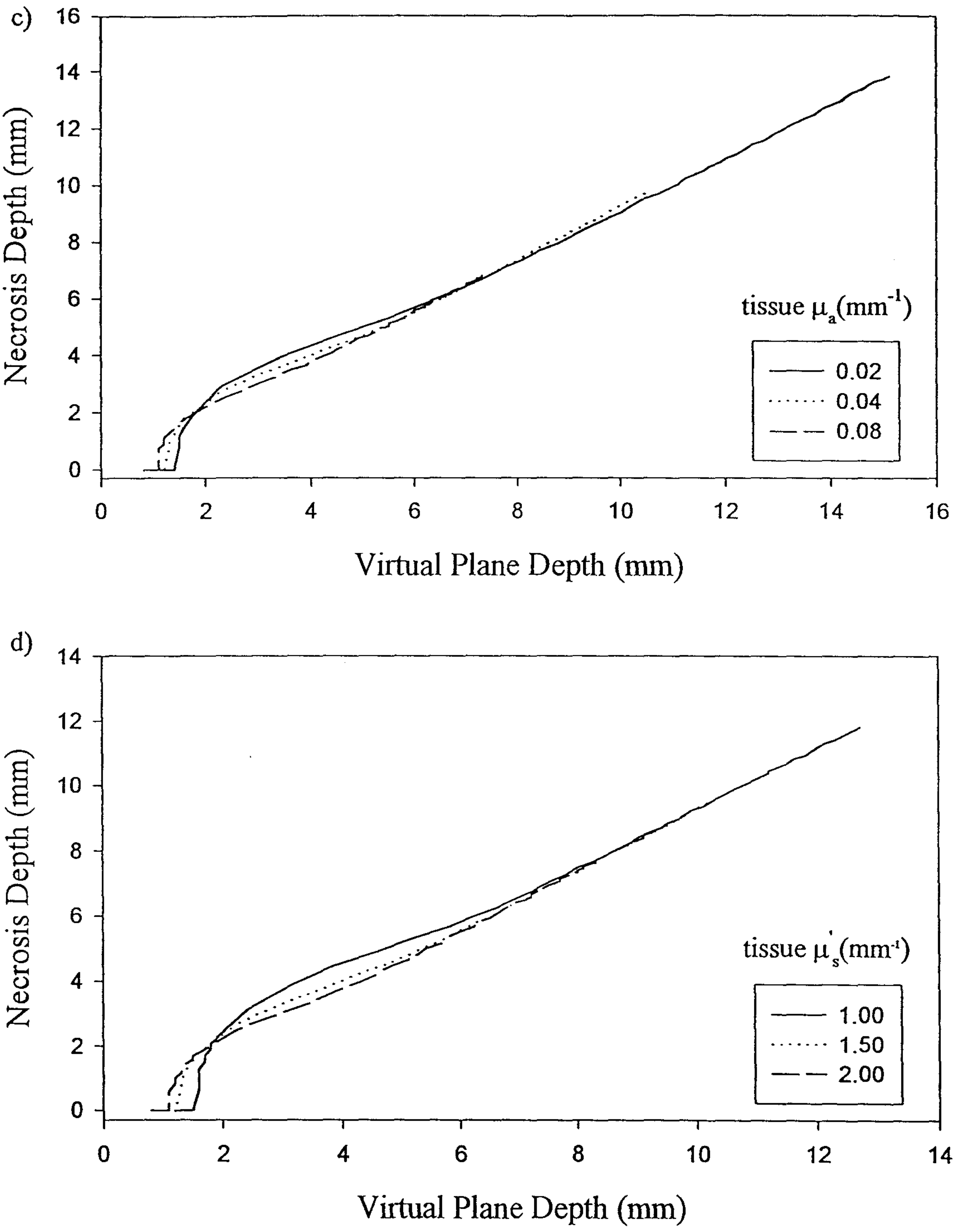

Figure 3.2.1 Other initial conditions used were standard.

c) Relationship between necrosis depth and virtual plane depth for varied endogenous tissue absorption coefficient.

d) Relationship between necrosis depth and virtual plane depth for varied tissue scattering coefficient.

The relative insensitivity of these relationships to altered initial conditions indicates that the potential exists to make accurate calculations of necrosis depth without highly accurate knowledge of optical properties if virtual plane depth is known. Unfortunately, the current technique employed for calculating the depth of the virtual plane requires that the optical properties be known *a priori*, limiting this approach until a new method is found for determination of the virtual plane depth. Alternatively, if the optical properties were measured prior to treatment, the discussed technique could potentially allow for monitoring of necrosis depth based on measured fluorescence. The use of spatially resolved fluorescence measurements has made it possible to indirectly track the changing spatial distribution of photosensitizer using a single metric, the virtual plane depth, thereby greatly simplifying the vast amount of information obtained. Furthermore, the virtual plane depth has been shown to be related to necrosis depth, providing a key link between observed fluorescence and photodynamic dose.

3.3 Pencil Beam Excitation, Highly Absorbing Medium

The effect of changing initial parameters on the relationship between virtual source depth and necrosis depth was investigated. To begin with, figure 3.3.1a again shows that increasing the percentage of photosensitizer that must be bleached for necrosis to occur provides a more useful curve as far as predicting necrosis depth is concerned.

Figures 3.3.1b-d investigate varied optical properties. Figure 3.3.1b demonstrates that the extent of tissue damage can be found from the virtual source depth without accurate knowledge of the initial drug absorption coefficient. Again, the necrosis

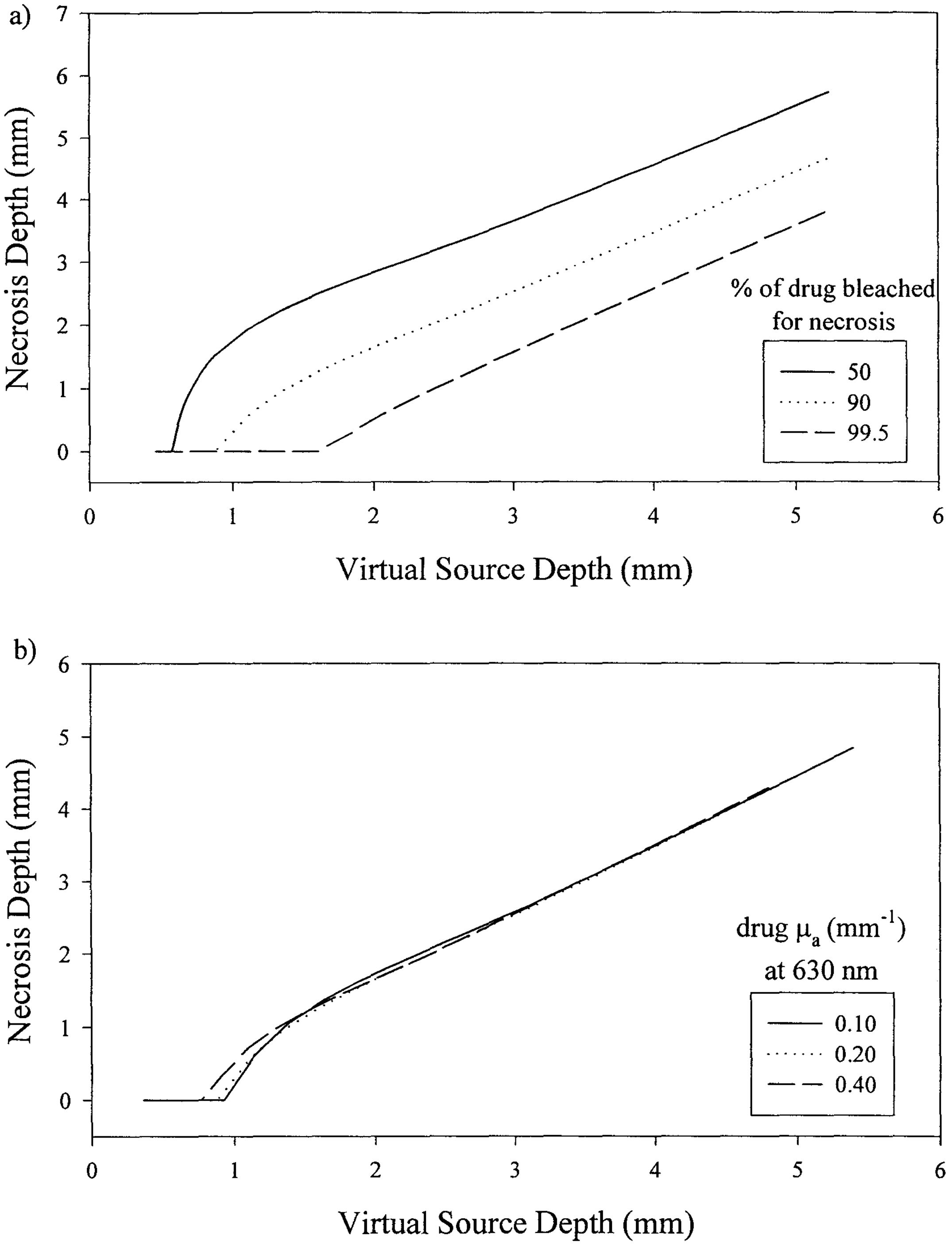

Figure 3.3.1 Other initial conditions used were standard.

a) Relationship between necrosis depth and virtual source depth for varied necrosis threshold.

b) Relationship between necrosis depth and virtual source depth for varied initial photosensitizer concentration.

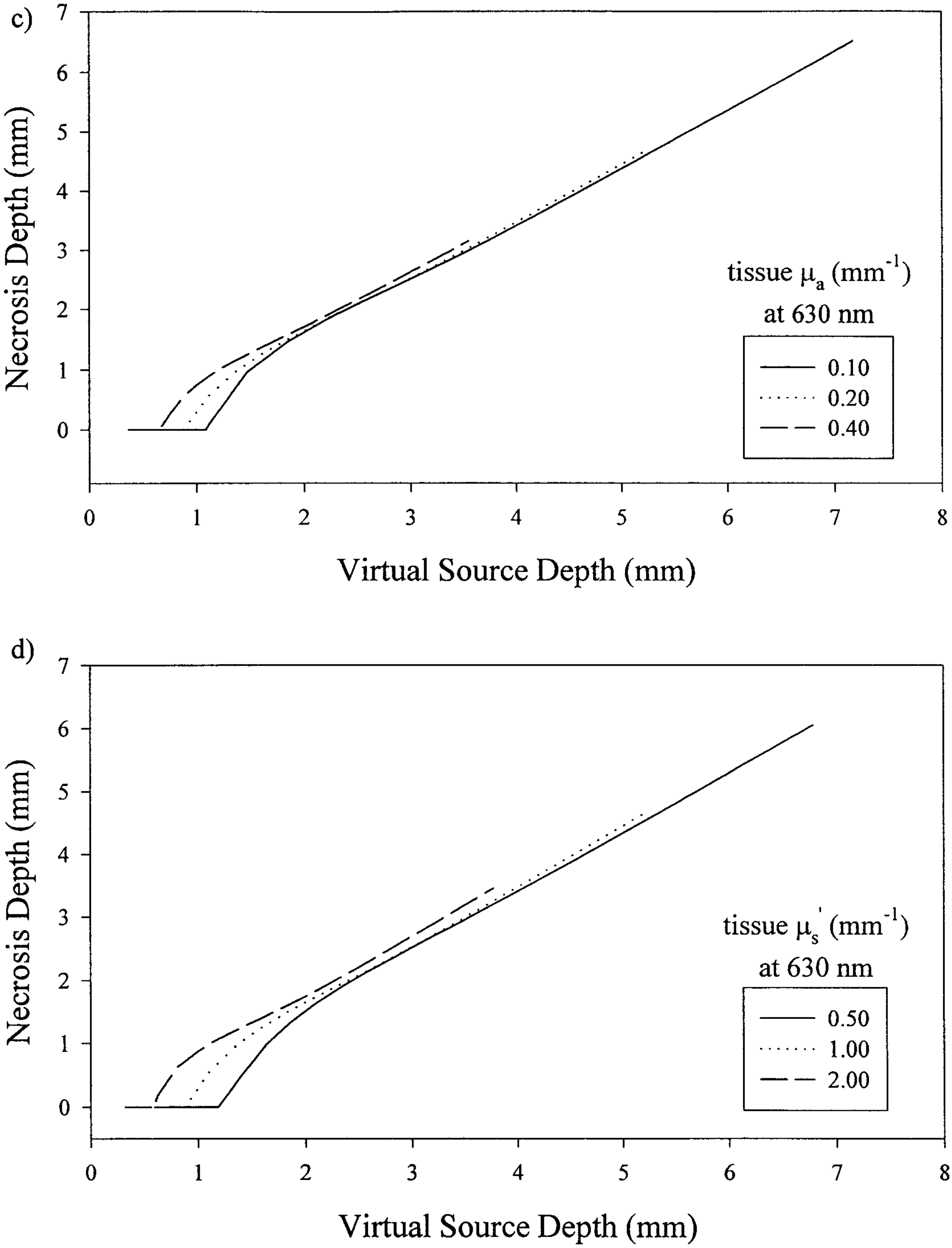

Figure 3.3.1 Other initial conditions used were standard.

c) Relationship between necrosis depth and virtual plane depth for varied endogenous tissue absorption coefficient.

d) Relationship between necrosis depth and virtual plane depth for varied tissue scattering coefficient.

threshold is a percentage of initial drug absorption coefficient (90 percent must be bleached). Similarly, figure 3.3.1c illustrates that the scattering coefficient is also not significant. Finally, changes in the absorption coefficient of the medium have little effect on the plot of necrosis depth versus virtual source depth shown in figure 3.3.1d. Note that the virtual source position does not depend on the tissue optical properties at the emission wavelength, so altering these would also have no effect. These results suggest that if the virtual source depth could be experimentally determined during a treatment, necrosis depth could be predicted without exact knowledge of the initial conditions.

Adapting the technique of spatial diffuse reflectometry described by Farrell *et al* (1992), the depth of this virtual source can be calculated based on the fluorescence observed from several fibres at known radii by solving equation 21. At the fluorescence wavelength, absorption by photosensitizers is generally very low. As a result, only the effective attenuation coefficient of the tissue at the fluorescence wavelength is unknown, and this parameter can be fitted simultaneously when determining the single fluorescence source depth.

Thus, by measuring fluorescence emission at several distances from the excitation fibre and calculating the depth of the virtual fluorescence source with respect to time, necrosis depth can be followed with little knowledge of other treatment parameters, unlike the case involving the virtual plane. This would be extremely useful in clinical situations where tissue optics, drug concentrations and fluence rates are difficult to determine accurately. It is important to realize, however, that the model requires knowledge of optical properties for determination of necrosis depth and predicts only the nature of the relationship between it and virtual source depth. The actual relationship between necrosis depth and virtual source depth would have to be determined experimentally.

3.4 Infinite Medium, Isotropic Point Source

The sensitivity of the relationship between necrosis radius and fluorescence signal to small changes in initial conditions was investigated for the spherical model. Since the fluorescence is decreasing over the course of the treatment, in these curves time progresses from right to left. To begin with, increasing the percentage of photosensitizer bleaching required for necrosis caused the curve to straighten, and decreased the necrosis depth for the given treatment period, illustrated in figure 3.4.1a. Unlike the previous models, necrosis depth can be determined early in the treatment for a low threshold without difficulty.

Figures 3.4.1b-d demonstrate the high dependence on initial drug absorption, tissue absorption and tissue scattering, respectively. Increasing the photosensitizer concentration (figure 3.4.1b) caused a decrease in the extent of necrosis, and a decrease in the fluorescence observed at 3.0 mm, due to self-shielding. An absolute necrosis threshold of 0.015 mm^{-1} was used in each case. Figure 3.4.1c shows the large decrease in fluorescence and slight decrease in necrosis radius resulting from an increase of the endogenous tissue absorption. Absorption by the tissue is considered equal for excitation and fluorescence light. Finally, an increase in scattering coefficient (figure 3.4.1d) raises the excitation fluence near the source resulting in an increase in observed fluorescence

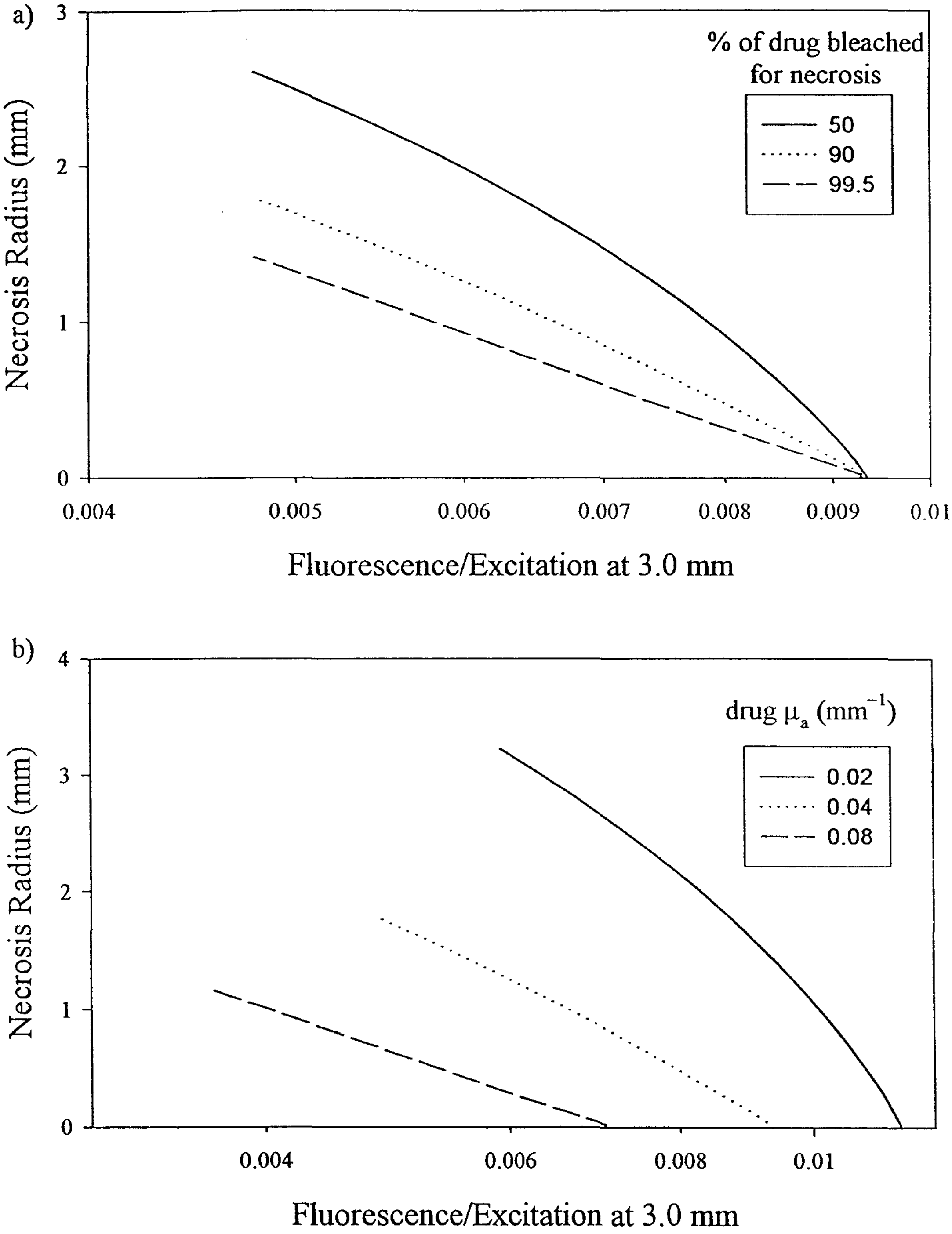

Figure 3.4.1 Other initial conditions used were standard.

a) Relationship between necrosis radius and fluorescence signal at 3.0 mm for varied necrosis threshold.

b) Relationship between necrosis radius and fluorescence signal at 3.0 mm for varied initial photosensitizer concentration.

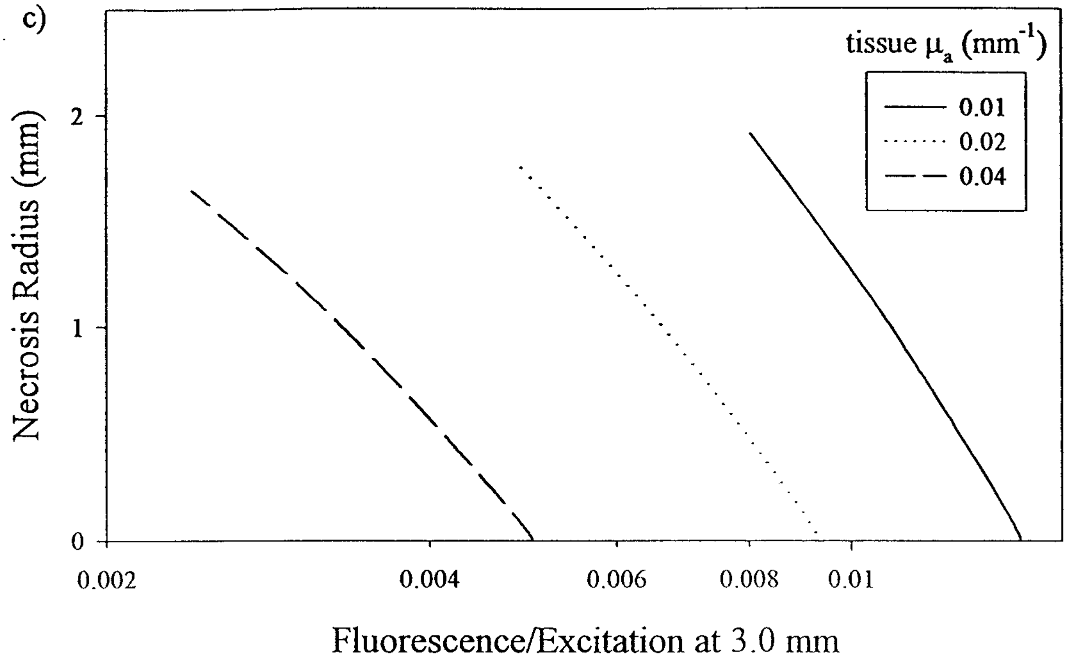

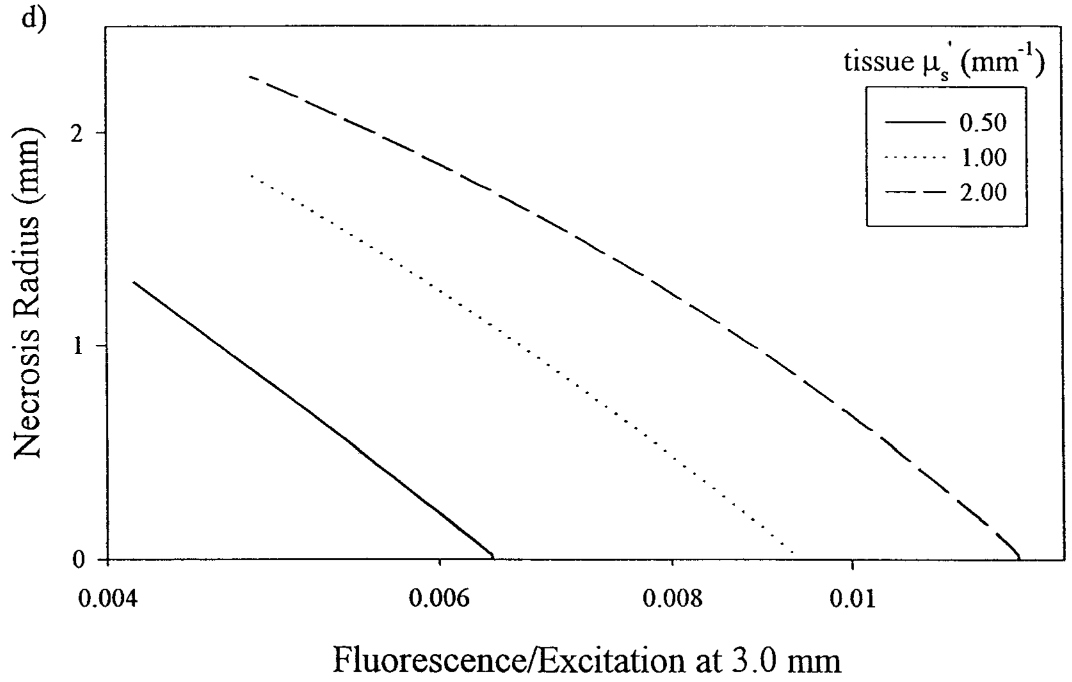

Figure 3.4.1 Other initial conditions used were standard.

c) Relationship between necrosis radius and fluorescence signal at 3.0 mm for varied endogenous tissue absorption coefficient.

d) Relationship between necrosis radius and fluorescence signal at 3.0 mm for varied tissue scattering coefficient.

and necrosis depth.

Unfortunately, without accurate knowledge of these parameters prior to treatment, the model would apparently be unable to make any useful predictions about necrosis depth. To improve this model, it may be possible to again look at the variation between spatially resolved measurements that could be performed by inserting several optical fibres at known radii from the source. These measurements could lead to the determination of a virtual shell of fluorescence which may be less sensitive to changes in initial conditions.

4 EXPERIMENTAL VERIFICATION

Photobleaching and fluorescence excitation experiments are necessary to explore the applicability of the mathematical modelling to an actual PDT treatment. Since initial studies require accurate characterization of initial conditions such as photosensitizer concentration and optical properties, tissue simulating optical phantoms were developed. Using the techniques described below, these phantoms were prepared with target initial characteristics and, once completed, verification was performed. Several phantoms were created having the same "standard" initial conditions to test reproducibility, while other phantoms had optical properties and photosensitizer concentration altered independently in order to observe the effect on measured fluorescence. Details of index of refraction measurements and bleach rate determination are also given, as is an analysis of phantom uniformity.

4.1 Phantom Preparation

Considering the need for a phantom with spatially varying optical properties, a curable liquid was required to allow for mixing of components prior to solidification. Although difficult to work with due to its viscous, sticky nature, a clear styrene and polyester casting resin (Lewiscraft) was chosen as it is relatively inert optically, mixes easily with the desired additives, and cures quickly following the addition of the required catalyst.

Endogenous absorption by the phantom was attained through the addition of a black dye produced specifically to colour the resin for crafts (Lewiscraft). Conveniently, it has uniform absorption in the visible spectrum and does not fluoresce. The absorption properties for various dye concentrations were determined in a spectrophotometer using methacrylate semi-micro cuvettes (polystyrene cannot be used because it reacts with the resin causing clouding of the cuvette walls).

Metal oxide powders were used as scatterers. A small particle size is used (less than five microns in diameter) to give a more uniform distribution, and to prevent settling during the curing period. Originally, aluminum dioxide was used until it was determined to fluoresce at 690 nm. Since photosensitizers generally fluoresce in the red region of the visible spectrum, this complication was unwelcome, leading to the adoption of titanium oxide (Aldrich Chemicals) which has very low absorption and fluorescence.

Given its photobleaching behaviour, solubility in the resin and clinical applicability, Photofrin was the photosensitizer employed. Absorption properties for various concentrations were determined using the spectrophotometer at the fluorescence excitation, bleaching, and fluorescence emission wavelengths (515 nm, 630 nm and 690 nm, respectively).

The preparation of a phantom is a tedious process that must be done carefully and precisely in a well-ventilated area. To begin with, the resin should be poured into a disposable, non-reactive polyethylene container with the desired geometry, preferably with a lid. A cylindrical container with a height of 4.5 centimetres and diameter of 9 centimetres (200 millilitres) was sufficient to avoid boundary problems for the scatter dominated phantoms produced, thereby providing an adequate "infinite" medium for an incident pencil beam of light. Since the resin is virtually impossible to transfer from one container to another, accurate volumetric measurements are difficult. The simplest approach is to fill the container to a known level (210 millilitres at the top) and then make fine adjustments by removing small amounts with a large syringe. Initially, 190 millilitres of resin are required to give a final volume of 200 millilitres after all components have been added.

Once the majority of bubbles have escaped from the resin the black dye can be added. Premature addition will lead to attraction of the dye to the bubbles making a uniform distribution difficult to achieve. For a background absorption of 0.02 mm^{-1} at 630 nm, 2.7 microlitres of dye were added using a micropipette and then folded into the resin with a metal spatula to avoid it binding to the container walls. At this point, a small amount of resin can be removed with a syringe and transferred to a cuvette if measurement of background absorption is desired.

Next, the photosensitizer is added. To allow for thorough mixing with the resin, the stock solution consists of Photofrin dissolved in spectro-grade methanol with a concentration of 2.5 milligrams/millilitre. Addition of 2.0 millilitres (equivalent to 25 milligrams of Photofrin for each litre of resin) will give a photosensitizer absorption coefficient of approximately 0.04 mm^{-1} at 630 nm. Once again, a spectrophotometer may be utilized to measure absorption properties in a cuvette of resin.

Titanium oxide powder tends to aggregate if added directly to the resin so it is first mixed with methanol to form a paste. Scattering properties are dependent on the number of scattering particles, requiring the mass of titanium oxide to be determined for the desired particle size. Using a powder with a maximum particle diameter of five microns (Aldrich Chemical Company, #22,422-7) a scattering coefficient of 1.0 mm^{-1} was obtained from 0.95 grams of titanium oxide mixed in a total of 10 millilitres of methanol. For best results, a small mixing container should be used, adding the methanol in several stages to wash the majority of the titanium oxide into the resin.

Finally, once thorough mixing has been accomplished, 12 drops of catalyst should be added. An increase in catalyst will cause the phantom to cure more rapidly, however subsequent elevated heating resulting from the exothermic curing process could chemically alter the photosensitizer.

After approximately 24 hours the phantoms will have set and must be removed from their containers to allow for final curing. Once they are no longer tacky the phantoms are easily machined on a lathe to give a flat surface. Sanding is done with wet sandpaper, increasing the grit number until desired smoothness is attained.

4.2 Phantom Properties

4.2.1 Optical Property Measurement

Non-invasive measurements of optical properties for the finished phantoms were determined using the concept of steady-state, spatially resolved diffuse reflectance (Farrell *et al* 1992). Multiply-scattered light from a broad-band pencil beam source normal to the phantom surface is collected at several known radii using an optical fibre based probe. Using spectrograph optics the light from each collection fibre is dispersed across a separate region of a CCD, giving spectrally resolved results. For a desired wavelength these radially resolved measurements are input into either a trained neural network or non-linear curve fitting routine (both diffusion theory based) which will return optical properties that have been shown to agree within two percent with values obtained using other techniques (Farrell *et al* 1994). Using this approach initial scattering and absorption properties can be derived at both bleaching and fluorescence wavelengths simultaneously without significant bleaching of the phantom.

4.2.2 Homogeneity

It is necessary for the entire volume of the phantom to have uniform optical properties to ensure homogeneous bleaching and consistent fluorescence measurements. To determine the homogeneity, several measurements of optical properties were made at random locations across the surface of a typical phantom. The average optical properties were: $\mu_s' = 0.99 \pm 0.04\ \text{mm}^{-1}$ and $\mu_a = 0.019 \pm 0.004\ \text{mm}^{-1}$, illustrating the homogeneity of the phantoms, with most of this variation arising from the measurement technique.

4.2.3 Index of Refraction Measurement

The index of refraction of the phantom must be known for the determination of light behaviour at the air-phantom boundary. Following the method outlined by Li and Xie (1996), resin was cast as a semi-cylindrical lens. By measuring the critical angle in contact with either air or water for both green and red laser light, the index of refraction was determined using Snell's Law

$$n_{phantom} = \frac{n_{air\text{ or }water}}{\sin\theta_{critical}}. \tag{57}$$

Using the refractive indices for air and water at the wavelengths of interest (Hale and Querry 1973), the resin was found to have an index of refraction of 1.48±0.01 at 630 nm.

4.2.4 Bleach Rate Determination

In order to make comparisons with mathematical modelling, the experimental bleach rate of the photosensitizer contained in the phantom was measured at 630 nm. If a low photosensitizer concentration is used such that photobleaching will not cause appreciable change to the distribution of drug and hence bleaching fluence rate, the following relationship is true for constant geometry

$$\frac{F(t)}{F(0)} = e^{-\phi Bt} \tag{58}$$

where $F(t)$ is the fluorescence, ϕ is the bleaching fluence rate, B is the bleach rate of the photosensitizer (in cm^2/J) and t is total irradiation time. Rearranging gives a simple relationship for bleach rate

$$B = \frac{1}{\phi t}\ln\left[\frac{F(0)}{F(t)}\right] \tag{59}$$

which is easily calculated from a fluence rate and the slope of a fluorescence versus time graph.

The fluorescence measurements were made on semi-micro cuvettes containing Photofrin, resin and catalyst only. In order to assure that the Photofrin was sufficiently dilute, the concentration was calculated so that the maximum absorption of excitation light would be less than one percent for a 5 mm path length through the cuvette. This gave a Photofrin concentration of 2.4 μg/mL based on an extinction coefficient of 0.0009 mm^{-1}/(μg/mL) at 630 nm (as determined by dilution experiment).

A laser source providing approximately 150 mW/cm^2 of 632 nm light was used to bleach the sample and fluorescence measurements were made with a spectrometer through a single optical fibre positioned at 90 degrees to the bleaching light. A 645 nm cut-on filter was used to eliminate most of the reflected 630 nm light while still allowing for determination of the 690 nm fluorescence peak height by fitting a Gaussian to the peak and a polynomial (third, fourth or fifth order) to the background. Also, a 5 percent correction for reflection at the air/cuvette boundary, based on mismatched indices of refraction, was made to the bleaching fluence rate. Figure 4.2.1 shows the resultant decrease in fluorescence for the Photofrin in resin only. The data strongly suggest that the reaction does not obey first order kinetics. There is an initial rapid decrease in fluorescence followed by a fairly linear period before the data become rather noisy. For the purpose of the modelling, which assumes first order bleaching kinetics, the intermediate linear section was presumed to provide the best indication of the bleach rate. This will be further discussed in the experimental results. Following data manipulation, the bleach rate was determined to be 0.015 cm^2/J.

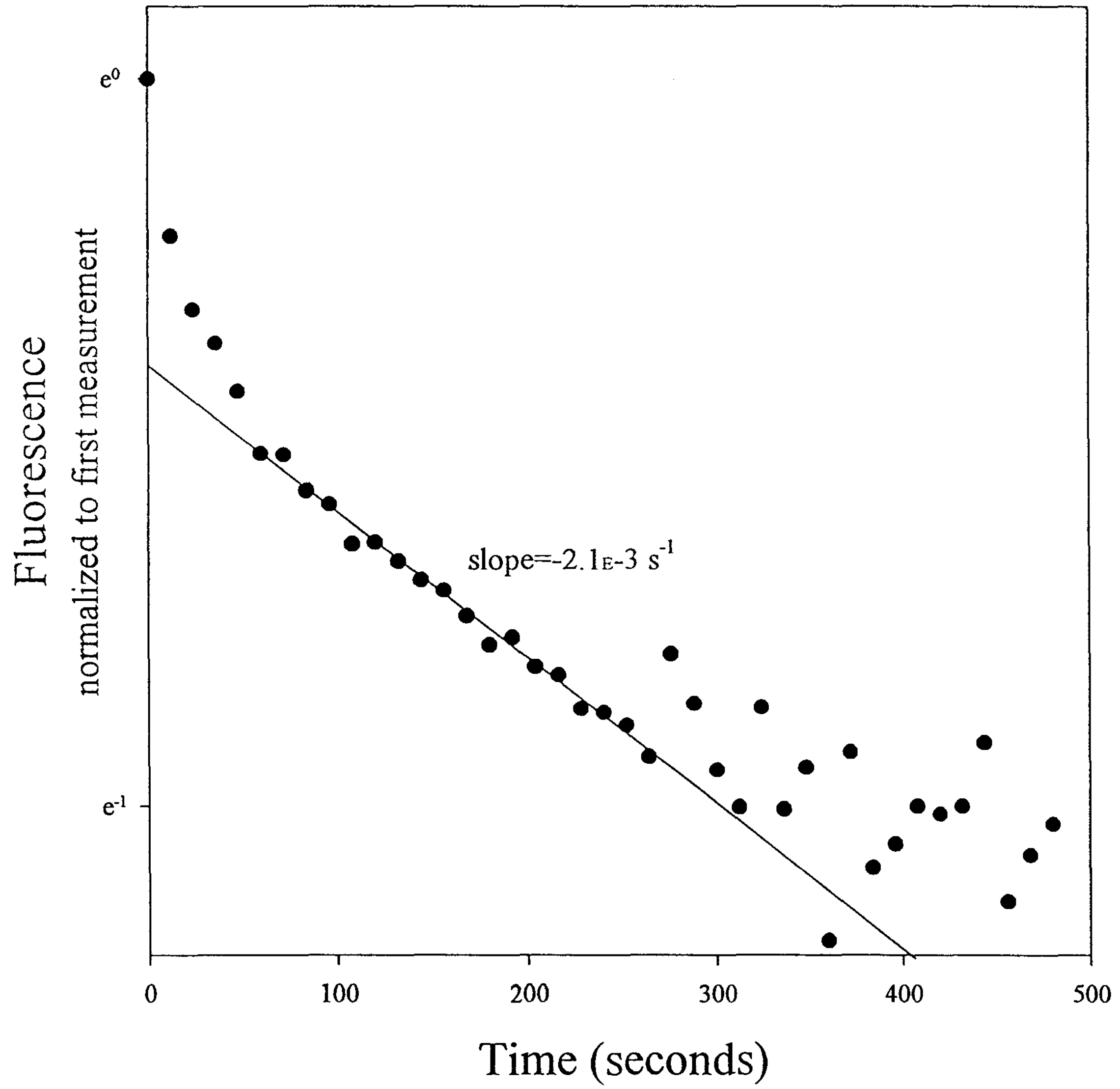

Figure 4.2.1 Fluorescence decrease as a function of time for a cuvette containing a very low concentration of Photofrin in resin. The fitted line shown has a slope of -2.1E-3 s^{-1} giving a bleach rate of 0.015 cm^2/J.

4.3 Experimental Design and Methods

4.3.1 Phantoms

Using the procedure previously described, a set of phantoms was developed having varied optical properties. A standard phantom was chosen to have the following characteristics: $\mu_s' = 1.00$, $\mu_{a_o} = 0.02$ and $\mu_{a(drug)}$=0.04 mm^{-1}. Four phantoms, named black, blue, red and purple, were made to have these properties in order to test the reproducibility of the results obtained. Measurement after completion gave the optical properties listed in table 4.3.1. In order to determine the drug and tissue contributions to the total absorption coefficient, two additional phantoms were created: grey, which contained no Photofrin, and white, which had no background absorber or Photofrin.

	μ_s' (mm^{-1})		**total μ_a (mm^{-1})**		**μ_{ao} (mm^{-1})**		**$\mu_{a(drug)}$* (mm^{-1})**	
Phantom	630 nm	690 nm	630 nm	690 nm	630 nm	690 nm	630 nm	690 nm
Red	0.99	0.96	0.083	0.051	0.020	0.020	0.063	0.031
Blue	0.97	0.99	0.083	0.043	0.020	0.020	0.063	0.023
Black	1.02	1.01	0.082	0.044	0.020	0.020	0.062	0.022
Purple	1.01	1.00	0.079	0.047	0.020	0.020	0.059	0.027
White	0.99	0.97	0.002	0.001	0.002	0.001	-	-
Grey	1.02	1.01	0.021	0.020	0.021	0.020	-	-

Table 4.3.1: Measured optical properties for standard phantoms. The values shown are an average of three measurements. The asterisk (*) indicates that the drug absorption coefficient is the total absorption coefficient minus background, determined from grey phantom.

In each, the scatter coefficient was determined to be approximately 1.00 mm^{-1}, as expected. Background absorption was negligible in the white phantom and was found to be 0.020 mm at both bleaching and fluorescence wavelengths in the grey phantom. This value was accepted as the endogenous absorption for all standard phantoms, allowing for the calculation of drug absorption coefficient by simple subtraction.

By varying the concentration of added components, the optical properties were independently manipulated about the standard values with the target values given in table 4.3.2.

Phantom	**μ_s' (mm^{-1})**	**μ_{ao} (mm^{-1})**	**$\mu_{a(drug)}$ (mm^{-1})**
μ_{ao}lo	1.00	**0.01**	0.04
μ_{ao}hi	1.00	**0.04**	0.04
druglo	1.00	0.02	**0.02**
drughi	1.00	0.02	**0.08**
$\mu_s$lo	**0.50**	0.02	0.04
$\mu_s$hi	**1.50**	0.02	0.04

Table 4.3.2: Array of target optical properties for varied phantoms at 630 nm. Bold type indicates values different from the standard.

Difficulty was encountered when attempting to determine the optical properties of some of these phantoms. In the cases of high absorption or low scattering the analyses by both neural network and non-linear curve fitting were not acceptable, leading to the incomplete information in table 4.3.3. Since the determination of optical properties is based on diffusion theory, which is most appropriate for highly scattering media, it is not surprising that ideal results were not obtained for these phantoms. It is assumed that the careful variation in added components has ensured optical properties close to those desired.

	μ_s' (mm^{-1})		total μ_a (mm^{-1})		μ_{ao} (mm^{-1})		$\mu_{a(drug)}$* (mm^{-1})	
Phantom	630 nm	690 nm	630 nm	690 nm	630 nm	690 nm	630 nm	690 nm
μ_{ao}lo^	0.96	0.97	0.068	0.037	0.008	0.010	0.060	0.027
μ_{ao}hi^	-	0.97	-	0.057	-	0.030	-	0.027
druglo	1.00	0.98	0.051	0.034	0.020	0.020	0.031	0.014
drughi	-	0.98	-	0.059	-	0.020	-	0.039
$\mu_s$lo	-	-	-	-	-	-	-	-
$\mu_s$hi	1.55	1.40	0.061	0.052	0.020	0.020	0.041	0.032

Table 4.3.3: Measured optical properties for the phantoms having varied ingredients, again averages of three measurements. The $\mu_{a(drug)}$ values for the phantoms having varied background absorber (^) were taken as an average of all standard phantoms so that μ_{ao} could be calculated from the total μ_a. For the remaining phantoms, the asterisk (*) again indicates that $\mu_{a(drug)}$ was found by subtracting the background absorption found from the grey phantom from the total μ_a.

Determined optical properties at the excitation wavelength (514 nm) were unsatisfactory in all cases, likely due to the much higher absorption and inherent difficulty encountered by the diffusion theory models in this situation. As a result, values for scattering and background absorption were assumed constant, while photosensitizer absorption was considered three times higher than the 630 nm value. These absorption estimates are based on transmission measurements at 515 nm, performed in a spectrometer on cuvettes containing only absorbing components and resin.

4.3.2 Irradiation

In order to approximate a semi-infinite medium, the dimensions of the phantoms were made to be several times larger than the average penetration depth of the light. For the optical properties of the phantoms used, the average path length of the photobleaching light was never greater than 1 mm, allowing a maximum of 3 percent transmission through the 3.0 cm depth. A diameter of 8.0 cm was used, however bleaching was performed on the centre 6.0 cm, and measurements were made on the inner 4.0 cm to avoid boundary effects. In order to ensure bleaching occurred evenly across the entire phantom, a slide projector was used with a 630 nm band pass filter to give a homogeneous distribution of treatment light. Careful measurement of the bleaching fluence rate across the surface of the phantom was performed using an optical power meter (Oriel) and had less than five percent variation. Monitoring was performed throughout the course of the experiment to verify the consistency of the bleaching fluence rate.

Fluorescence excitation light was provided by the 514 nm line of an Argon ion laser focused through the source fibre of a flat, black probe. Encompassing the source fibre are several collection fibres at known radii ranging between 0.33 and 10.0 mm. These collect light from the phantom and deliver it to a spectrometer, passing through a 540 nm cut-on filter along the way to prevent saturation of the CCD by the excitation light. Variable attenuators allowed for adjustment of the detected light intensity so that enough counts were obtained in the more distant detectors without saturation of the close tracks. This is accounted for by calibrating the attenuator effect using an integrating sphere and a broad band source (Farrell *et al* 1994).

Since the fluence rate provided by the slide projector was in the order of a 2-5 mW/cm^2, lengthy periods of bleaching were required in order to observe an appreciable decrease in fluorescence. Bleaching was done for periods of five minutes, followed by removal of the phantom from the bleaching light and subsequent fluorescence measurement. By securing the phantom with a clamp attached to a retort stand it was possible to swing the phantom out of the treatment light, and then return it to its original position. In order to minimize the bleaching caused by the 200 mW/cm^2 fluorescence excitation light, measurements were never taken in the same place twice, and the excitation period was typically only 2-3 seconds. Although a small amount of photobleaching will have occurred, it should be negligible compared with that of the treatment light over the course of the experiment.

4.3.3 Analysis of Fluorescence

For the purple phantom, calibrated fluorescence spectra for twelve detection fibres at radii between 0.33 and 4.50 mm are shown in figure 4.3.1. The 630 nm and 690 nm fluorescence peaks typical of Photofrin are clearly seen, as is a broad band of fluorescence centred around 650 nm. This unexpected fluorescence is thought to be a photoproduct created during the treatment of the phantom and is common when exciting with low wavelengths (Moan 1986). These spectra were obtained after ten minutes of treatment, during which time photoproducts have been created mainly near the surface where the

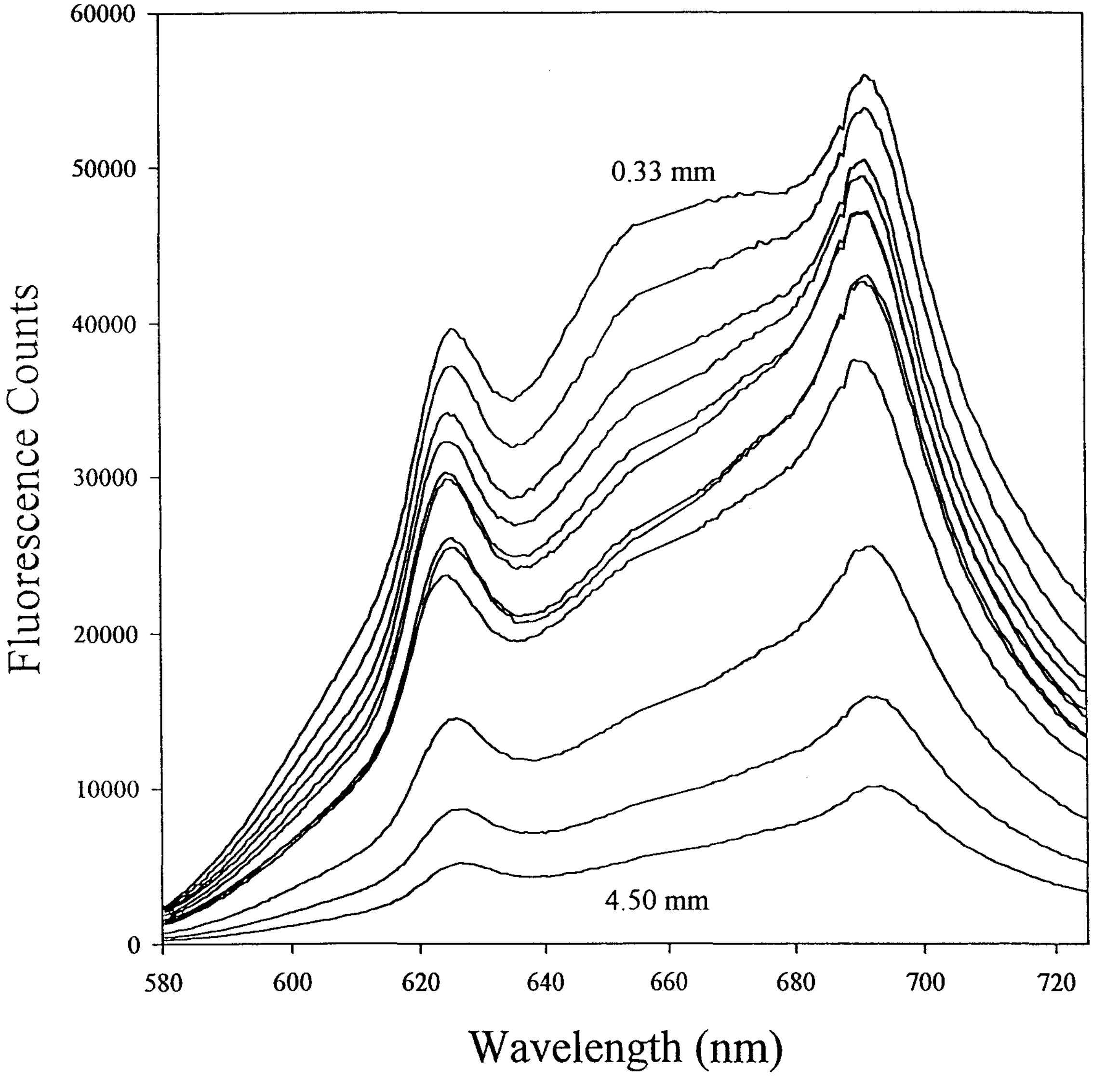

Figure 4.3.1 Fluorescence spectra at several detection radii obtained from a single measurement using 515 nm excitation on Purple phantom.

bleaching fluence is much higher. As a result, the closest detection fibres, which collect more shallow light, show the greatest amount of photoproduct fluorescence. These photoproducts are very clearly seen in figure 4.3.2, where they can be observed to increase from the initial $\Psi=0$ curve, followed by gradual photobleaching. Also obvious is the relative decrease in the 630 and 690 nm peak heights over the course of the treatment.

In order to obtain useful information from these fluorescence spectra, the fluorescence in the two peaks was quantified. Since there is a large background of fluorescence present, absolute peak heights are useless, and curve fitting is required to determine the peak areas. Figure 4.3.3 shows the results of fitting a polynomial background with two Gaussian peaks centred at 635 and 695 nm. Subtraction of the background from the original fluorescence spectrum clearly shows the two fluorescence peaks. Since the amplitude of a Gaussian is proportional to its area, the fitted peak heights can be plotted against scaled photobleaching fluence, as shown in figure 4.3.4. This result agrees well with the mathematically predicted shape of the fluorescence curve from a single fibre, first demonstrated in figure 2.2.2a. As expected, similar results are observed for all fibres in figure 4.3.5a. The variation between fibres can be better visualized by normalizing to a single fibre, as figure 4.3.5b illustrates. Although the variation is much less than in the modelling (figures 2.3.1b and 2.3.6b), there is a larger relative increase in fluorescence at the more distant fibres. This normalization also removes most of the variability between measurements which may result from variations in probe coupling with the phantom and excitation fluence rate (figure 4.3.5a). Finally, figure 4.3.6 illustrates the change in radially resolved fluorescence that occurs as

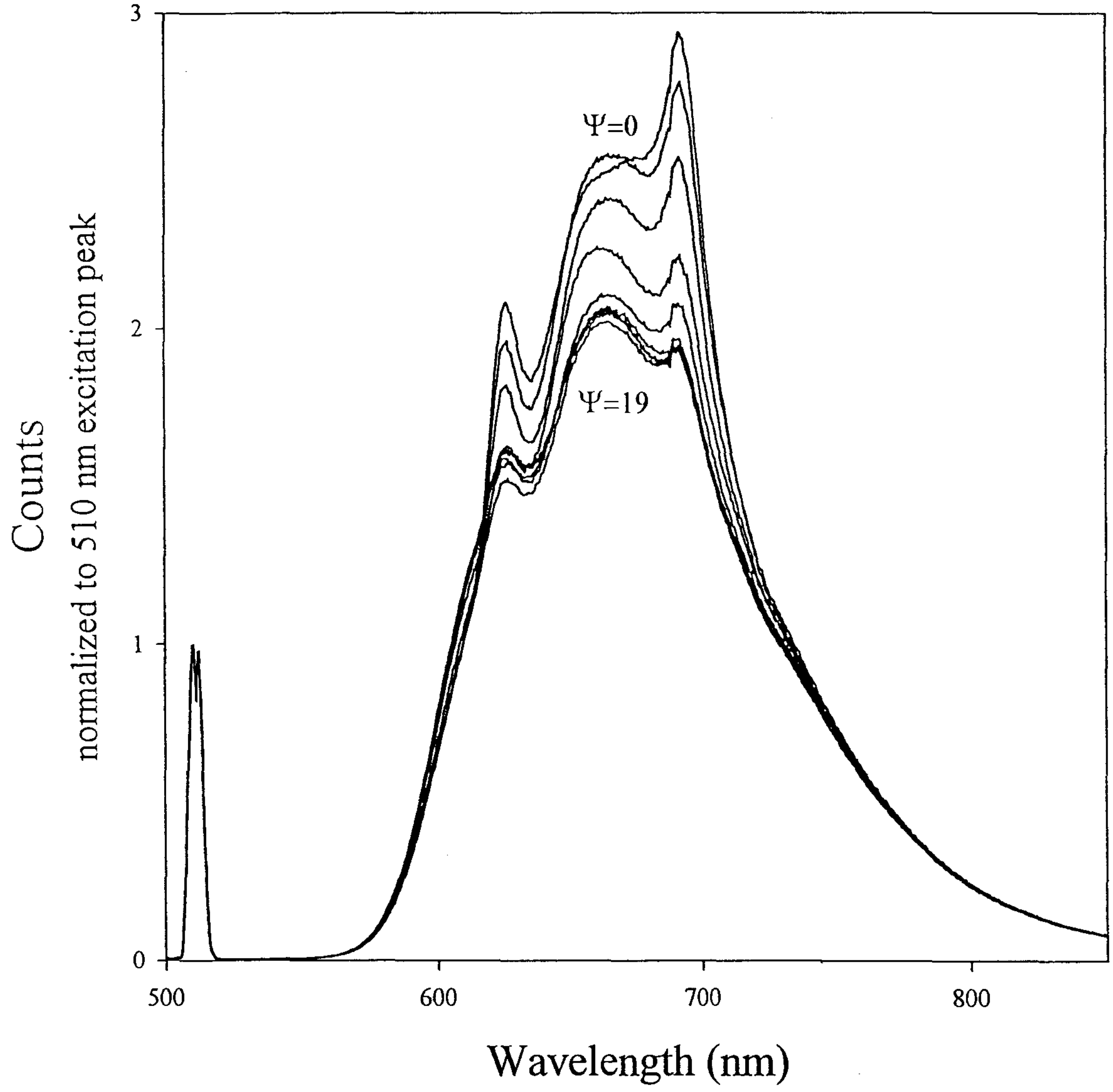

Figure 4.3.2 Fluorescence spectra from Purple phantom as treatment progresses, illustrating the occurrence of photobleaching. The spectra were normalized to the 515 nm excitation peak.

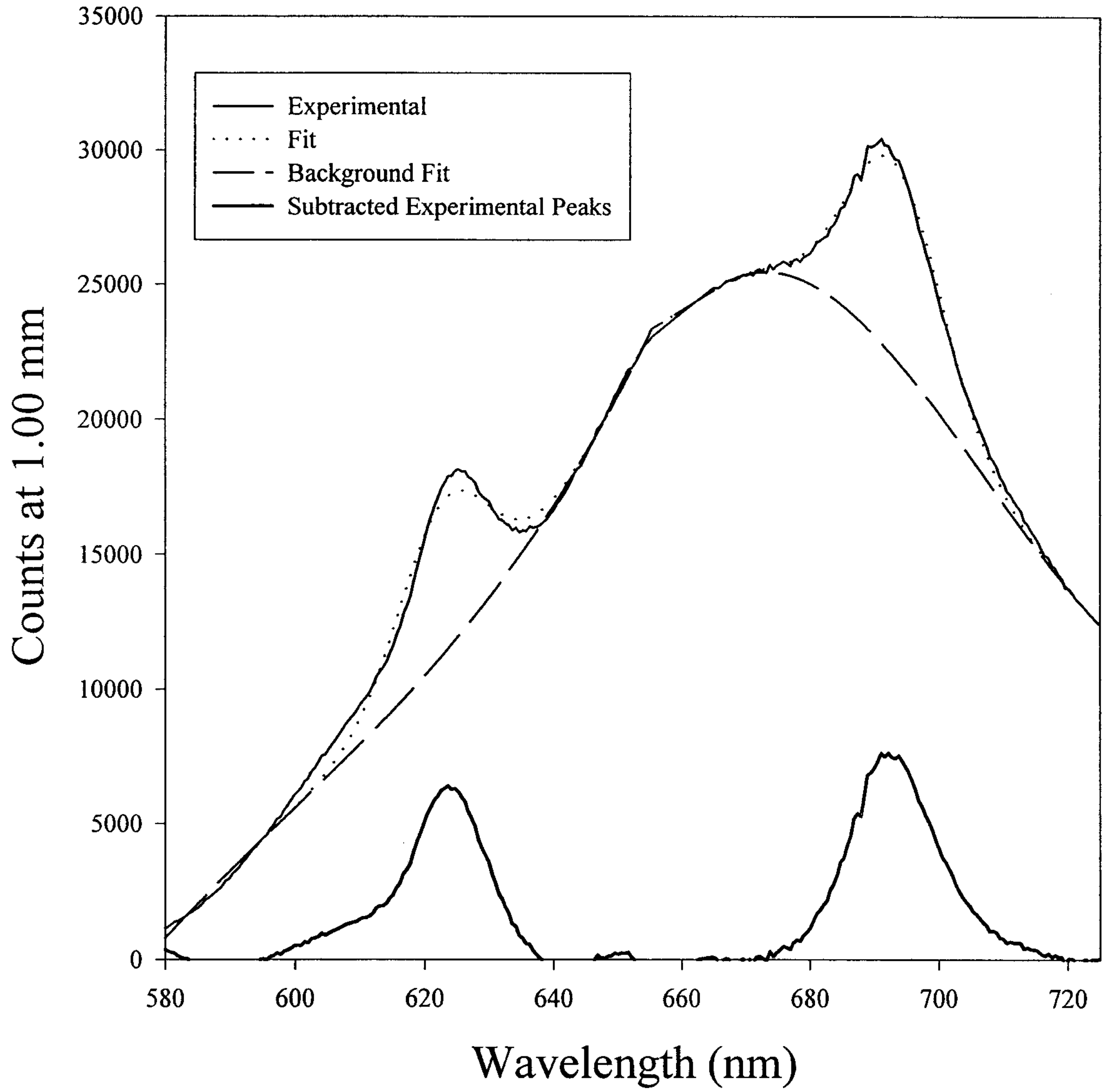

Figure 4.3.3 A typical fitted fluorescence spectrum using a polynomial background with two Gaussians. The background is shown, as are the 630 nm and 690 nm fluorescence peaks resulting from subtraction.

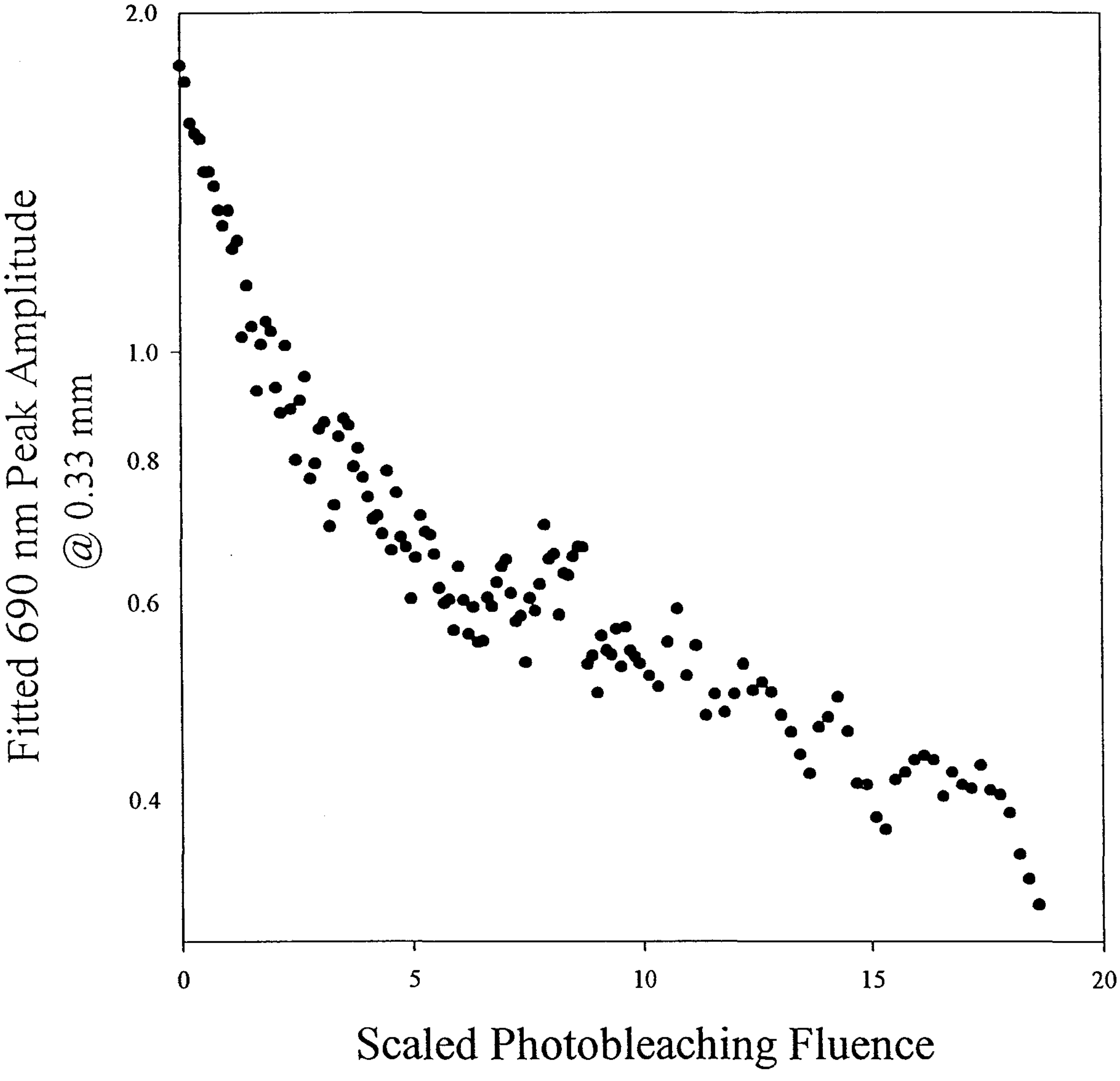

Figure 4.3.4 Fitted 690 nm fluorescence peak amplitude as a function of scaled photobleaching fluence for a single fibre at 0.33 mm on the surface of Purple phantom.

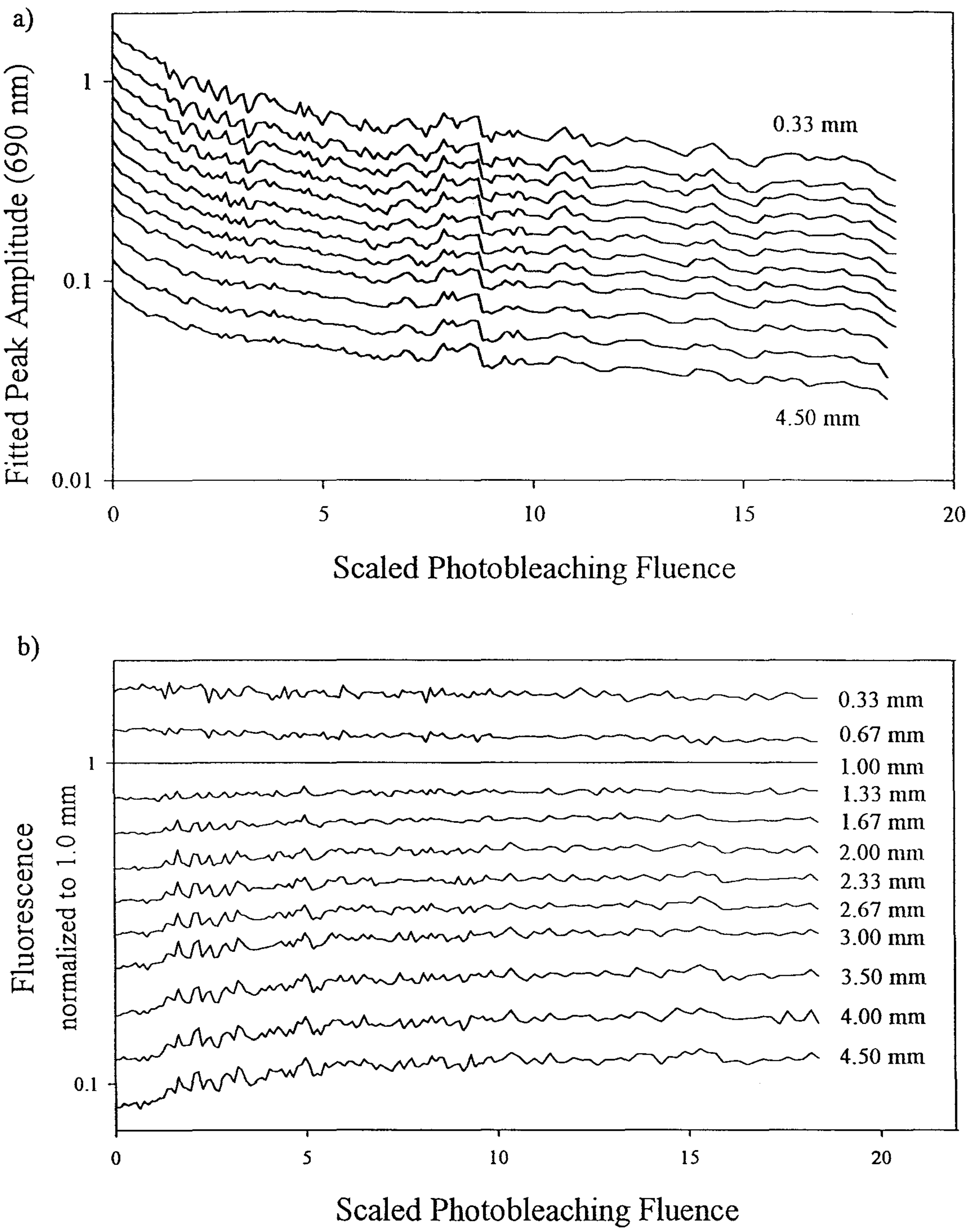

Figure 4.3.5 **a)** 690 nm fluorescence as a function of scaled photobleaching fluence for 12 detection fibres at different radii.

b) Fluorescence versus scaled photobleaching fluence normalized to 1.00 mm to remove variation between measurements.

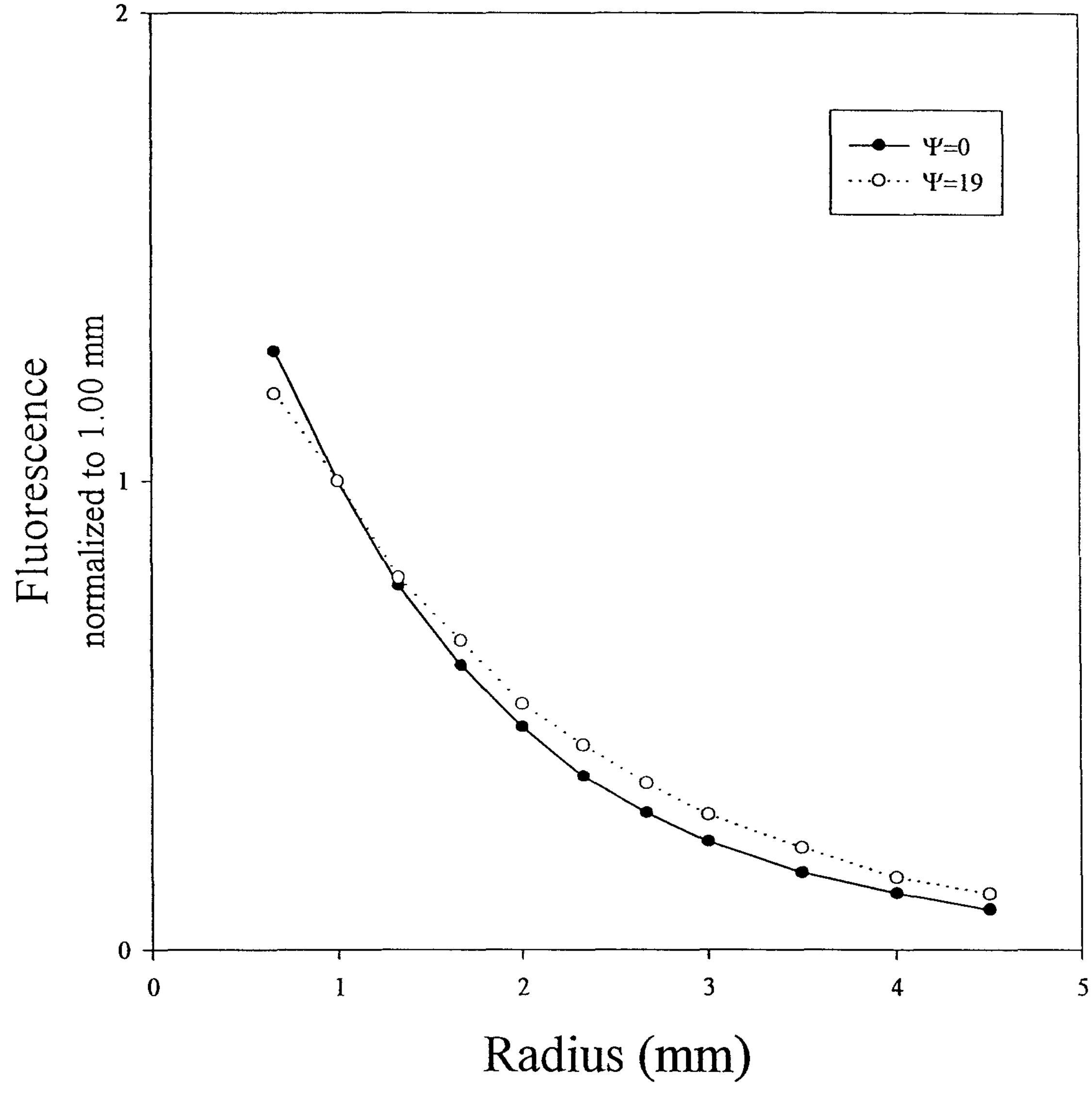

Figure 4.3.6 Fluorescence as a function of radius prior to any photobleaching, and at the completion of the bleaching experiment. The results are from Purple phantom, and are normalized to 1.00 mm.

treatment progresses. It is this variation that will allow the determination of both virtual plane and source depths and ultimately lead to predictions of necrosis depth.

4.4 Experimental Results

4.4.1 Virtual Plane Depth

Using the measured optical properties of the phantoms, the scatter dominated pencil beam excitation model was used to generate curves representing the total probability of fluorescence escape from a plane of fluorescence at a single depth as a function of radius (figure 4.4.1a), similar to those shown in figure 2.3.4b. The radial fluorescence data in figure 4.3.6 were compared with these data and best fit curves were determined by minimizing the Chi-squared value, resulting in the representative virtual plane depths shown. The fitted curves matched the experimental data quite well (figure 4.4.1b), and the virtual plane depth increased with bleaching fluence, as anticipated. This change in virtual plane depth is better illustrated in figure 4.4.2 which gives the gradual increase in depth as a function of photobleaching fluence. This shows the same general shape as that predicted by the modelling (figure 2.3.5a). Unlike the theoretical curve, the experimental plane depth has very little penetration as treatment progresses, although it does originate at a depth close to one mean free path, as anticipated.

The progress of the virtual plane depth for all of the standard phantoms can be seen in figure 4.4.3. All exhibit a similar increase over time, and all but black start at the expected depth indicating decent reproducibility. Unfortunately, in order to allow proper

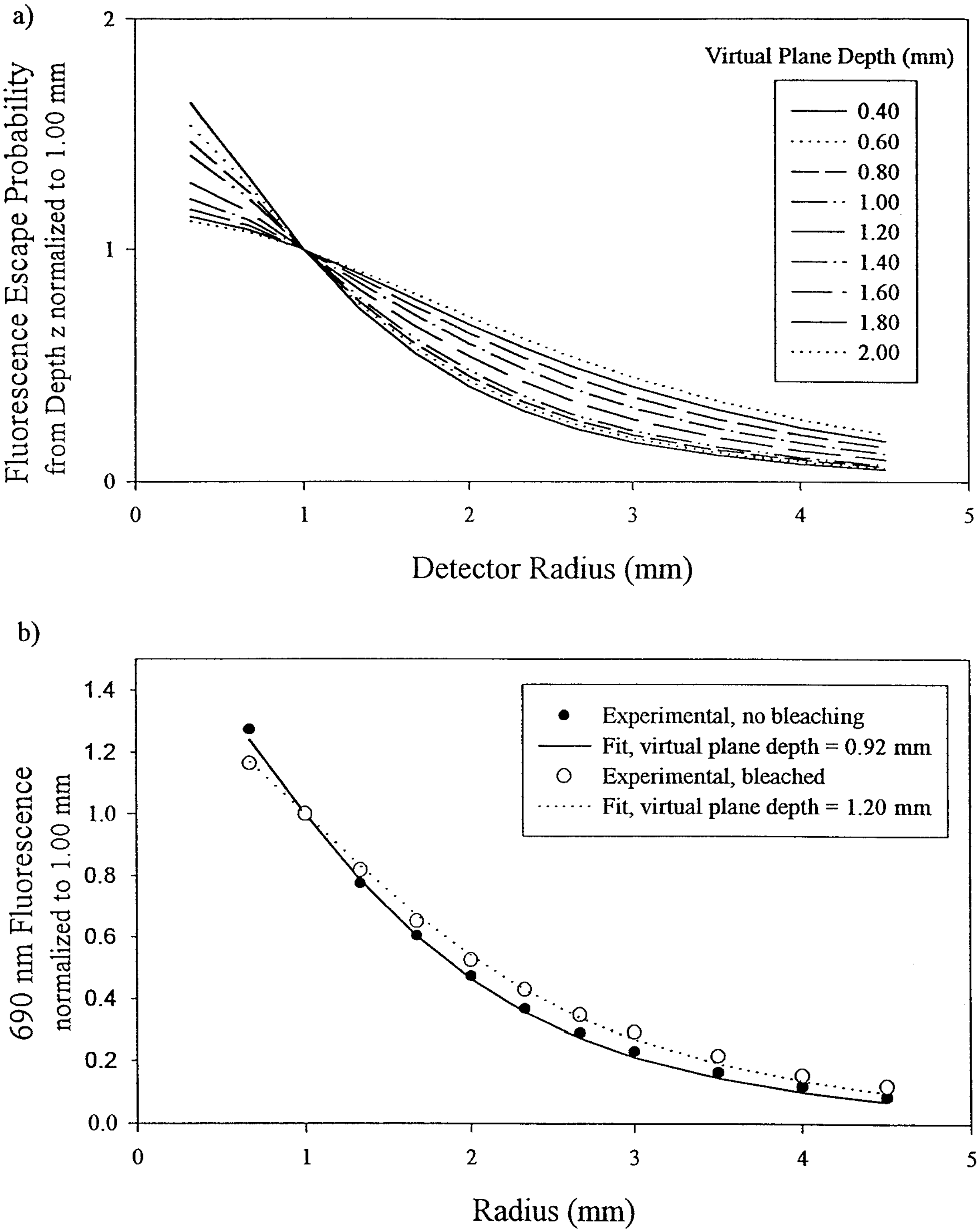

Figure 4.4.1 **a)** Total fluorescence escape probability from a virtual plane as a function of radius for several depths, normalized to 1.00 mm. Standard initial properties for the scatter dominated model were used.
b) Fluorescence versus radius curves and their corresponding fits giving the depth of the virtual plane prior to bleaching, and at $\Psi = 19$.

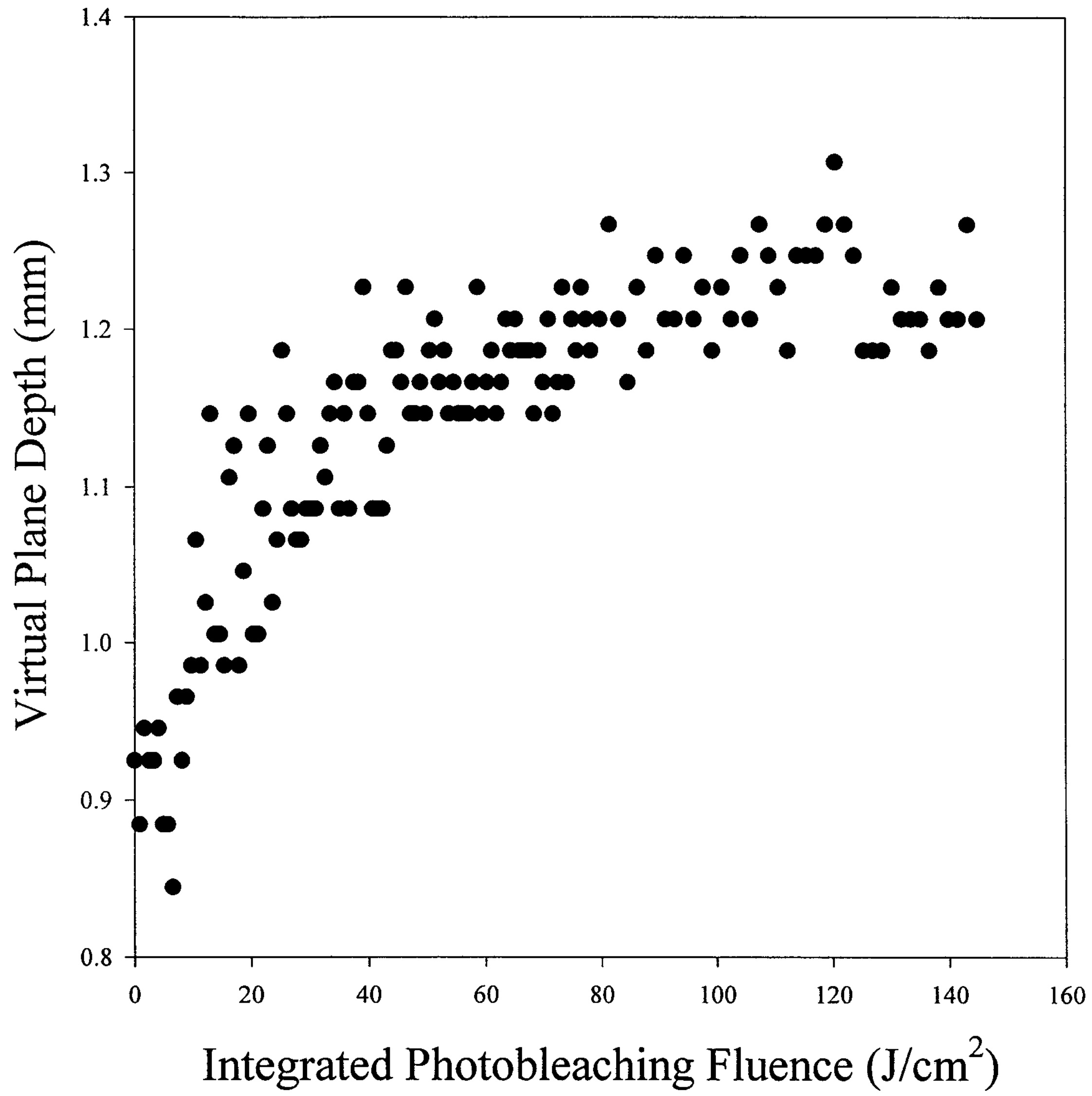

Figure 4.4.2 Virtual plane depth as a function of integrated photobleaching fluence for Purple phantom.

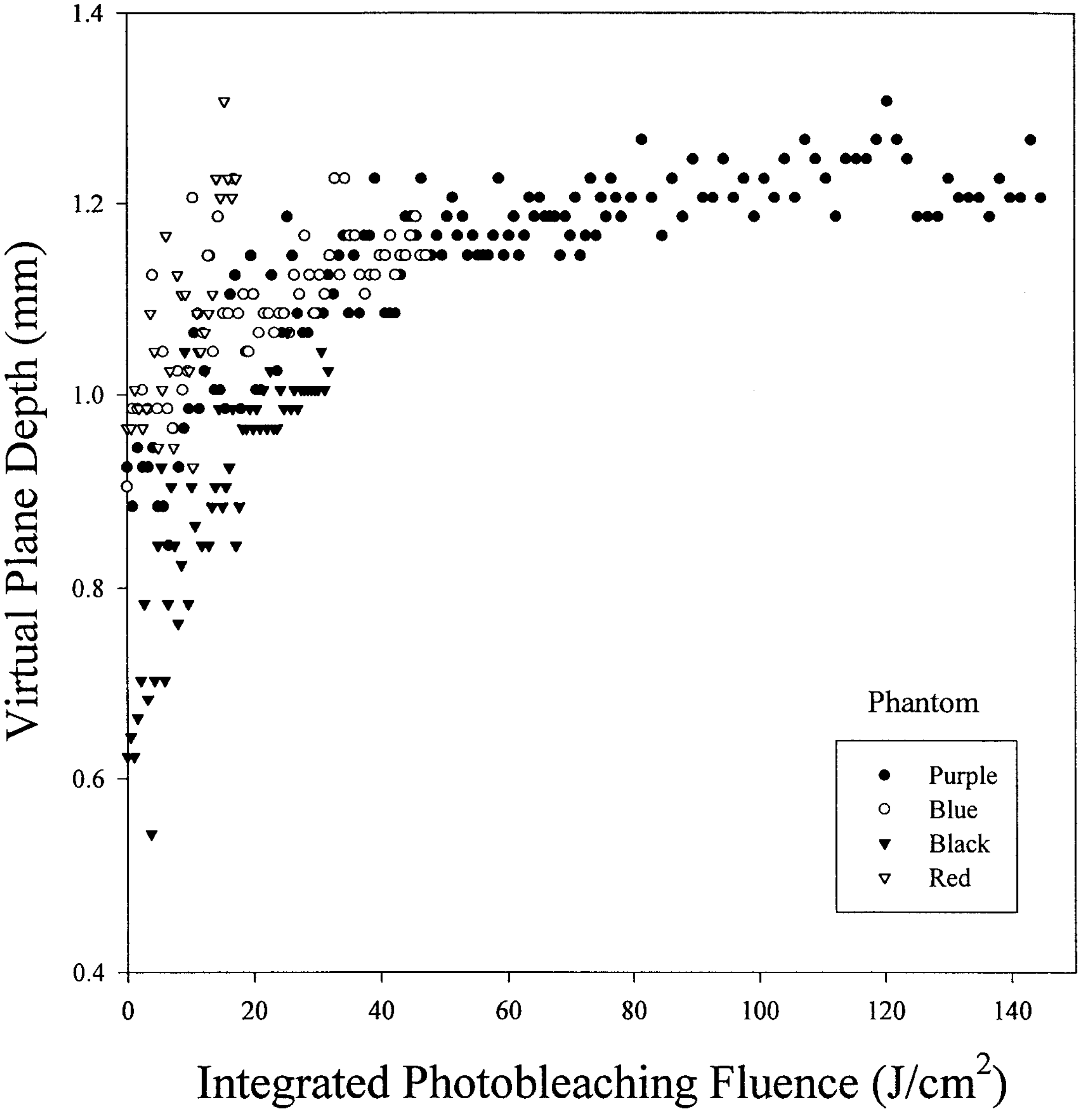

Figure 4.4.3 Virtual plane depth as a function of integrated photobleaching fluence for all four standard phantoms.

comparisons, treatment times should have been extended for the black, blue and red phantoms to compensate for the low bleaching fluence.

Variation in experimental virtual plane depth was investigated for altered initial optical properties, using the measured values given in table 4.3.3. Figure 4.4.4 shows the experimental and predicted virtual plane depths for different initial photosensitizer concentrations. The three experimental curves in figure 4.4.4a are well-differentiated and are ordered as predicted in figure 4.4.4b, although drughi is generally not as deep as expected and has a larger spread in the data points. This is somewhat expected since the diffusion model does not work as well for situations involving high absorption.

Data obtained for three phantoms with dissimilar background absorption coefficients and the corresponding modelled outcomes are seen in figures 4.4.5a and 4.4.5b, respectively. Although it is difficult to differentiate between the experimental points, the ua0lo data seems to be slightly higher than the standard, while the ua0hi is generally lower, not disagreeing with the curves in figure 4.4.5b. All three have similar initial virtual plane depths which is reasonable considering only a small variation in mean free path exists for small changes to μ_{ao}.

Finally, altered scattering coefficient is investigated in figure 4.4.6. For low scattering, the model failed to make predictions about virtual plane depth which is anticipated considering this case violates the principal assumption that $\mu_s' \gg \mu_a$. On the other hand, although the data are fairly noisy, the highly scattering phantom behaves as predicted by figure 4.4.6b since the virtual plane depth is originally shallower than the standard phantom, and increases more slowly.

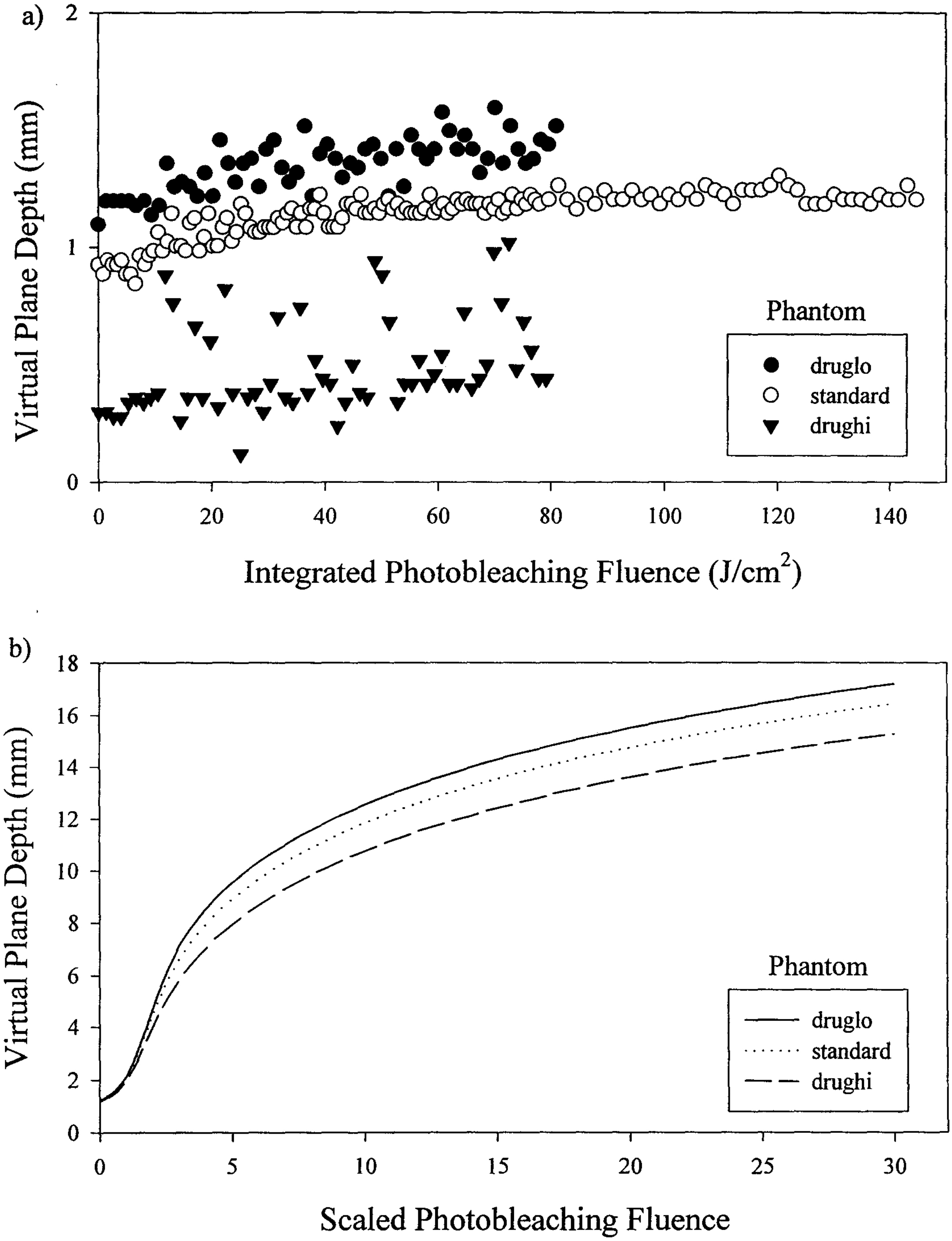

Figure 4.4.4 **a)** Experimentally determined virtual plane depth as a function of integrated bleaching fluence for varied initial drug concentration.
b) Predicted virtual plane depth versus scaled photobleaching fluence using the scatter dominated model with measured phantom optical properties.

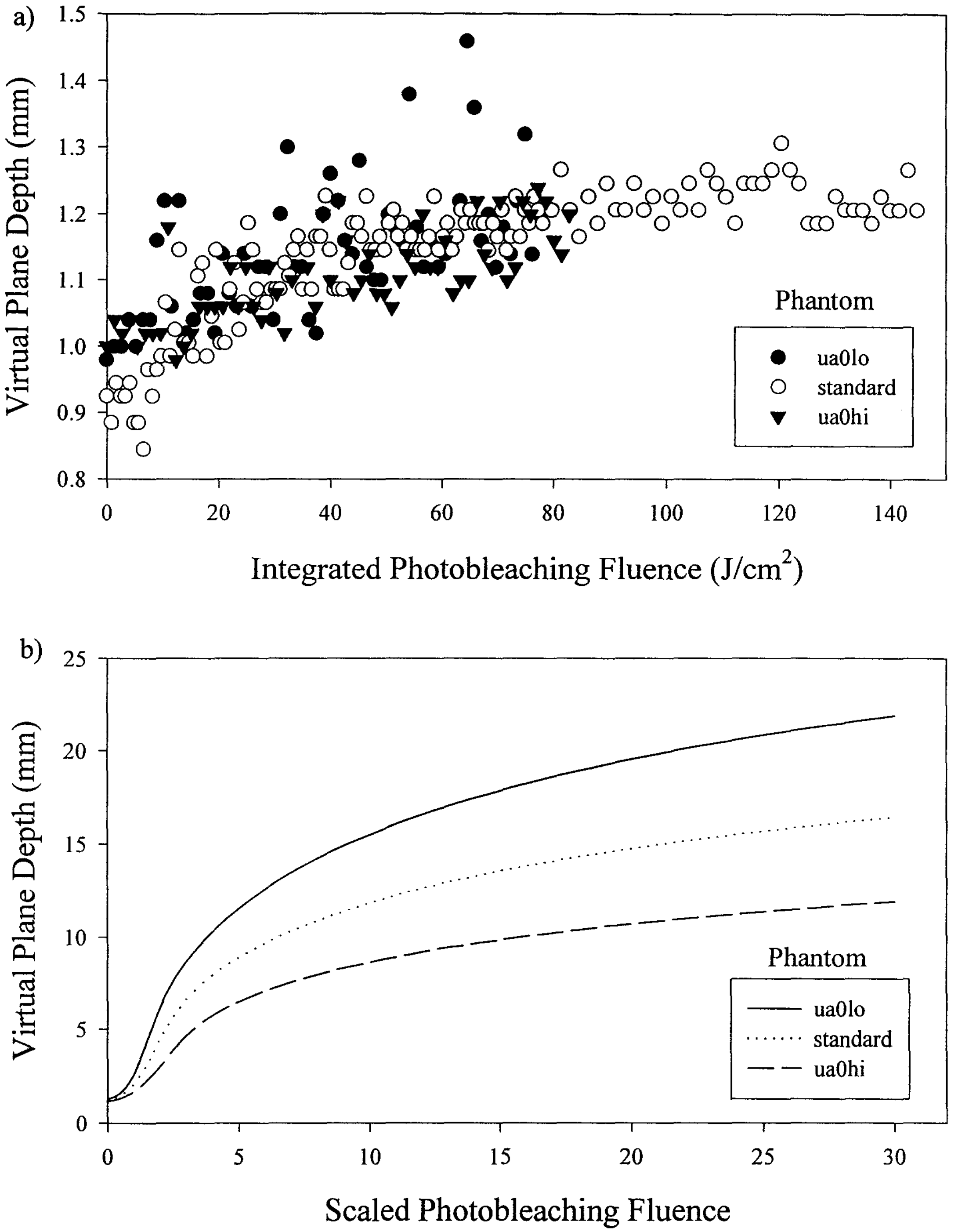

Figure 4.4.5 **a)** Experimentally determined virtual plane depth as a function of integrated bleaching fluence for varied endogenous tissue absorption.

b) Predicted virtual plane depth versus scaled photobleaching fluence using the scatter dominated model with measured phantom optical properties.

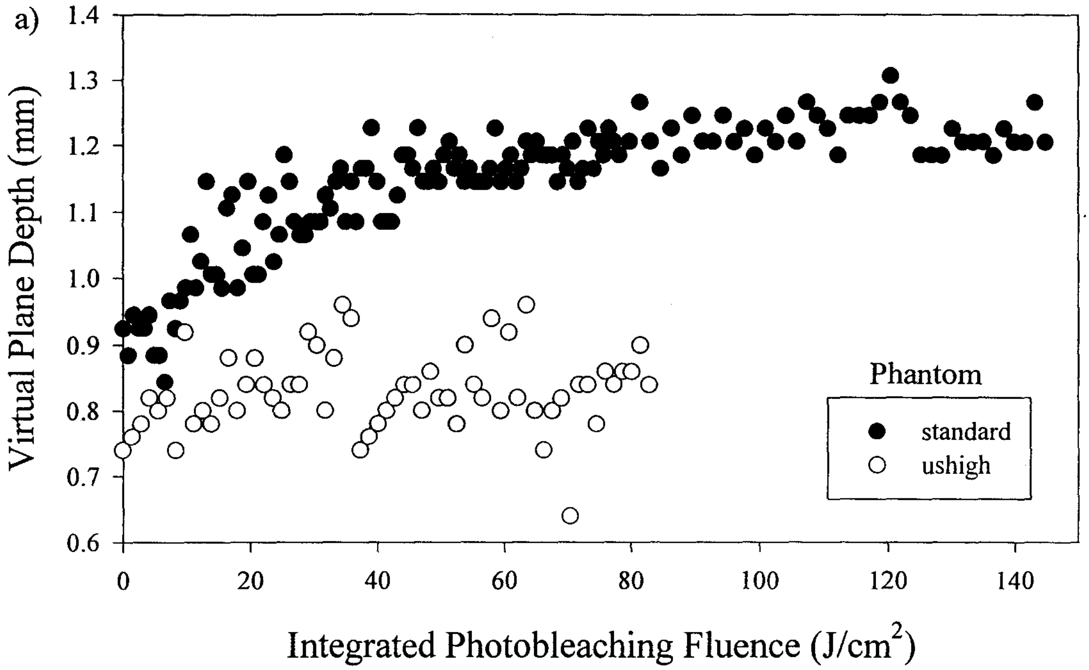

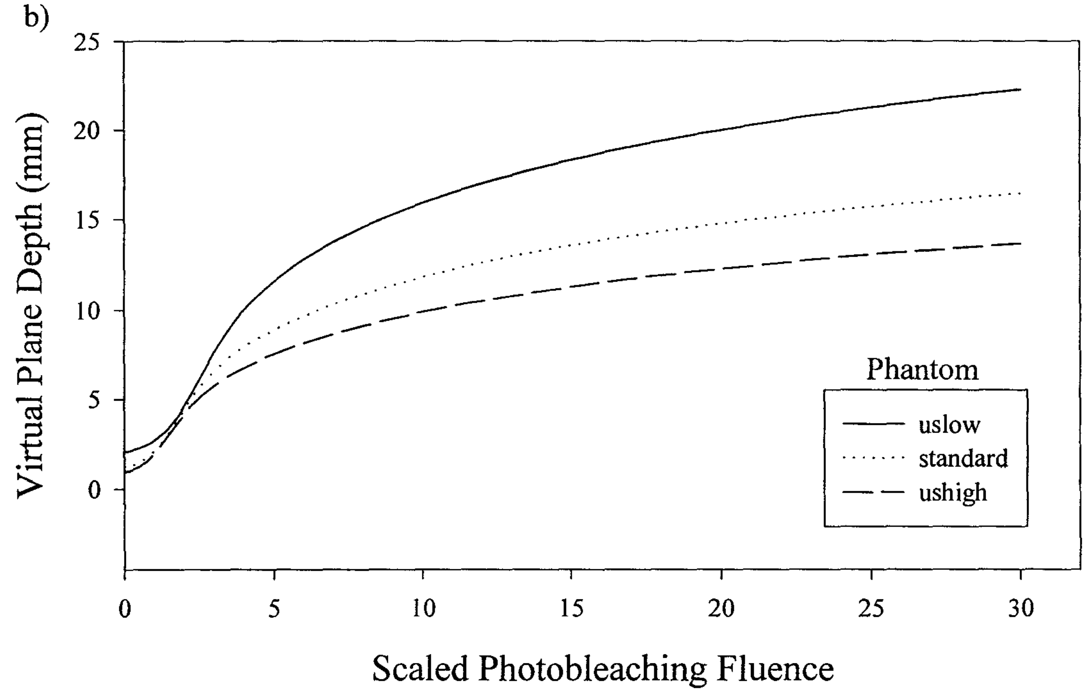

Figure 4.4.6 **a)** Experimentally determined virtual plane depth as a function of integrated bleaching fluence for varied tissue scattering coefficient.

b) Predicted virtual plane depth versus scaled photobleaching fluence using the scatter dominated model with measured phantom optical properties.

4.4.2 Virtual Source Depth

Similar analysis can be performed using the pencil beam excitation model that assumes absorption dominates. Using equation 18, which describes the fluorescence distribution arising from a single fluorescence point, the radial fluorescence measurements (figure 4.3.6) can be fitted to determine a depth for the virtual source, z_o. The effective attenuation coefficient is fitted simultaneously, and once determined is assumed constant at the fluorescence wavelength. As a result, no *a priori* information is required concerning tissue optics to determine the virtual source depth. Figure 4.4.7 shows the fluorescence data and fitted curves with their resulting virtual source depths at the beginning and end of the purple phantom bleaching experiment. As with the virtual plane, fits are good and the virtual source depth increases during the course of treatment. The curve of virtual source depth as a function of photobleaching fluence is depicted in figure 4.4.8, agreeing very well with the shape of the predicted curve in figure 2.3.9a. Similar to the virtual plane results, the virtual source does not penetrate nearly as deeply as the modelling would suggest it should for the input parameters used. The virtual source depth is expected to originate at a depth of one mean free path, or 0.83 mm, however the experimentally determined value is initially deeper, at 1.1 mm. The remaining standard phantoms also have virtual source depths originating near 1.1 mm, as observed in figure 4.4.9 which shows excellent agreement between all four phantoms with the standard optical properties.

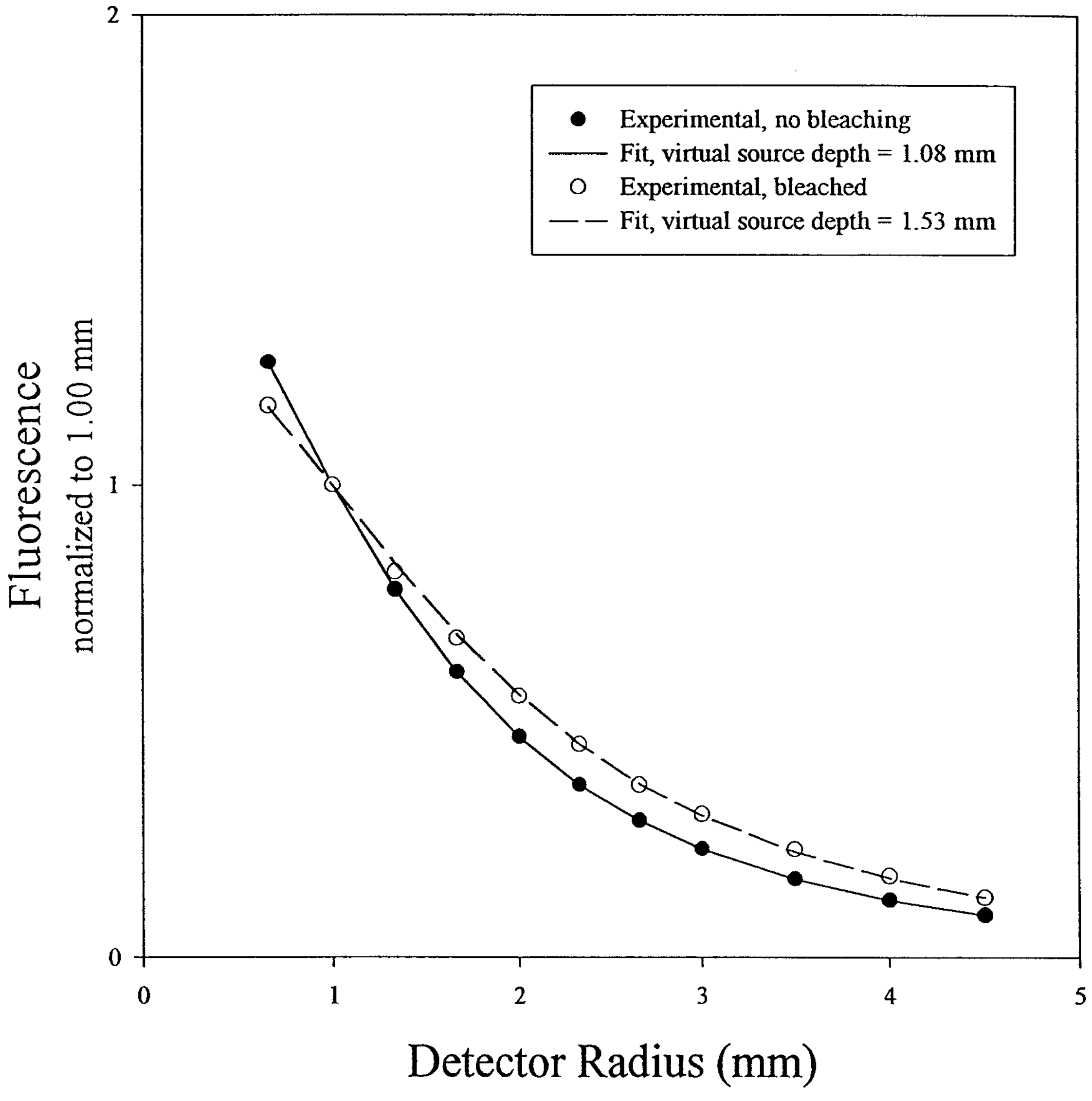

Figure 4.4.7 Fluorescence versus radius curves and their corresponding fits, all normalized to 1.00 mm, giving the depth of the virtual source prior to any photobleaching, and at the completion of the photobleaching experiment ($\Psi = 19$).

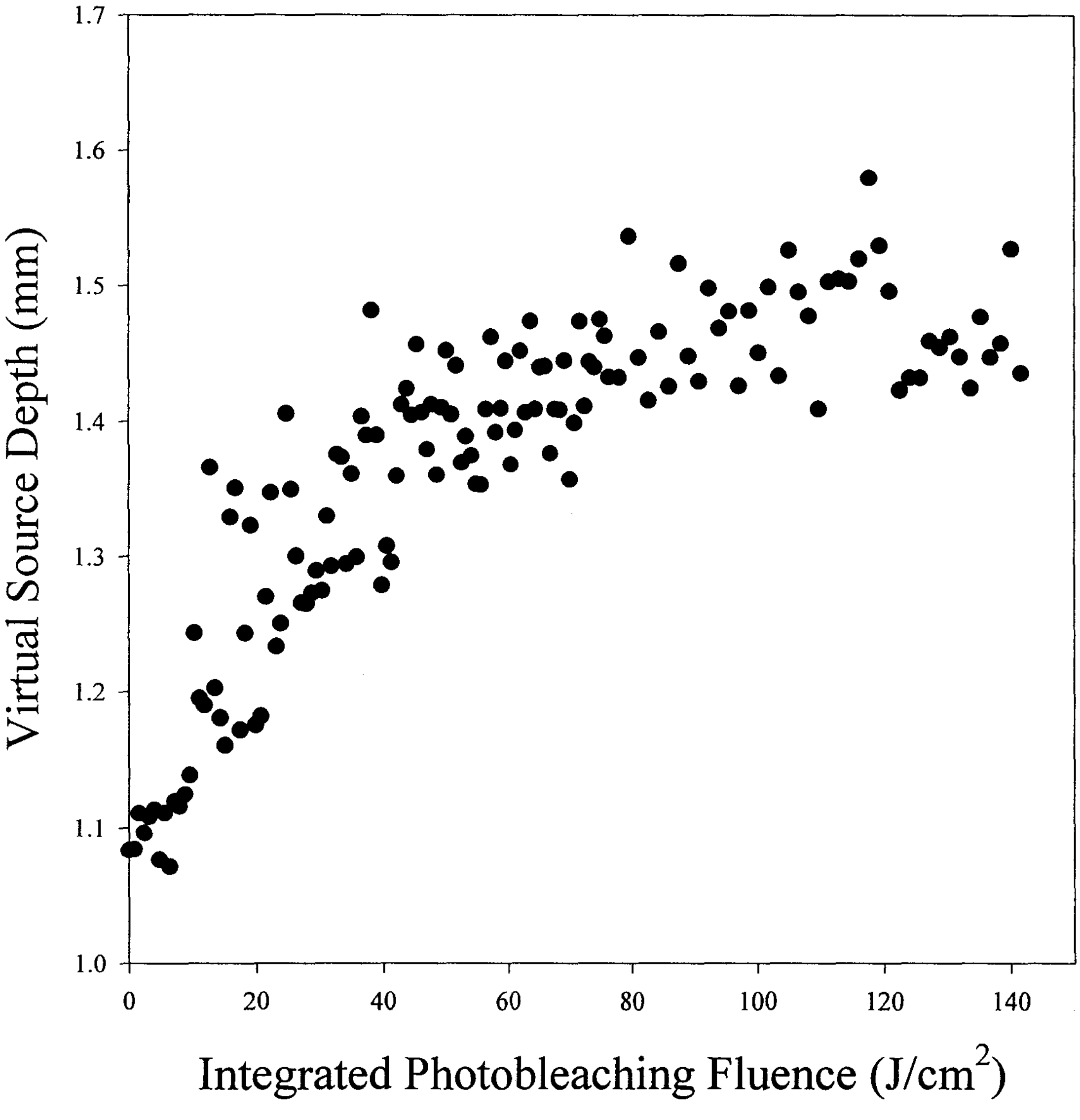

Figure 4.4.8 Virtual source depth as a function of integrated photobleaching fluence for Purple phantom.

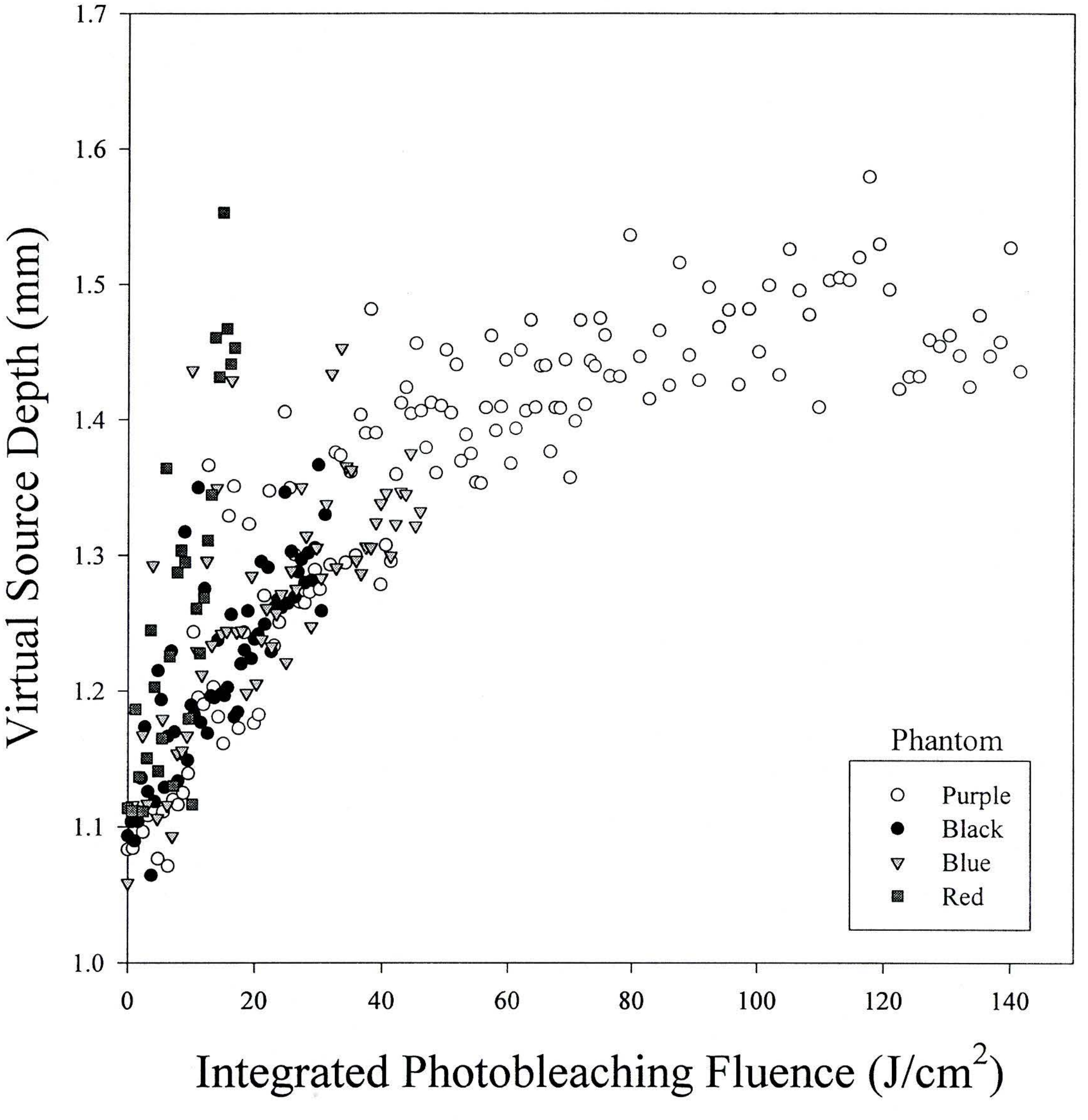

Figure 4.4.9 Virtual source depth as a function of integrated photobleaching fluence for all four standard phantoms.

The effects of changing the initial drug absorption coefficient are shown in figure 4.4.10. While the phantoms having standard and high concentrations of photosensitizer seem to behave as predicted by the modelling, druglo does not. Since this model necessitates a high total absorption to minimize the effects of scattering, a low drug concentration is far from ideal, explaining the poor result.

Figure 4.4.11a follows from the variation of phantom background absorption by 100 percent in either direction from the standard. Three distinct curves are fairly evident, all following the expected trends shown in figure 4.4.11b. Considering the small effect on the mean free path that occurs for these changes in absorption coefficient, the close grouping of the initial virtual source depths is favourable, although once again they are slightly higher than expected.

The last set of curves (figure 4.4.12) demonstrates the effect of altering the scattering coefficient, and provides the most perplexing results. Although this model is based on a highly absorbing medium, it is the phantom with the higher scattering that behaves as it should, having an initial virtual source depth close to its mean free path (0.7 mm compared with 0.6 m) and tracking below the standard phantom. At the same time, the phantom having a low scattering coefficient is much more shallow than the modelling predicts, actually falling below the standard phantom curve.

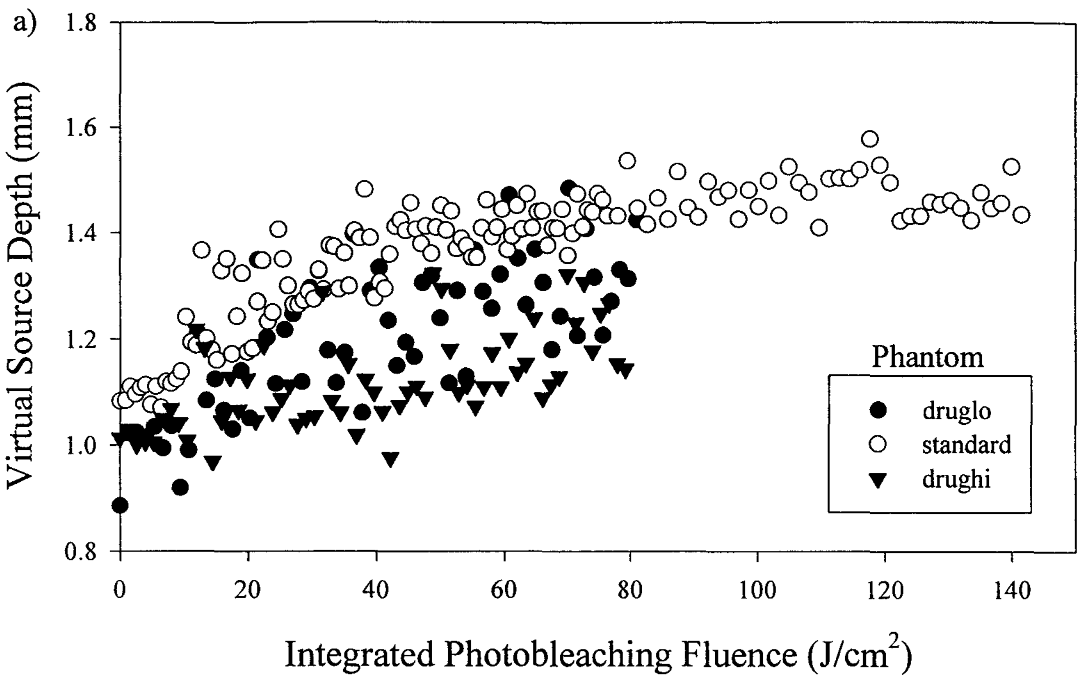

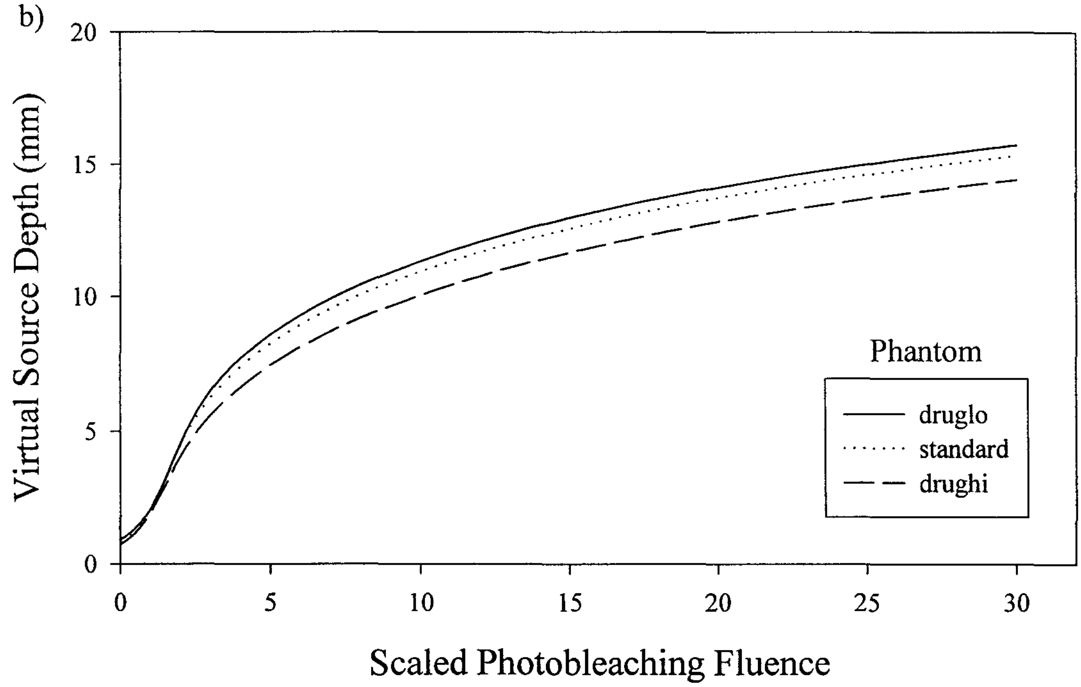

Figure 4.4.10 **a)** Experimentally determined virtual source depth as a function of integrated bleaching fluence for varied drug absorption coefficient.
b) Predicted virtual source depth versus scaled photobleaching fluence using the highly absorbing model with measured phantom optical properties.

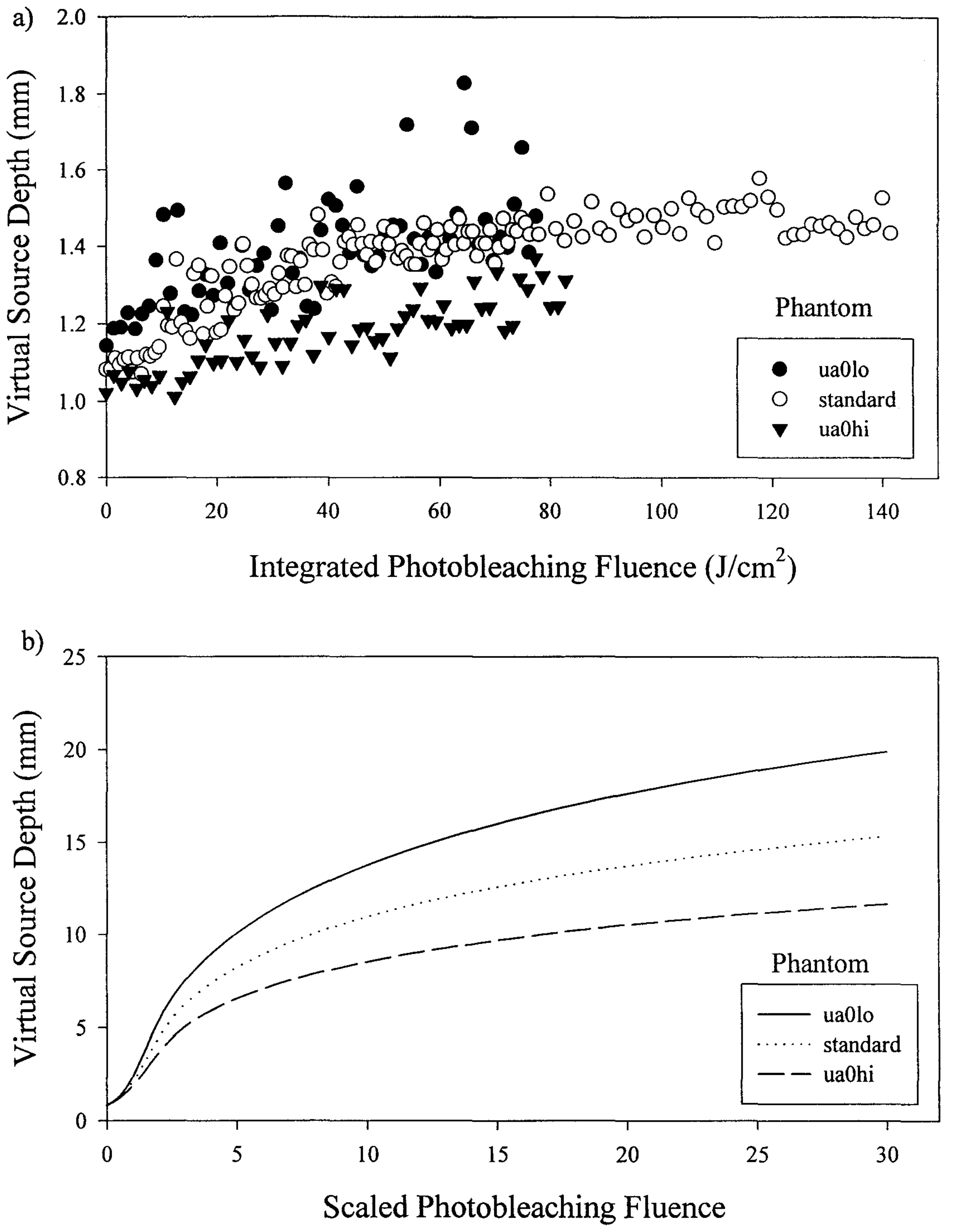

Figure 4.4.11 **a)** Experimentally determined virtual source depth as a function of integrated bleaching fluence for varied endogenous tissue absorption.
b) Predicted virtual source depth versus scaled photobleaching fluence using the highly absorbing model with measured phantom optical properties.

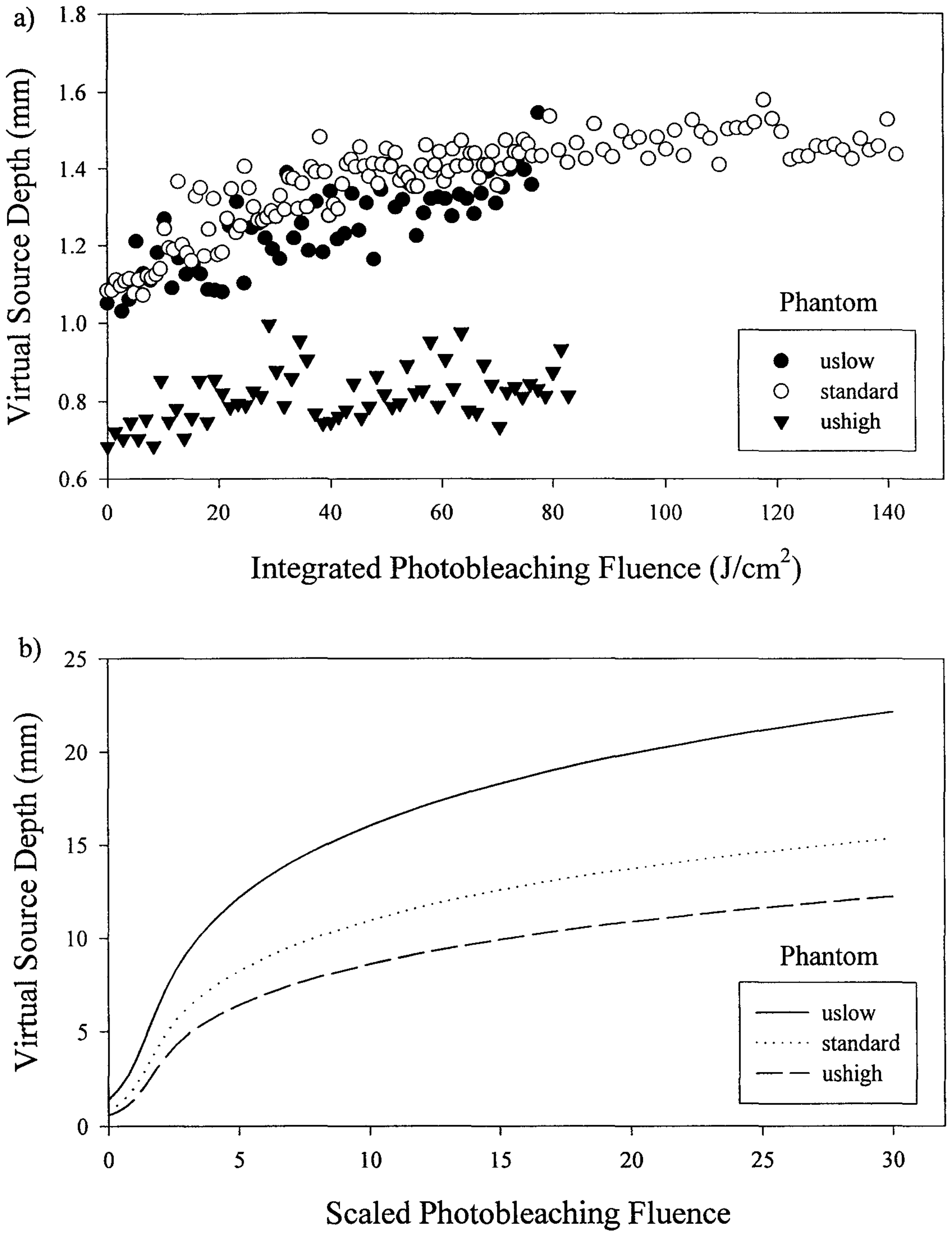

Figure 4.4.12 **a)** Experimentally determined virtual source depth as a function of integrated bleaching fluence for varied tissue scattering coefficient.

b) Predicted virtual source depth versus scaled photobleaching fluence using the highly absorbing model with measured phantom optical properties.

5 DISCUSSION

5.1 Predictive Value of Theoretical Models

It is important to discuss the applicability of the mathematical modelling to actual PDT treatments. Each model has been designed to simulate a realistic treatment method so that experimental verification may be performed on phantoms, and eventually in a clinical setting.

The broad-beam photobleaching model is appropriate for describing the irradiation of a tumour near the surface of the skin. Diffusion theory performs well for the tissue optical properties normally encountered in human tissue, and treatment is often performed using laser sources with lenses to spread the beam, or slide projectors at 630 nm (McCaughan 1992).

As long as the instrumentation remains stable, it is convenient to place a single fibre on the surface while irradiating with the broad-beam treatment source. Only a single light source is required, and the measurement process could be automated. As seen in section 3.1, the relationship between observed fluorescence and necrosis depth is very sensitive to changes in optical properties and drug concentration. However, if accurate measurements of the initial treatment parameters could be made, it would be possible to obtain information about the photosensitizer distribution and photodynamic dose from the decreasing fluorescence signal.

Using a pencil beam source for fluorescence excitation allows for spatially resolved fluorescence measurements to be made. Although the probe would have to be manually placed on the surface at fixed time intervals (the treatment light would be turned off), normalization to one of the detection fibres removes the variation introduced by making random measurements in different locations.

For the scatter dominated model, the 630 nm treatment laser could be coupled into the probe for fluorescence excitation, requiring only one laser source. If the optical properties could be determined at the fluorescence wavelength, escape probabilities could be calculated through the modelling and the virtual plane depth could be tracked while the treatment progressed. Since the virtual plane depth calculations are based on fluorescence escape probabilities, they do not depend heavily on photosensitizer concentration. Since the relationship between virtual plane depth and necrosis depth is fairly insensitive to changes in optical properties at treatment wavelengths (section 3.2), the progression of tumour damage could be followed during treatment based on the penetration of the virtual plane.

Excitation with a pencil beam of light in a highly absorbing medium is most plausible at lower excitation wavelengths. Thus, a second light source other than the treatment light is necessary. The combination of an argon ion laser and pumped dye laser is ideal. In this case, the spatially resolved fluorescence measurements arising from the optical fibre based probe allow for the calculation of a virtual source depth without any *a priori* knowledge of tissue optical properties or photosensitizer concentration. If the relationship between the virtual source depth and necrosis depth could be determined experimentally, its robust nature would allow accurate determination of tumour damage as treatment progresses using only the changes in radial fluorescence.

Although bleaching was minimal for the phantoms studied, both pencil beam excitation models were shown to track the progress of the respective virtual fluorescence depth indicators, illustrating the sensitivity of the technique. It seems reasonable that if the idea of determining a virtual source could be applied to a model that works for more realistic optical properties, accurate PDT dosimetry will be possible based on emitted fluorescence only.

5.2 Phantom Measurements

In general, the phantoms used for the photobleaching experiments gave favourable results. The uniform, flat surface allowed for simple, consistent measurements of optical properties and emitted fluorescence. Photobleaching was evident by the decrease in observed fluorescence, and radially resolved measurements allowed the increase in average photosensitizer depth to be monitored. Although the bleaching was much less than desired, the fact that the virtual plane and source depths could be tracked over very small distances illustrates the high sensitivity of the technique.

As mentioned, the most glaring problem with the phantom results is the very shallow penetration of the virtual plane and source depths achieved compared with the mathematical predictions. The phantom optical properties were fairly well characterized, so the problem was thought to originate with the bleaching of the drug. Visually detectable changes in colour were noticeable in bleached areas of cuvettes containing just

Photofrin and resin, however no such difference was apparent with the phantoms, even after 15 hours of bleaching. In addition, total absorption coefficient measurements on the surface of the phantoms at 630 nm after the bleaching experiments gave minimal decrease in absorption coefficient. Bleach rate experiments on cuvettes containing only resin and Photofrin demonstrated much more rapid photobleaching, giving bleach rates much higher than observed in the phantoms (figure 4.2.1). A reaction may be taking place between either the TiO_2 or the background dye and the Photofrin to somehow alter the photochemistry in the phantom such that the drug did not bleach to the same extent as previously. Alteration of the photosensitizer molecules could also result from the heating that occurs with the exothermic resin curing reaction. This would have less effect on the small volume of the cuvette due to the increased relative surface area allowing for better heat dispersion.

In an attempt to obtain a better understanding of what is occurring, a cuvette sized piece of phantom material was cut from the centre of phantom druglo and the bleach rate was measured as previously described. Although the scatterer present will increase the fluence rate in the sample by an appreciable factor (figure 2.1.1a), the effect will be small when compared with observed changes to the bleach rate. Figure 5.2.1 shows the resultant fluorescence decrease over the course of treatment. Using equation 59, and assuming a modest increase in the incident fluence by a factor of three due to scattering, the bleach rate was determined to be 1.5E-4 cm^2/J. Comparison with the previous bleach rate indicates a large discrepancy between this result and that for the cuvette containing only resin and Photofrin (1.5E-2 cm^2/J). Further investigation of this effect is required.

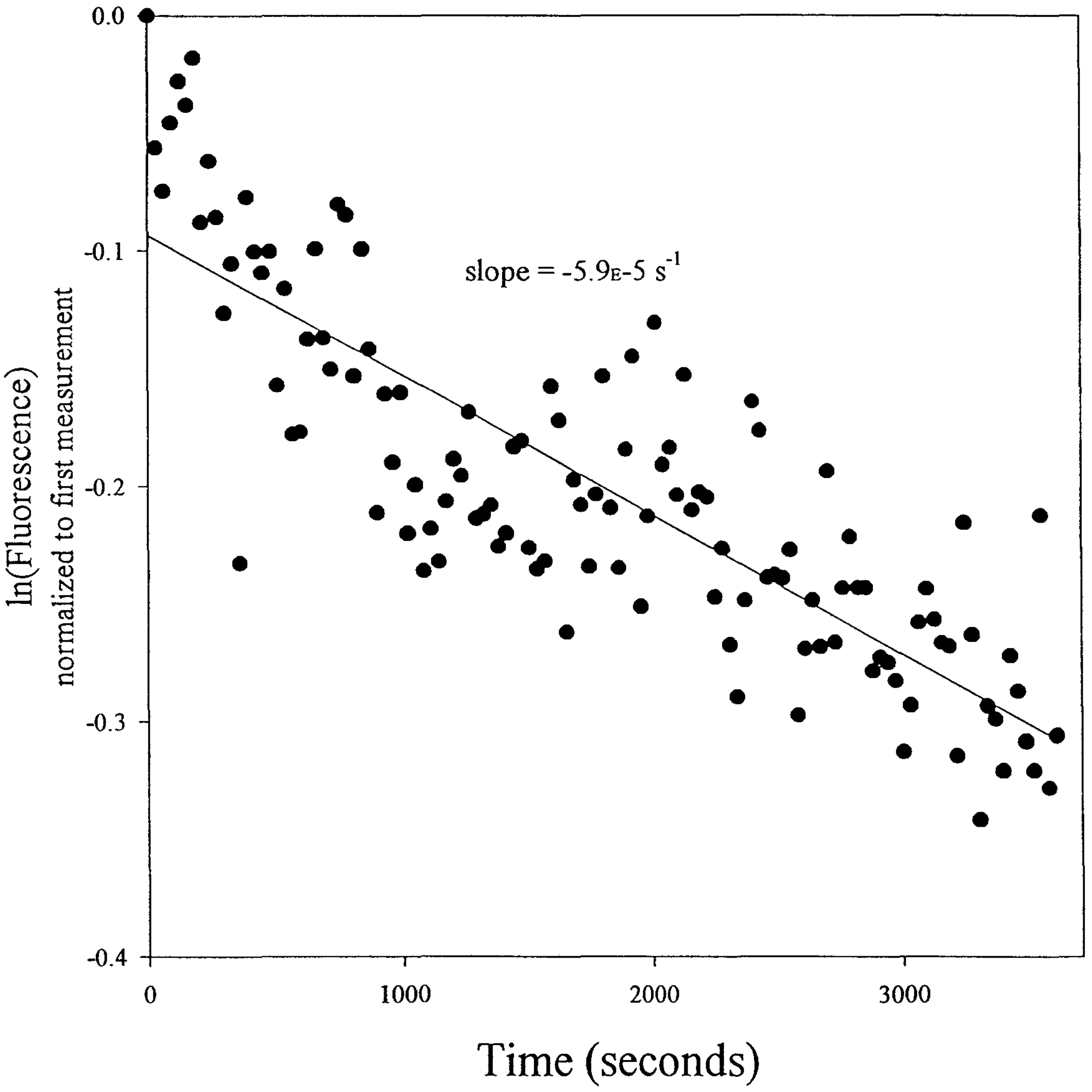

Figure 5.2.1 Fluorescence decrease as a function of time for a cuvette sized phantom piece (druglo). The fitted line shown has a slope of -5.9E-5 s^{-1} giving a bleach rate of 1.5E-4 cm^2/J.

5.2.1 Virtual Plane Depth

The fundamental requirement in order to implement a virtual plane depth is a scatter dominated medium. Since absorption by the phantoms is lower at higher wavelengths, ideally 630 nm light would be used in fluorescence excitation. This would also eliminate any photobleaching resulting from measurements performed at lower wavelengths. Unfortunately, although attempts were made to take advantage of this fact, very little fluorescence was observed using 630 nm excitation leading to the use of 515 nm light to acquire an adequate number of fluorescence counts. Scattering should still be sufficiently high at this wavelength to allow for comparison with the scatter dominated model. The added benefit of this lower excitation wavelength is that a greater range of the fluorescence spectrum is observable, allowing for characterization of the 630 and 690 nm Photofrin peaks.

In order to better understand the deviations from the expected results, it is useful to consider what occurs when drug absorption is not negligible. If the ratio of scatter to absorption is varied without changing the total interaction coefficient, increasing the absorption will result in fewer scattering events at all depths. There will be a corresponding decrease in the fluorescence initiated away from the excitation beam axis arising from the diffusely scattered light, and an increase in the fluorescence near the axis resulting from the absorbed photons. Since the fluorescence observed at the further radii primarily arises from the deeper fluorescence sources, and sources closer to the detection fibres, there will be less fluorescence detected in the furthest fibres from the source. This will cause the fluorescence as a function of radius to shift slightly, resulting in a virtual plane depth that is not as deep as predicted. This may help to explain why the phantoms having the highest scatter to absorption ratio have initial virtual plane depths closest to one mean free path, whereas the lower this ratio becomes, the more shallow the initial plane depth.

Another problem is the assumption that the drug concentration does not affect the distribution of diffuse excitation fluence. In the model, the single scatter source at a depth of one mean free path gives rise to a spherically symmetric excitation fluence that does not change with time. However, as the photosensitizer bleaches near the surface, this distribution will become skewed as excitation light fluence becomes higher towards the surface of the medium. The effects of this are difficult to predict and warrant modelling using Monte Carlo simulations.

5.2.2 Virtual Source Depth

In all cases, the virtual source depth originates slightly deeper than predicted, with the exception of the low scattering phantom. This may be due to the much higher scattering levels than would normally be expected with this model. If the total attenuation coefficient remains constant but the ratio of scatter to absorption is increased slightly, the average interaction depth will remain constant $(\frac{1}{\mu_t'})$ while the percentage of absorption events will decrease as scatter becomes more of a factor. Fluorescence events originating on the excitation beam axis will decrease, whereas fluorescence created away from this axis and deeper within the medium will increase. Fluorescence photons that come from deeper within the medium or further from the excitation axis have a better probability of reaching the more distant radii at the surface. There will be a relative increase in the fluorescence reaching the distant detectors, resulting in a downward shift of the virtual source depth. This effect should be magnified as the ratio of absorption to scattering decreases, and this may help to explain the unexpected data in figure 4.4.12a. The calculated virtual source depth will be closer to its predicted value (1.2 mm) for the low scattering phantom while it is greater than expected for the standard phantom bringing the two curves together in figure 4.4.12a. Also a consideration is the variation in total interaction coefficient between phantoms which will affect the initial depth of the virtual source (initial virtual source depth $\approx \frac{1}{\mu_t'}$).

5.2.3 Further Discussion

The assumption that light incident on the surface of the medium does not deviate from its well-collimated, pencil beam geometry should be discussed. Realistically, the beam will spread out in the radial direction, highly dependant on tissue optics. This divergence will increase the average path length that the photons must follow in order to penetrate into the medium, thereby decreasing the fluence rate. Less fluorescence will originate from deep in the medium, and since this accounts for the majority of the fluorescence reaching the most distant detectors on the surface, there will be a slight shift in the radial distribution towards the near fibres. As a result, both the experimentally determined virtual plane and source depths may be shifted closer to the surface than the modelling predicts.

In all cases, the virtual source depth was larger than the virtual plane depth. This may be due to the assumption discussed previously that photobleaching of the photosensitizer does not affect the excitation fluence distribution in the scatter dominated model. As bleaching occurs, there will be an increase in excitation fluence closer to the surface from the single scatter source at depth $\frac{1}{\mu_t'}$. Although prediction about the effects are difficult to make and require further study, it seems logical that this increased excitation could increase the fluorescence at the inner fibres thereby making the virtual plane depth appear more shallow. This would work to slow the regular progression of the plane depth as treatment progresses.

In general, the trends observed in the virtual plane and source depth curves were in agreement with the mathematical models. In the instances where the modelling was expected to perform poorly, such as the highly absorbing phantom in the scatter dominated model, and the phantom with low drug concentration in the absorption dominated model, it failed. The phantoms were designed to have optical properties comparable to those of tissue, and as a result were not particularly suited to either model. Although the absorption coefficient of the photosensitizer could be increased by exciting with a lower wavelength, there were no phantoms in which absorption dominated scatter. At the same time, scattering was generally much higher than absorption in the phantoms, but the requirement of 515 nm excitation light in order to see appreciable fluorescence made circumstances less than ideal for the scatter dominated model. It should be remembered, however, that the modelling is attempting to describe the photodynamic process in tissue, and that alterations must be made to the models, not the reverse.

5.3 Future Directions

The most obvious continuation of this work involves the development of mathematical models that are more useful in the region where scatter and absorption are comparable or in which scatter dominates, but bleaching does affect the excitation fluence. Work has been initiated involving Fermi-Eyges theory for the former, and Monte Carlo for the latter to more accurately model the penetration of a pencil beam into a medium. The spherical model also requires further consideration, possibly incorporating several radially resolved fluorescence measurements and the calculation of a virtual shell depth similar to the semi-infinite medium.

In order to test the improved models, optical phantoms should be improved. To obtain a better understanding of the Photofrin reactions that occurred, the phantoms will require dissection and analysis by fluorescence microscopy or chemical techniques. Different dyes should be tested in the phantoms to determine if the effect on bleach rate is limited to Photofrin. If the problem persists, the time consuming task of developing a new phantom, with the same characteristics but composed of different materials, will have to be undertaken. Also a consideration would be the addition of a dye with an absorption spectrum similar to the endogenous chromophores in human tissue to improve realism.

In order to perform rigorous testing of the models in a biological system, *in vivo* studies will be required. Treatment analogous to that performed on the phantoms will be done on animal models after injection with photosensitizing drugs. The decreasing fluorescence will give similar information about the photosensitizer distribution which can be compared with the actual distribution found by chemical extraction of biopsied tissue, or fluorescence microscopy. Unlike the phantom resin, necrosis will occur in the tissue and the depth may be determined. This will allow for the establishment of a relationship between the predicted progression of photosensitizer bleaching (for example using virtual source depth) and necrosis depth.

5.4 Conclusions

Light propagation through tissue is known to be accurately predicted by diffusion theory, and the phenomenon of photosensitizer photobleaching is also well established. The mathematical models presented combine these ideas and calculate the resulting fluorescence observed at the surface based on the changing distribution of photosensitizer for varying initial optical properties. Models where scatter dominates absorption and vice-versa have been addressed and were shown to agree qualitatively with experimental findings, even though the phantoms used were ideal for neither model. Spatially resolved fluorescence emission was experimentally measured and the process of photobleaching observed. The relative decrease in fluorescence in spatially resolved measurements occurred as predicted, allowing for the determination of virtual plane and source depths that can localize the bleached/non-bleached photosensitizer interface. If the destruction of the drug and tissue are mediated by the same photoproduct in tissue, it may be expected that this bleached drug interface will be related to the depth of necrosis. If this relationship could be determined, the modelling could make predictions about necrosis depth from measurements of the changing fluorescence signal. Calculation of the virtual fluorescence source depth can be performed without accurate knowledge of tissue optics, initial concentration of photosensitizer, and bleach rate which could lead to much more efficient, effective treatment in a clinical environment. These results indicate that, with improvement of the current modelling to better handle realistic optical properties, potential exists for the development of an accurate dosimetry technique in photodynamic therapy.

REFERENCES

Brown, S.G., Tralau, C.J., Coleridge-Smith, P.D., Akdemir D. and Wieman, T.J., 1986, "Photodynamic therapy with porphyrin and phthalocyanine sensitizer: quantitative studies in normal rat liver," *Br. J. Cancer* **54**, 43-52.

Boyle, D.G. and Potter, W.R., 1987, "Photobleaching of Photofrin II as a means of eliminating skin photosensitivity," *Photochem. Photobiol.* **46**, 997-1001.

Dougherty, T.J., Kaufman, J.E., Goldfarb, A. *et al*, 1978, "Photoradiation therapy for the treatment of malignant tumours," *Cancer Res.* **38**, 2628-2635.

Dougherty, T.J., 1987, "Photosensitizers: Therapy and detection of malignant tumours," *Photochem. Photobiol.* **45**, 874-889.

Eason, G., Veitch, R., Nisbet, R. and Turnbull, F., 1978, "The theory of backscattering of light by blood," *J. Phys. D* **11**, 1463-1479.

Farrell, T.J., Patterson, M.S., Hayward, J.E., Wilson, B.C., and Beck, E.R., 1994, "A CCD and neural network based instrument for the non-invasive determination of tissue optical properties *in vivo*," *SPIE Proceedings, Vol 2135*, 117-128.

Farrell, T.J., Patterson, M.S. and Wilson, B.C., 1992, "A diffusion theory model of spatially resolved, steady-state diffuse reflectance for the non-invasive determination of tissue optical properties *in vivo*," *Medical Physics* **19**, 879-888.

Farrell, T.J., Wilson B.C., Patterson, M.S. and Chow, R., 1991, "The dependence of photodynamic threshold dose on treatment parameters in normal rat liver *in vivo,*" *SPIE Proceedings, Vol. 1426,* 146-155.

Figge, F.H.J., Weiland, G.S. and Manganiello, L.O.J., 1948, "Cancer detection and therapy. Affinity of neoplastic, embryonic, and traumatized tissues for porphyrins and metalloporphyrins," *Proc. Soc. Exper. Biol. and Med.*, **68**, 181-188.

Gerald, C.F. and Wheatley, P.O., 1970, *Applied Numerical Analysis*, Addison-Wesley Publishing, Don Mills, ON.

Gregorie, H.G., Horger, E.O., Ward, J.L. *et al*, 1968, "Hematoporphyrin derivative fluorescence in malignant neoplasms," *Ann. Surg.* **167**, 820-828.

Groenhuis, R.A, Ferwerda, H.A. and.Bosch, J.J.T, 1983, "Scattering and absorption of turbid materials determined from reflection measurements. 1: Theory," *Applied Optics* **22**, 2456-2462.

Hale, G.M. and Querry, M.R., 1973, "Optical constants of water in the 200 nm to 200 μm wavelength region," *Applied Optics* **12**, 555-563.

Hamblin M.R. and Hasan, T., 1996, Photodynamic Therapy Review, *Optics and Photonics News*, 17-21.

Keijzer, M., Star W.M. and Storchi, P.R.M., 1988, "Optical Diffusion in Layered Media," *Applied Optics* **27**, 1820-1824.

Li, H. and Xie, S., 1996, "Measurement method of the refractive index of biotissue by total internal reflection," *Applied Optics* **35**, 1793-1795.

Lipson, R.L., Gray, M.J. and Baldes, E.J., 1966, "Hematoporphyrin derivative for detection and management of cancer," *Proc. 9th International Cancer Congress*, Tokyo.

Mang, T.S., Dougherty, T.J., Potter, W.R., Boyle, D.G., Somer, S. and Moan, J., 1987, "Photobleaching of porphyrins used in photodynamic therapy and implications for therapy," *Photochem. Photobiol.* **45**, 501-506.

Mathews, J. and Walker, R.L., 1970, *Mathematical Methods of Physics*, Benjamin/Cummings, Menlo Park, CA.

McCaughan, J.S., 1992, *A Clinical Manual: Photodynamic Therapy of Malignancies*, R.G. Landes Company, Austin.

Moan, J., 1986, "Effect of bleaching on porphyrin sensitizers during photodynamic therapy," *Cancer Letters* 33, 45-53.

Pass, H.I., 1993, "Photodynamic Therapy in Oncology: Mechanisms and Clinical Use," *J. Natl. Cancer Inst.* **85,** 443-456.

Patterson, M.S., Chance, B. and Wilson, B.C., 1989, "Time resolved reflectance and transmittance for the non-invasive measurement of tissue optical properties," *Applied Optics* **28**, 2331-2336

Patterson, M.S., Wilson, B.C. and Graff, R., 1990, "*In vivo* tests of the concept of photodynamic threshold dose in normal rat liver photosensitized by aluminum chlorosulphonated phthalocyanine," *Photochem. Photobiol.* **51**, 343-349.

Patterson, M.S. and Wilson, B.C., 1994, "A theoretical study of the influence of sensitizer photobleaching on depth of necrosis in photodynamic therapy," *SPIE Proceedings, Vol. 2133*, 208-219.

Potter, W.R., 1986, "The theory of photodynamic therapy dosimetry: consequences of photodestruction of sensitizer," *SPIE Proceedings Vol. 712,* 124-129.

Svaasand, L.O. and Gomer, C.J., 1989, "Optics of Tissue," *Dosimetry of Laser Radiation in Medicine and Biology, Vol. IS5*, 114-132.

Thorpe, W.P., Toner, M., Ezzell, R.M., Tompkins, R.G. and Yarmush, M.L., 1995, "Dynamics of photoinduced cell plasma membrane injury," *Biophysical Journal* **68**, 2198-2206.

Wilson, B.C., 1989, "Photodynamic therapy: light delivery and dosage for second-generation photosensitizers," in *Photosensitizing Compounds: their Chemistry, Biology and Clinical Use*, 60-77, Wiley, Chichester.

Wilson, B.C., Park, Y., Hefetz, Y., Patterson, M.S., Masden S. and Jacques, S., 1989, "The potential of time-resolved reflectance measurements for the non-invasive determination of tissue optical properties," *SPIE Proceedings, Vol 1064*, 97-106.

Wilson, B.C., Patterson, M.S. and Lilge, L., in press, "Implicit and explicit dosimetry in photodynamic therapy: a new paradigm," *Lasers in Medical Science*.